# TUM

## Technische Universität München

# Dark Matter Phenomenology in Scalar Extensions of the Standard Model

Dissertation

by

Camilo A. Garcia Cely
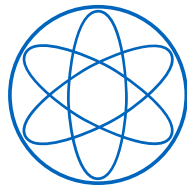
Physik Department T30d

# Technische Universität München

## Physik Department T30d

# Dark Matter Phenomenology in Scalar Extensions of the Standard Model

## Camilo A. Garcia Cely

Vollständiger Abdruck der von der Fakultät für Physik der Technischen Universität München zur Erlangung des akademischen Grades eines

**Doktors der Naturwissenschaften**

genehmigten Dissertation.

| | | |
|---|---|---|
| Vorsitzender: | | Univ.–Prof. Dr. Lothar Oberauer |
| Prüfer der Dissertation: | 1. | Univ.–Prof. Dr. Alejandro Ibarra |
| | 2. | Univ.–Prof. Dr. Nora Brambilla |

Die Dissertation wurde am 06.08.2014 bei der Technischen Universität München eingereicht und durch die Fakultät für Physik am 01.09.2014 angenommen.

*A mis padres*
*Alfredo y Rosa*

# ABSTRACT

We consider three models that address the nature of dark matter and that are characterized by the presence of new scalar fields. In one of them, dark matter is constituted by a particle with identical quantum numbers as the Higgs boson. In the other two, the stability of dark matter is due to a discrete symmetry that arises from the spontaneous breaking of a global symmetry. Consequently, both scenarios contain a Goldstone boson and another particle that mixes with the Higgs boson. We investigate the phenomenological consequences in cosmology as well as in direct and indirect dark matter experiments. In particular, we analyze the gamma-ray spectral features that arise in dark matter annihilations from every scenario, concretely monochromatic lines, virtual internal bremsstrahlung and gamma-ray boxes. For the first model, we show that the one-loop annihilation into gamma-rays violates unitarity and argue that including the so-called Sommerfeld effect solves this problem. In addition, for the second and third models, we study the contribution of their Goldstone boson to the radiation density of the Universe as well as its role in dark matter production during the Early Universe.

# ZUSAMMENFASSUNG

Wir untersuchen drei Modelle, die die Beschaffenheit der Dunklen Materie beschreiben und sich durch die Existenz von neuartigen Skalarfeldern auszeichnen. In einer dieser Szenarien ist die Dunkle Materie ein Teilchen mit identischen Quantenzahlen wie das Higgs-Boson, während in den anderen beiden Modellen die Stabilität des Dunkle-Materie Teilchens durch eine diskrete Symmetrie garantiert wird, welche ihren Ursprung in der spontanen Brechung einer globalen Symmetrie hat. Folglich beinhalten beide Modelle ein Goldstone-Boson und ein weiteres Teilchen welches sich mit dem Higgs-Boson mischt. Wir untersuchen die phänomenologischen Konsequenzen im Gebiet der Kosmologie sowie für Experimente zur indirekten und direkten Suche nach Dunkler Materie. Insbesondere untersuchen wir für jedes der Szenarien spektrale Merkmale der Gammastrahlung, welche in der Annihilation der Dunklen Materie entsteht; im speziellen betrachten wir monochromatische Linien, Virtuelle Interne Bremsstrahlung und boxförmige Spektren. Im Falle des ersten Modells zeigen wir dass die one-loop Annihilation in Gammastrahlung die Unitarität der Theorie verletzt, und wir argumentieren, dass die Berücksichtigung des sogenannten Sommerfeld-Effekts dieses Problem löst. Für das zweite und dritte Modell untersuchen wir den Beitrag des Goldstone-Bosons zur Strahlungsdichte im Universum sowie seine Rolle in der Produktion der Dunklen Materie in der Anfangsphase des Universums.

# Contents

# Introduction

The Standard Model (SM) has been spectacularly confirmed at the Large Hadron Collider (LHC). In particular, we are sure about the existence of the Higgs boson [1,2], which is -to the best of our knowledge- the first elementary scalar that has been observed. Nevertheless, only a small part of the Universe is described by the SM. In fact, the nature of so-called dark matter is unknown in spite of its gravitational effects in the dynamics of galaxies, clusters of galaxies or in the Universe at large scale (for a review see [3–5]). Because of this, it is reasonable that other scalar particles exist and that they are closely related to the properties of dark matter. Consequently, in this thesis we consider some extensions of the Standard Model that address the nature of dark matter and that are characterized by the presence of new scalar particles.

In analogy to the Higgs boson, it is conceivable that some of these scalar particles belong to another scalar doublet. In fact, this is not counter-intuitive as each fermionic representation in the SM is repeated three times. In this work we address this possibility, specifically we study the Inert Doublet Model (IDM) [6–18], a minimal extension of the SM which consists in introducing one extra scalar doublet, odd under an unbroken $Z_2$ symmetry, with identical gauge quantum numbers as the SM Higgs. The discrete symmetry ensures the stability of the lightest extra particle, which could therefore be a candidate for dark matter. In spite of the minimality of the IDM, its phenomenology is very rich. In this work we particularly focus in the possibility of detecting signatures of the IDM through the observation of the gamma-rays that are produced in dark matter annihilations. We will see that -in order to do that properly- we must consider a non-perturbative effect usually called Sommerfeld enhancement [19–28].

Even if dark matter is not made of scalar particles, these can still play an important role in its phenomenology. In this thesis we investigate two models in which scalar particles are closely related to the stability of dark matter. In general, the latter is likely due to the existence of a preserved, or very mildly broken, symmetry in the Lagrangian (see [29] for a review of possible explanations to the dark matter stability). The simplest symmetry that ensures the absolute stability of the dark matter particle is a discrete $Z_2$ symmetry, as in the IDM case. The discrete symmetry in the Lagrangian could be imposed by hand or could, perhaps more plausibly, arise as a remnant of the breaking of a global continuous symmetry. Indeed, if a global $U(1)$ symmetry is spontaneously broken by a scalar field with charge 2 under that symmetry, a discrete $Z_2$ symmetry automatically arises in the Lagrangian [30].

As in the case of the IDM, the phenomenology of these models is very rich. In fact, the spontaneous breaking of a global continuous symmetry, as is well known, gives rise to massless Goldstone bosons in the spectrum [31–33]. In this work we show that the Goldstone boson that

arises in this framework could contribute to the radiation density of the Universe and can mimic neutrinos in the Cosmic Microwave Background [34,35]. In addition, we argue that the Goldstone bosons associated to the stability of the dark matter also play a crucial role in the dark matter production. Moreover, we show that these models predict the existence of a $CP$-even scalar with similar properties to the SM Higgs. In fact, this leads to the interaction of the dark matter particle with nucleons, thus opening the possibility of detecting signatures of these models in direct dark matter search experiments. We also discuss the phenomenological implications of these models in indirect detection experiments.

This thesis consists of four parts. Part I, which includes chapters 1 and 2, introduces the basics of dark matter phenomenology. Part II, which consists of chapters 3, 4, 5 and 6, discusses the IDM. Concretly, in chapter 3, we introduce the model. In chapter 4, we discuss the annihilation of dark matter into photons and show that we must include a non-perturbative effect, which we address in chapter 5. In chapter 6, we discuss the limits on the IDM coming from dark matter indirect detection experiments with gamma-rays. Subsequently, in part III, consisting on chapters 7,8, 9 and 10, we introduce two models in which the stability of dark matter is due to the spontaneous breaking of a global symmetry. Chapter 9 discusses the conditions under which the corresponding Goldstone-boson contributes to the radiation density of Universe, and in chapter 10, using dark matter indirect detection experiments with gamma-rays, limits on these models are derived. Finally, we conclude this thesis in part IV.

Some parts of this work have been also discussed in separate articles:

[36] **Novel Gamma-ray Spectral Features in the Inert doublet Model**,
C. Garcia-Cely and A. Ibarra,
JCAP **1309**, 025 (2013)

[37] **Dark matter production from Goldstone boson interactions and implications for direct searches and dark radiation**,
C. Garcia-Cely, A. Ibarra and E. Molinaro,
JCAP **1311**, 061 (2013)

[38] **Cosmological and astrophysical signatures of dark matter annihilations into pseudo-Goldstone bosons**,
C. Garcia-Cely, A. Ibarra and E. Molinaro,
JCAP **1402**, 032 (2014)

[39] **Sommerfeld Enhanced Gamma-Ray Spectral Features from the Inert doublet Model**,
C. Garcia-Cely, M. Gustafsson and A. Ibarra,
To be submitted

# Part I

# Basics of Dark Matter Phenomenology

# Chapter 1

# Introduction to Dark Matter

Before describing the models under consideration in this thesis, we first introduce the basic concepts of dark matter phenomenology. In particular, in this chapter we discuss the evidence that supports the existence of dark matter and describe the properties that this must have.

## 1.1 Elements of Standard Cosmology

Standard Cosmology is built upon the Cosmological Principle, which states that the Universe at sufficiently large scales is isotropic and homogeneous. By demanding a solution of the Einstein's General Relativity Equations in agreement with this principle, one arrives at the conclusion that there is a reference frame where the space-time metric takes the so-called Friedmann-Lemaître-Robertson-Walker (FLRW) form [1]. In spherical coordinates $t, r, \theta, \phi$ this metric is

$$ds^2 = dt^2 - a(t)^2 \left( \frac{dr^2}{1 - kr^2} + r^2(\sin^2\theta + \phi^2) \right), \tag{1.1}$$

where $k = 0, 1$ or $-1$ for a flat, positively curved or negatively curved Universe respectively. The reference frame where the metric takes this particular form is called the comoving frame.

The function $a(t)$ in Eq. (1.1) is usually called the scale factor and it accounts for the expansion of the Universe, whose rate is given by the Hubble parameter $H \equiv \dot{a}/a$ [41].

In order to study the expansion of the Universe it is necessary to consider its energy content, which -for an isotropic and homogeneous metric- is described by a perfect fluid with energy density $\rho$ and pressure $p$. In general, these quantities receive contributions from different types of fluids: matter, radiation and dark energy. Matter is constituted by non-relativistic particles - for instance, baryons or dark matter today- and it is therefore pressureless, that is $p_M = 0$. In contrast, radiation is made of relativistic particles like photons or neutrinos and follows the equation of state $p_R = \frac{1}{3}\rho_R$. Finally, the nature of dark energy is currently unknown, however for the sake of simplicity I assume here that this component of the Universe is described by a cosmological constant $\Lambda$ such that $\rho_\Lambda = -p_\Lambda = \Lambda$.

---

[1]For a comprehensive review see, *e.g.*, [40].

With this, the Einstein's equations for the FLRW Universe are

$$\sum_i \left( \dot{\rho}_i + 3H(\rho_i + p_i) \right) = 0, \tag{1.2}$$

$$H^2 + \frac{k}{a^2} = \frac{8\pi G}{3} \sum_i \rho_i. \tag{1.3}$$

These expressions are called the Friedmann equations. Here $i$ stands for $M, R$ or $\Lambda$. On the one hand, Eq. (1.2) is the energy conservation law for a fluid in a FLRW Universe. In fact, one can assume that this equation holds individually for the matter, the radiation and the dark energy fluids. If that is the case, one finds that, as the Universe expands, the different densities scale as $\rho_M \propto a(t)^{-3}$, $\rho_R \propto a(t)^{-4}$ and $\rho_\Lambda \propto a(t)^0$. On the other hand, Eq. (1.3) describes the evolution of the scale factor $a(t)$. By writing the energy densities in terms of the critical density $\rho_c$

$$\rho_c \equiv \frac{3H^2}{8\pi G}, \tag{1.4}$$

one can write Eq. (1.3) as

$$1 - \Omega_k = \Omega_R + \Omega_M + \Omega_\Lambda, \qquad \text{where} \qquad \Omega_i \equiv \frac{\rho_i}{\rho_c} \qquad \text{and} \qquad \Omega_k \equiv -\frac{k}{a^2 H^2}. \tag{1.5}$$

Notice that if the total density of the Universe equals the critical density, then the Universe is flat. If it is less or more, then the Universe is negatively or positively curved, respectively. Today $\rho_c = 10^{-5} h^2$ GeV cm$^{-3}$, where $h \approx 0.7$ is the Hubble parameter in units of 100 Km s$^{-1}$ Mpc$^{-1}$.

Since the Universe is expanding, in other words $a(t)$ is increasing, the matter and radiation densities were much greater in the past. Furthermore, at some point in the Early Universe matter and radiation were in thermal equilibrium due to the rapid collisions of photons with baryonic matter. As time passed, the Universe became cooler and less dense, and eventually photons began a free expansion. Today, these photons -which consequently have a thermal spectrum- are observed as a Cosmic Microwave Background (CMB) with a temperature of $T = 2.725K$ [40]. The moment when the CMB was formed is called recombination era because at this time electrons bound in atomic nuclei and consequently the universe became transparent to light.

Using the Stefan-Boltzmann law, which states that $\rho_\gamma \propto T^4$, one can estimate the radiation density from the temperature of the CMB. In fact, today $\Omega_R h^2 = 4.15 \times 10^{-5}$ [40]. Likewise, a careful analysis of the small temperature fluctuations in the CMB favors $\Omega_k \approx 0$ [40] (see also section 1.2). In contrast, a dedicated study of the expansion of Universe with observations of Type Ia supernovae indicates that $\Omega_M \approx 0.28$ [42–45] ,which according to the Friedmann Eq. (1.5) implies that $\Omega_\Lambda \approx 0.72$. All this conclusively shows the Universe today is made predominantly of dark energy and matter. In section 1.2 it is shown that in fact most of the matter content is not made of baryons -like stars or galaxies- but of a non-baryonic dark matter.

Although today the Universe is dominated by dark energy, at earlier times it was matter-dominated since $\rho_M \propto a(t)^{-3}$, $\rho_R \propto a(t)^{-4}$ and $\rho_\Lambda \propto a(t)^0$. Furthermore, at times even earlier, the Universe was dominated by radiation. The transition between the last two epochs occurred shortly before recombination when the temperature of the Universe was about $1\,\text{eV}$.

In this thesis, we are interested in the temperature dependence of the energy and entropy densities during the radiation-dominated era. These are given by

$$\rho = \frac{\pi^2 g_* T^4}{30}, \qquad s = \frac{2\pi^2 g_* T^3}{45}, \tag{1.6}$$

where $g_*$ stands for the effective number of relativistic degrees of freedom of the thermal plasma at a particular moment. Every bosonic helicity contributes to $g_*$ with a unit, whereas every fermionic helicity contributes with a factor of 7/8. In addition, Eq. (1.3) implies that during the radiation-dominated epoch, the Hubble parameter was given by $H \simeq 1.66\, g_*^{1/2}\, T^2/m_{\mathrm{Pl}}$, where we use $m_{\mathrm{Pl}} = G^{-1/2}$. Here is a good place to mention that along this thesis we only use natural units.

Two more aspects of Standard Cosmology are Big Bang Nucleosynthesis and the anisotropies in the CMB. Because they provide direct evidence for the existence of dark matter, we discuss them in the next section. We also describe the history of radiation in more detail in section 2.4.

## 1.2 Experimental Evidence for Dark Matter

In this section we discuss the experimental facts that support the existence of dark matter. We do not discuss them in the chronological order in which they were discovered or according to the different scales in which they manifest. Instead, we show first the experimental indications of a significant amount of non-visible matter in the Universe, and then we discuss the pieces of evidence that show that such non-visible matter can not be accounted for in the Standard Model of particle physics.

### Virialized Clusters of Galaxies

The first observational evidence for dark matter is often attributed to Fritz Zwicky [46]. In 1933 he applied the virial theorem to estimate the mass of clusters of galaxies and found that in the Coma Cluster there was about two orders of magnitude more mass than was visually observable. Here I repeat his argument very succinctly.

Clusters are non-relativistic groups of galaxies that are bound together by the gravitational force. If Newton's Law of Gravitation is valid up to this scale and if they have reached a state of statistical equilibrium in which individual galaxies are moving but there is no further statistical evolution, then the virial theorem states that

$$2\langle T \rangle + \langle V \rangle = 0. \tag{1.7}$$

If $M$ is the total mass of the cluster, it is possible to write the average kinetic and potential energy as $\langle T \rangle = \frac{1}{2} M \langle v^2 \rangle$ and $\langle V \rangle = -\frac{1}{2} G M^2 \langle \frac{1}{r} \rangle$ respectively, where $\langle v^2 \rangle$ is the mass-weighted average of the square velocity and $\langle 1/r \rangle$ is the corresponding quantity for the inverse separation of the galaxies. As a result, the virial theorem implies that the mass of a cluster is given by

$$M = \frac{2\langle v^2 \rangle}{G \langle 1/r \rangle} \,. \tag{1.8}$$

Now $\langle v^2 \rangle$ can be estimated from the Doppler shift of the galaxies or from the X-ray spectrum of the gas in the cluster. On the other hand, $\langle 1/r \rangle$ can be obtained from measurements of the angular separation between galaxies in the cluster. Moreover, if the absolute luminosity $L$ of the cluster is also measured, one can determine the mass-to-light ratio $M/L$. These estimates have generally given results of order $300\,M_\odot/L_\odot$ (see, *e.g.*, [40]), where $M_\odot$ and $L_\odot$ are the mass and the absolute luminosity of the Sun. These results are approximately one hundred times greater than what is expected if the mass of the galaxies is mostly in stars because -in that case- these should have mass-to-light ratios of order unity in solar units. Based on this argument, Zwicky inferred that there must be some non-visible form of matter in the Coma cluster. Notice that using the same argument, one expects that galaxies account for only one percent or less of the total matter in clusters of galaxies.

**Galaxies Rotation Curves**

Zwicky noted that a similar method could be applied to single galaxies. Nonetheless, a determination of $\langle v^2 \rangle$ was not feasible at that time because it was not possible to get accurate spectroscopic measurements from different parts of a given galaxy. This situation changed since the work of Vera Rubin and her collaborators [47] at end of the 1960's. They worked with a new sensitive spectrograph that could measure the velocity curve of spiral galaxies with a greater degree of accuracy and concluded that most of the mass of these galaxies is also not in luminous stars. Here I show a simplified version of the argument.

If the matter moving in the disk of a spiral galaxy obeys Newton's Law of Gravitation, under the assumption of spherical symmetry, their centripetal acceleration is given by $\vec{a} = -(v(r)^2/r)\hat{r} = -(GM(r)/r^2)\hat{r}$, where $v(r)$ is the rotational velocity of the stars at a distance $r$ from the center of the galaxy and $M(r)$ is the mass enclosed within a sphere of radius $r$. It follows then that

$$M(r) = \frac{r\,v(r)^2}{G}\;. \tag{1.9}$$

This is a generalization of Kepler's Third Law which allows to determine the distribution of mass within spiral galaxies, in analogy to Eq. (1.8). In particular, if most of the mass of a spiral galaxy were in the luminous central regions, then the rotational speeds of stars outside this region would scale as $v(r) \propto 1/\sqrt{r}$. Instead, it is observed that $v(r)$ outside the central region is roughly constant, even beyond the visible disk of the galaxy. This would be expected for a spherical halo with $M(r) \propto r$, in which case most of the mass of the galaxy would be in the dark outer parts of the halo. Thus we find again that there must exist some non-visible form of matter.

**Gravitational Lensing**

Gravitational lensing is the effect by which light coming from a distant source is bent by distributions of mass in between the distant object and the observer. There are three types of gravitational lensing and they are all used in order to infer the existence of dark matter and study its properties.

**1. Strong Lensing:**  Galaxy clusters are massive enough to significantly bend light coming from galaxies behind them. Since the effect is determined by the mass distribution, it is possible to estimate the mass of the clusters for which this effect is observed by measuring the geometrical distortions. In general, what is obtained is in agreement with mass measurements based on the virial theorem or X-rays spectroscopy (see below). Furthermore, if the luminosity is also determined, the resulting mass-to-light ratios are orders of magnitude greater than the corresponding quantity for visible parts of galaxies, in agreement with observations based on the virial theorem, and therefore with the existence of non-luminous matter. One remarkable example of this is given by the galaxy cluster Abell 1689 (see, *e.g.*, [48]).

**2. Weak Lensing:**  Although light is bent by any mass distribution according to general relativity, this effect seldom forms big arcs or multiple images like in the case of strong lensing. However, even when the effect is very small, the presence of masses in between the observer and sources can be detected by analyzing large numbers of sources in order to find coherent distortions (see, *e.g.*, [40]). These measurements have been used to map out the distribution of dark matter in many clusters of galaxies. A remarkable example is the bullet cluster, which is discussed below.

**3. Microlensing:**  As opposed to the cases discussed previously, here the mass of the lens is too small to produce a visible displacement of light. However, if the massive object is compact enough the effect of the lensing is observed by an apparent brightening of the source, which can take place on human time-scales, and therefore detected in order to determine mass distributions. By using this method in the Milky Way, it has been argued that the dark matter of the halo can not be composed of massive compact objects -such as planets or brown dwarfs- with masses in between $10^{-7} M_\odot < M < 15 M_\odot$ [49].

Now, we discuss experimental evidence suggesting that this non-visible matter can not be made of protons or neutrons.

**X-rays from Clusters of Galaxies**

Because only baryonic matter can emit light in a cluster of galaxies, it is possible to establish the ratio of the amount of baryonic dark matter to the total non-relativistic matter by studying its X-ray emission. Moreover, in these studies, it is assumed that the pressure and the gravitational force balance each other out. Assuming spherical symmetry, at a distance $r$ from the center, this can be written as

$$p_B(r + dr) - p_B(r) = -G \frac{(\rho_B(r) \, dr) \left( \int_0^r 4\pi r'^2 \rho_M(r') dr' \right)}{r^2}, \tag{1.10}$$

here $\rho_B$ and $p_B$ are the density and the pressure of the baryonic dark matter whereas $\rho_M$ is the total density of the non-relativistic dark matter. Accordingly, the right-hand side of the previous equation is the force (per unit of area) felt by an infinitesimal portion of the baryonic matter

due to the non-relativistic matter enclosed within a radius $r$. If one assumes that the baryonic matter behaves as an ideal gas and that its temperature is $T_B$, then $p_B(r) = k\rho_B(r)T_B(r)/m_B$, which can be used to write the hydrostatic equilibrium equation (1.10) as

$$\frac{d}{dr}\left[\frac{r^2}{\rho_B(r)}\frac{d}{dr}\left(\frac{k\rho_B(r)T_B(r)}{m_B}\right)\right] = -4\pi G r^2 \rho_M(r). \tag{1.11}$$

Now, X-rays coming from clusters of galaxies are produced only by the baryonic matter in their hot gas. In fact, from the X-ray spectra it is possible to determine the temperature $T_B$ of the baryons. Moreover, from the luminosity of the X-rays and the temperature it is possible to infer the baryonic density $\rho_B$. All this information can be plugged in Eq. (1.11) to determine the total density of non-relativistic matter. Using this method it is found that [40] within clusters of galaxies $\Omega_B/\Omega_M \approx 0.12$. Therefore only about 10% percent of the matter in galaxies clusters is baryonic.

**Big Bang Nucleosynthesis**

Soon after the formation of protons and neutrons in the Early Universe, these particles were present in equal amounts because weak interactions allow proton-neutron conversion by means of the processes $n \rightleftharpoons p + e^- + \bar{\nu}$, $n + \nu \rightleftharpoons p + e^-$ and $n + e^+ \rightleftharpoons p + \bar{\nu}$. However, when the temperature of the Universe dropped below approximately 1 MeV, the neutron-proton ratio started decreasing not only because of the Boltzmann suppression for the neutron density but also because of the disappearance of the electron-positron pairs. Eventually this conversion of neutrons into protons was stopped by the formation of heavy nuclei, in which neutrons are stable. A detailed analysis of how and when these processes took place allows to infer the primordial abundance of nuclei. In particular, for protons -or hydrogen $^1$H- it is predicted a primordial mass abundance of around 75%, and for helium $^4$He a mass abundance of about 25%, along with small amounts of deuterium $^2$H, helium $^3$He and lithium $^7$Li. These predictions have been accurately confirmed by observations [50]. Although the exact value of the initial baryon density does not affect the overall picture, an accurate measurement of the deuterium-hydrogen ratio does allow to infer the initial baryon density with great precision. Such measurements imply a ratio of the baryon density to the critical density of $\Omega_B \approx 0.045$. This value is much less than the fraction that all non-relativistic matter contributes to the critical density $\Omega_M \approx 0.28$, which can be inferred from studies of galaxies clusters or from the redshift-distance relation of type Ia supernovae. It is this discrepancy that provided the original evidence for non-baryonic dark matter in the universe [40].

**Anisotropies in the Cosmic Microwave Background (CMB)**

At some point in the Early Universe, matter and radiation were in thermal equilibrium due to the rapid collisions of photons with baryonic matter. As time passed, the Universe became cooler and less dense, and eventually photons began a free expansion. Today, these photons -which

consequently have a thermal spectrum- are observed as a Cosmic Microwave Background (CMB). Since these photons originated in the Early Universe, the CMB is highly isotropic. However, small anisotropies in the CMB were also formed during the Early Universe due to acoustic oscillations in the primordial plasma. The interactions responsible for these oscillations are the gravitational and the electromagnetic interactions. Although baryonic matter and dark matter were both non-relativistic at the time CMB was formed and therefore indistinguishable from a gravitational point of view, they interacted differently with photons. Hence baryonic and dark matter had different effects on the acoustic oscillations. Accordingly, the power spectrum of the CMB anisotropies shows different effects for baryonic matter and dark matter. In particular, the first peak of the CMB power spectrum -which is the largest- is related mostly to the density of baryonic matter, whereas the third one is associated mostly to the density of dark matter. These and other effects in the CMB anisotropies have been investigated by a large number of experiments. In particular, from the relative heights of the acoustic peaks in the CMB, the Planck collaboration has determined the following values for the ratios of the baryonic and the dark matter densities to the critical density [35]

$$\Omega_B h^2 = 0.02207 \pm 0.00033 \qquad \text{and} \qquad \Omega_{DM} h^2 = 0.1196 \pm 0.0031 \ . \qquad (1.12)$$

This conclusively shows that the amount of baryonic matter is less than the dark non-baryonic matter content of the Universe. In fact, dark matter constitutes 84.5% of the total matter.

### The Bullet Cluster

The double galaxy cluster 1E0657-558, commonly known as the Bullet Cluster provides one of the most vivid pieces of evidence for the existence of dark matter, or more precisely, of a form of matter that does not have non-gravitational interactions with baryonic matter. The bullet cluster consists of two colliding subclusters, whose major components are galaxies, hot gas and dark matter [51]. The galaxies -which as argued before account for around one percent of the total matter- are mostly grouped in the two distinct visible regions. In contrast, using X-rays techniques, the hot gas is observed in the region in between these two subregions. Finally, using weak lensing techniques, it is possible to infer that the dark matter also forms two subclusters that are almost coincident with the galaxies. The interpretation is that two clusters collided. On the one hand, the hot gas belonging to both clusters slowed much more than the galaxies and the dark matter due to the electromagnetic interaction among the baryons; on the other hand, the galaxies due to their smaller density had little chance of close encounters and therefore continued mostly on their original paths. One therefore concludes that the dark matter continued along its original path because it interacts weakly with ordinary matter. In particular, the dark matter component might not interact electromagnetically, which explains why it can not emit light. Furthermore, although some of the evidence for non-luminous matter can also be interpreted as a failure of Newton's Gravitational Law at large scales, the bullet cluster makes this interpretation unlikely. In fact, at a statistical significance of $8\sigma$, it was found that the spatial offset of the

center of the total mass from the center of the baryonic mass subregions can not be explained with a modification of the gravitational force law [51].

## 1.3 The Dark Matter Particle

Big Bang Nucleosynthesis allows to conclude that most of the matter in the universe can not be made of baryons, that is, of protons or neutrons. This conclusion is reinforced by studying the anisotropies in the CMB and by a careful analysis of the Bullet cluster. We conclude that some other form of matter exists. Although the nature of this new form of matter is currently unknown, some its properties are well-established:

- It must be dark. This means that dark matter can not interact significantly with photons, otherwise we could see dark matter directly in astronomical observations. An immediate consequence of this is that the new form of matter can not be electrically charged.

- It can not be made of protons or neutrons.

- It must be stable at cosmological scales, otherwise dark matter would not be abundant today, in contrast with astrophysical and cosmological observations.

- It must have been cold enough to allow for structure formation in the early universe. Cold here does not refer to an actual temperature but instead refers to how slow the dark matter moved at the moment when the first structures started to form. In particular, hot dark matter candidates -such as neutrinos- have been ruled out because they can not form large-scale structures in agreement with observations [52].

- As explained above, microlensing observations indicate that a significant amount of dark matter is not made of massive compact objects such as planets or brown dwarfs.

- Experimental limits on the the scattering cross section between dark matter and ordinary matter suggest that it is unlikely for dark matter to have color charge (see, *e.g.*, [53]).

All this supports the existence of a particle that is not described in the Standard Model of particle physics. Such particle must be electrically neutral, colorless, stable on cosmological scales and massive enough to have been cold during the formation of the first structures in the Early Universe.

There is a plethora of models of physics beyond the Standard Model that attempt to describe this particle. An incomplete list of popular models is: sterile neutrinos [54], the sneutrino, the neutralino and the gravitino in the context of supersymmetric theories [55–59], axion dark matter models [60–65] , Minimal Dark Matter scenarios [24, 66, 67], the Inert Doublet Model [6–18], Kaluza-Klein dark matter models [68–72] (see [5] for comprenhensive list) . In this work three models will be discussed, they are introduced in chapters 3, 7 and 8. Their common feature is the presence of additional scalar particles.

In general, all these models include more new particles besides the one that accounts for the dark matter. In fact, these new particles -the dark sector- make the dark matter phenomenology very rich even when the dark sector is intrinsically simple. The additional particles might be divided in three groups

1. Particles much heavier than the dark matter. In general these particles do not contribute to the dark matter phenomenology. In fact, in most cases these particles can be integrated out from the effective theory describing the dark matter. For instance, this is the case of the heavy supersymmetric particles in the MSSM.

2. Particles slightly heavier than the dark matter particle. These particles strongly influence the dark matter phenomenology. In this work we concretely study three examples of this: coannihilations for the production of dark matter in chapters 3 and 7, virtual internal bremsstrahlung in chapter 4, and finally Sommerfeld enhancement between different pairs of particles in chapter 5.

3. Light particles. The dark sector may contain particles lighter than the dark matter. For instance, a distinctive prediction of the models introduced in part III is the existence of (pseudo-)Goldstone bosons. These light particles may contribute to the radiation energy density of the Universe and consequently have been dubbed dark radiation.

In the next chapter we give a general overview of these ideas.

# Chapter 2

# The Dark Sector

As mentioned in chapter 1, dark matter models generally include more new particles besides the one that describes dark matter. The set of all of them constitutes the dark sector. In this chapter we investigate dark sectors with a $Z_2$ symmetry. We also study those with relativistic particles, which we call dark radiation.

## 2.1 Stability of Dark Matter and the Symmetries of the Dark Sector

One of the most striking features of the dark matter particle is its long lifetime, longer than the age of the Universe - about $10^{18}$ seconds - and possibly much longer as indicated by the non-observation of its decay products in cosmic ray experiments [73], for instance longer than about $10^{26}$ seconds if antiprotons are produced copiously when the dark matter decays. This observation suggests that the dark matter particle is stable.

As shown in Table 2.1, in the Standard Model the stability of all the particles can be explained in terms of a symmetry principle. The photon is stable because it is the massless gauge boson associated to the exact $U(1)_{\rm em}$ gauge symmetry. Similarly, the electron is stable because it is the lightest particle with electric charge, and its decay would violate the $U(1)_{\rm em}$ symmetry. In addition, the lightest neutrino is stable because it is the lightest particle with half-integer spin, and hence Lorentz symmetry - or more precisely quantum angular momentum conservation-forbids its decay. And finally, the proton is stable because it is the lightest particle with baryonic number, and therefore $U(1)_{\rm B}$ symmetry forbids its decay. Likewise, one would expect that the longevity of the dark matter particle is likely due to the existence of a preserved, or very mildly

| Particle | Symmetry |
|---|---|
| Photon | Gauged $U(1)_{\rm em}$ |
| Electron | $U(1)_{\rm em}$ |
| Lightest Neutrino | Lorentz Symmetry |
| Proton | $U(1)_{\rm B}$ |
| Dark Matter | $Z_2, U(1)_{\rm DM}, ...$ |

Table 2.1: Symmetries associated to the stability of each particle of the Standard Model.

broken, symmetry.

Many popular dark matter models rely on this assumption. For instance, in the MSSM the lightest supersymmetric particle -which is assumed to be a dark matter candidate- is stable due to $R-$parity, which for any particle of spin $S$, lepton number $L$ and baryon number $B$ is given by $R = (-1)^{2S+3(B-L)}$. With this charge assignment all the supersymmetric particles of the MSSM are odd under $R-$parity while the SM particles are even. Although this symmetry was originally introduced to forbid certain interactions that lead to proton decay, it was soon realized that $R-$parity guarantees the stability of the lightest supersymmetric particle and therefore provides a dark matter candidate. Another example is given by Minimal Dark Matter models. Here the symmetry group is the same of the Standard Model. Nevertheless, an accidental symmetry at renormalizable level arises when the dark matter belongs to a high $SU(2)_L$ multiplet. In the IDM, to be discussed in part II, the dark matter particle belongs to a gauge multiplet with the same quantum numbers of the Standard Model scalar, but it is charged under a $Z_2$ symmetry group. For a comprehensive review of similar examples (see, *e.g.*, [29]).

From now on, for the sake of simplicity and because it is the case of the models discussed in this thesis, we assume that a $Z_2$ symmetry ensures the stability of the dark matter.

### 2.1.1 The $Z_2$ Symmetry

The discrete group $Z_2$ describes the behavior of even and odd integers under addition. This is a group operation because the addition of two even numbers or two odd numbers is even and the addition of an even and odd number is odd. Accordingly, the representations of this group are also called even and odd. Notice that this group is isomorphic to the set $\{1, -1\}$ along with the number multiplication.

The $Z_2$ group is the simplest non-trivial group and in fact it can be used to ensure the absolute stability of dark matter if all the Standard Model particles are even under this group while the dark matter particle -and possibly other particles- are odd. Furthermore, it is necessary to assume that dark matter corresponds to the lightest odd particle because, in that case, the dark matter can not decay into lighter particles.

### 2.1.2 Postulated or Derived from First Principles?

This discrete symmetry in the Lagrangian could be imposed by hand. Nevertheless, it is desirable to give an explanation for the origin of such symmetry. For instance, this symmetry could arise as a remnant of the breaking of a global continuous symmetry. Indeed, if a global $U(1)$ symmetry is spontaneously broken by a scalar field with charge 2 in units of the smallest $U(1)$-charge, a discrete $Z_2$ symmetry automatically arises in the Lagrangian. Moreover, all the fields with even (odd) charge under the global group will acquire, after the spontaneous symmetry breaking, an even (odd) discrete charge under the $Z_2$ transformation [30]. Therefore, the lightest particle with odd charge is absolutely stable and a potential candidate for dark matter. This is the case of the models discussed in this work in part III.

## 2.2 Dark Matter Annihilation in the Early Universe and its Abundance Today

Although the $Z_2$ symmetry in the dark sector forbids the decay of dark matter particles, a pair of them may annihilate without violating such discrete symmetry. As a consequence, the number of dark matter particles is not conserved. Nevertheless, as we show in this section, the abundance of dark matter today does not depend on the initial conditions of the Universe as long as it was in equilibrium with the rest of particles at some point. When this happens, we say that the dark matter has been thermally produced [40, 74–77].

### 2.2.1 Thermal Production of Dark Matter

Dark matter annihilations occurred more often in the Early Universe because its density was much higher back then. Moreover, the inverse processes also took place when the thermal energy of ordinary particles was high enough to produce dark matter pairs. Thus, at that point, the dark matter number density $n_{DM}$ was given by the chemical equilibrium conditions of the primordial plasma, or equivalently, by a Boltzmann distribution, which is proportional to the temperature to the third power for relativistic particles. Because the comoving volume is inversely proportional to $T^3$, this means that the dark matter density only changed due to the expansion of the Universe.

However, soon after the temperature dropped below the dark matter mass, it was not possible for the lighter particles to annihilate into dark matter pairs and consequently the density of dark matter decreased faster than $T^3$. Moreover, at some point the abundance of dark matter was so little, that the equilibrium between lighter particles and dark matter did not exist anymore. This point is called freeze-out. As a matter of fact, since the annihilation rate is proportional to the density, at some point this became smaller than the expansion rate of the Universe, that is, the annihilation process stopped being efficient and hence the dark matter density changed again only due to the expansion of the Universe, and therefore became proportional to $T^3$ as before. When the Universe became matter dominated, the critical density also became proportional to $T^3$ and therefore $\Omega_{DM}$ became constant.

Since $\Omega_{DM}$ can be measured very precisely, invoking thermal production of dark matter in a particular model constrains severely its parameter space. Because of this reason, it is essential to study such mechanism quantitatively. This can be done by means of the Boltzmann equation.

### 2.2.2 The Boltzmann Equation

Suppose that there are $N$ particle species, that have an odd charge under the $Z_2$ symmetry, and that each of them has a density equal to $n_i$, where $i = 1, ...N$. The lightest among these particles corresponds to the dark matter. We now derive the Boltzmann equation that describes the total density of odd particles $n = \sum_{i=1}^{N} n_i$.

**The simplest case.** For the sake of illustration, we consider first the case of $N = 1$ and constant annihilation cross section $\sigma v$. Then, the dark matter annihilation rate per particle is given by $n\sigma v$, where $v$ is its relative velocity. The number of particles in a comoving volume is $na^3$, and hence the decrease rate of dark matter particles in such volume is $(na^3)(n\sigma v)$. Since the thermal plasma also creates particles at rate $\mathcal{G}$ the total rate is $d(na^3)/dt = -(na^3)(n\sigma v) + \mathcal{G}$. Since in equilibrium this rate is zero we have that $\mathcal{G} = (n^{eq})^2 a^3 \sigma v$ and consequently $d(na^3)/dt = -(n^2 - (n^{eq})^2)a^3\sigma v$. Using the fact that the Hubble parameter is $H = \dot{a}/a$, we conclude [74]

$$\frac{dn}{dt} + 3H\,n = -\sigma v(n^2 - (n^{eq})^2)\,. \tag{2.1}$$

This is the Boltzmann equation for the case when $N = 1$ and $\sigma v$ is independent of the velocity. Here $n^{eq}$ is the equilibrium density given by the Boltzmann distribution of a particle of mass $M$ and $g$ internal degrees of freedom

$$n^{eq} = \frac{gM^2T}{\pi^2}K_2\left(\frac{M}{T}\right)\,, \tag{2.2}$$

where $K_n(x)$ is the modified Bessel function of the second kind of $n$th order.

**General case.** The general case requires some modifications. If the cross section depends on the velocity of the dark matter, it is necessary to perform an average over the dark matter velocity, or equivalently, a thermal average. Furthermore, if there are many particles charged under the $Z_2$ group, it is necessary to introduce an effective annihilation cross section [78]

$$\langle\sigma_{\text{eff}}v\rangle = \sum_{i,j=1}^{N}\langle\sigma^{ij}v\rangle\frac{n_i^{eq}}{n^{eq}}\frac{n_j^{eq}}{n^{eq}}, \tag{2.3}$$

with

$$\langle\sigma^{ij}v\rangle = \frac{\int_{(M_i+M_j)^2}^{\infty}\frac{ds}{\sqrt{s}}K_1\left(\frac{\sqrt{s}}{T}\right)(s-(M_i+M_j)^2)(s-(M_i-M_j)^2)\sigma(ij\to\text{all})}{8TM_i^2M_j^2K_2(\frac{M_i}{T})K_2(\frac{M_j}{T})}\,, \tag{2.4}$$

$$n_i^{eq} = \frac{g_iM_i^2T}{\pi^2}K_2\left(\frac{M_i}{T}\right) \qquad\text{and}\qquad n^{eq} = \sum_i n_i^{eq}. \tag{2.5}$$

Here $g_i$ is the particle internal degrees of freedom. In terms of these quantities, the generalization of the Boltzmann Eq. (2.1) reads

$$\frac{dn}{dt} + 3H\,n = -\langle\sigma_{\text{eff}}v\rangle(n^2 - (n^{eq})^2)\,. \tag{2.6}$$

For the models that are considered in this work, we solve the Boltzmann Eq. (2.6) using micrOMEGAs 3.1 [79]. The solution gives the total density of particles that are charged under $Z_2$ group. All these particles must eventually decay into the dark matter. As a result, $n$ corresponds to the dark matter density $n_{DM}$ today. From this, the dark matter energy density

$\rho_{DM} = M_{DM}n_{DM}$ can be calculated and, if this quantity is divided by the critical density, one obtains the relic density $\Omega_{DM}$.

In general, not all the particles that are charged under the $Z_2$ group should be included in the Boltzmann equation because the equilibrium densities, given in Eq. (2.5), are proportional to $K_2(M_i/T)$ which decays exponentially with the mass. As a consequence, it is a very good approximation to include only the dark matter and the particles whose mass is similar to dark matter mass in the Boltzmann equation. These particles are called the coannihilating species.

### 2.2.3 Instantaneous Freeze-out Approximation

In general, a full integration of the Boltzmann equation is needed in order to calculate the relic density. Nonetheless, an approximate solution - the so-called instantaneous freeze-out approximation [80]- can be applied under the following circumstances:

- When the annihilation process is not mediated by resonances.

- When the annihilation process is not close to a kinematical threshold. In other words, when the total mass of the annihilating particles and the total mass of the annihilation products are not close to each other.

Then it is possible to identify two regions where the Boltzmann equation can be solved analitically. On the one hand, at very early times when the temperature was much higher than the dark matter mass, its density was given by the Boltzmann distribution $n^{eq}$, because under that circumstance - as explained before- $n^{eq} \propto T^3 \propto 1/a^3$ and $n = n^{eq}$ is a solution of Eq. (2.5). On the other hand, for temperatures much smaller than its mass, the density of dark matter deviated from the equilibrium density, in fact $n \gg n^{eq}$. Then, the two conditions from above can be used to prove [80] that there was transition between the two regions corresponding to the moment when the dark matter density started deviating from the the equilibrium distribution. This transition is called the freeze-out. The temperature at which it happened can be estimated by comparing the annihilation rate with the expansion rate, that is, by solving

$$\left.\frac{n^{eq}\,\langle\sigma v\rangle_{\text{eff}}}{H}\right|_{T=T_f} \approx 1, \tag{2.7}$$

which implies that the freeze-out temperature $T_f$ implicitly satisfies

$$x_f \sim \log\left(\frac{0.038 g_{DM} m_{\text{Pl}} M_{DM}\langle\sigma_{\text{eff}}v\rangle}{g_*(x_f)^{1/2}x_f^{1/2}}\right), \qquad \text{where} \qquad x_f = M_{DM}/T_f. \tag{2.8}$$

From the general discussion at the beginning of this section, one expects $x_f > 1$. In fact, typically $x_f \approx 20 - 30$, and therefore dark mater is non-relativistic at $T_f$.

After the freeze-out, the equilibrium density was much smaller than $n$ in Eq. (2.6). Consequently $n^2 - n^{eq2} \approx n^2$ and the resulting expression can be integrated from the freeze-out to the present.

In fact one obtains that

$$n(t_0) = \frac{1}{a(t_0)^3 \left( \frac{1}{n(t_f)a(t_f)^3} + \int_{t_f}^{t_0} \frac{\langle \sigma_{\text{eff}} v \rangle dt}{a(t)^3} \right)} \simeq \frac{1}{a(t_0)^3 \int_{t_f}^{t_0} \frac{\langle \sigma_{\text{eff}} v \rangle dt}{a(t)^3}}. \tag{2.9}$$

Recalling that during the radiation-dominated era $H = 1.66 \, g_*^{1/2} T^2 / m_{\text{Pl}}$ and that $\rho_c = 10^{-5} h^2 \, \text{GeV} \, \text{cm}^{-3}$, one finds that the dark matter relic density is approximately equal to

$$\Omega_{\text{DM}} h^2 = \frac{M_{DM} \, n(t_0)}{\rho_c / h^2} \tag{2.10}$$

$$\simeq \frac{1.07 \times 10^9 \, \text{GeV}^{-1}}{J(x_f) \, g_*(x_f)^{1/2} \, m_{\text{Pl}}} = \frac{1.02 \times 10^{-27} \, \text{cm}^3 \text{s}^{-1}}{J(x_f) \, g_*(x_f)^{1/2}}, \tag{2.11}$$

where $J$ is called post freeze-out annihilation integral and is given by

$$J(x_f) = \int_{x_f}^{\infty} \frac{\langle \sigma_{\text{eff}} v \rangle}{x^2} \, dx. \tag{2.12}$$

Suppose now that there are no coannihilations, resonances or kinematical thresholds. Furthermore, assume a constant annihilation cross section $\sigma v$ so that the post freeze-out annihilation integral can be solved. Then Eq. (2.11) gives the annihilation cross section as a function of the dark matter abundance. For $\Omega_{DM} h^2 = 0.1196$ and $g_*(x_f) \sim 100$, one obtains

$$\sigma v \simeq 3 \times 10^{-26} \text{cm}^3 \text{s}^{-1}. \tag{2.13}$$

This is the so-called thermal cross section and it is the expected value for the simplest case but it does not apply in general. Moreover, this cross section is of the same order of magnitude as the weak interaction cross sections of particles with masses around the electroweak scale. This supports the hypothesis that dark matter is in fact made of a weakly interacting massive particle (WIMP). In fact, the thermal production of dark matter is generally associated to WIMPs.

Since at the freeze-out dark matter is non-relativistic, the effective thermal cross section $\langle \sigma_{\text{eff}} v \rangle$ can be expanded in the velocity. In fact,

$$\langle \sigma^{ij} v \rangle = a + 6 \left( b - \frac{a}{4} \right) \frac{1}{x}, \qquad \text{if} \qquad \sigma^{ij} v = a + b v^2. \tag{2.14}$$

The first term in this expansion is called the s-wave and the second term the p-wave.

In chapters 3, 7 and 8, we apply the formalism of this section in order to calculate the dark matter relic abundance for the different models under consideration in this thesis.

## 2.3 Dark Matter Searches

In spite of its gravitational effects in the dynamics of galaxies, clusters of galaxies or in the Universe at large scale, dark matter has not been observed on Earth. In this section we describe some search strategies that are currently pursued in order to achieve that goal. In particular, we describe direct and indirect dark matter experiments. For others, in particular collider searches, see [5].

### 2.3.1 Direct Detection Experiments

A very promising search strategy of dark matter goes under the name of direct detection (For a comprehensive review see [5]). This sort of experiments aims at detecting WIMPs through the observation of their recoil off atomic nuclei [81]. In fact, if the Milky Way dark matter halo is made of WIMPs, the motion of the earth across the galaxy can produce a flux of WIMPs sufficiently large so that some of them elastically scatter off nuclei. In fact, those recoils can be detected by measuring the ionization of atoms struck by the recoiling nucleus, or by counting the photons emitted by these atoms, or by measuring the vibrations in the crystal lattice of the detector. Moreover, failing to observe nuclear recoil events excludes regions in the plane direct detection cross section vs. dark matter mass. As of 2014, the best limits on this plane has been provided by the LUX collaboration [82]. In chapters 6, 7, 8 and 10, we consider these limits in order to constrain the parameter space of the models of this thesis.

### 2.3.2 Indirect Detection Experiments and Photons from Dark Matter Annihilations

Dark matter particles may annihilate without violating the $Z_2$ symmetry. As shown in section 2.2, this property is essential to understand the thermal production of dark matter in the Early Universe. In particular, a detailed analysis of dark matter annihilations allows to establish when their rate became smaller than the expansion rate of the Universe and therefore when annihilations effectively stopped taking place, leading to the abundance of dark matter that is observed today.

While annihilations no longer continue on the whole Universe, they may still go on in those regions where the density of dark matter is relatively large. In fact, searching for the products of theses annihilations is another promising method to identify dark matter and its properties. Experiments with this aim are called indirect detection experiments because they do not attempt to detect dark matter directly but only its annihilation products. For a review see [5].

The general idea goes as follows. Somewhere in the Universe where its density is high, dark matter annihilates into some particles and these in turn decay producing a flux of photons, electrons, protons, positrons, antiprotons and/or (anti-)neutrinos. Subsequently, these propagate from the point where they are produced until they reach the earth. Among all of them, photons play a significant role because of two reasons. On the one hand, because they propagate basically unperturbed and hence they directly point to their source. On the other hand, and more importantly, because the photon spectra typically exhibits spectral features.

The photon flux produced in dark matter annihilations and received at Earth from a given solid angle in the sky, $\Delta\Omega$, is given by

$$\frac{d\Phi_\gamma}{dE_\gamma} = \frac{1}{8\pi} \left( \frac{1}{\Delta\Omega} \int_{\Delta\Omega} J d\Omega \right) \left( \frac{\langle \sigma v \rangle}{M_{DM}^2} \sum_f B_f \frac{dN^f}{dE_\gamma} \right) , \tag{2.15}$$

where the $J$-factor is the integral of the squared dark matter density $\rho_{DM}$ along the line of sight $J = \int_{\text{l.o.s.}} ds \rho_{DM}^2$, $B_f$ the branching ratio into a channel $f$, and $N^f$ the number of photons per

annihilation associated to that channel at a particular energy. The second parenthesis includes the particle physics input, that is, the photon spectrum $dN^f/dE_\gamma$ and the cross sections into gamma-rays of each individual annihilation channel. In contrast, the first parenthesis includes all the astrophysics information, in particular the distribution of the dark matter whose annihilation gives rise to gamma-rays. Although other targets can be used, in this thesis we consider only dark matter annihilations in the center of the Milky Way.

In our galaxy, two popular dark matter distributions are the Einasto profile, favored by recent $N$-body simulations [83–85],

$$\rho_{\text{DM}}(r) \propto \exp\left[-\frac{2}{\alpha}\left(\frac{r}{r_s}\right)^\alpha\right] \tag{2.16}$$

with $r_s = 20$ kpc and $\alpha = 0.17$ [86,87], as well as the Navarro-Frenk-White (NFW) profile [88,89]

$$\rho_{\text{DM}}(r) \propto \frac{1}{(r/r_s)[1 + (r/r_s)]^2} \,, \tag{2.17}$$

with scale radius $r_s = 21$ kpc [90], both profiles normalized to a local dark matter density $\rho_{\text{DM}}(r = 8.5 \text{ kpc}) = 0.39 \, \text{GeV cm}^{-3}$ [91–94]. Here we have assumed that the distance from the earth to the galactic center is 8.5 kpc.

Notice that the gamma-ray flux is proportional to the dark matter annihilation cross section. This can be expanded on partial waves: $\sigma v = a + bv^2$, because dark matter is non-relativistic today. As we discussed before, the first term in this expansion is called the s-wave and the second term the p-wave. If the first term does not vanish, the gamma-ray flux is not suppressed by $v^2$. In contrast, if the s-wave vanishes, or equivalently if the dark matter annihilates via p-waves, the flux is suppressed and in general very small. Therefore, the phenomenology of indirect dark matter detection crucially depends on whether the annihilation proceeds via s-waves or p-waves. We will see an example of this in chapter 10.

We now discuss the gamma-ray spectra. If dark matter annihilates producing quarks, leptons, gauge or Higgs bosons, then their hadronization and further decay create a soft featureless photon spectrum with a cutoff at the kinematical energy limit, which is the dark matter mass. This spectrum is universal in the sense that it is very similar for almost all the final states and depends very weakly on the mass (if the energy is normalized with respect to it). Since the astrophysical background, which is not well understood, is also soft and extends over many orders of magnitude, it is very difficult to claim a discovery of dark matter based only on signals like this one.

In contrast, there are at least three known processes that give rise to features in the photon spectrum which are directly related to dark matter properties, in particular, to its mass. We show examples of these processes in Fig. 2.1.
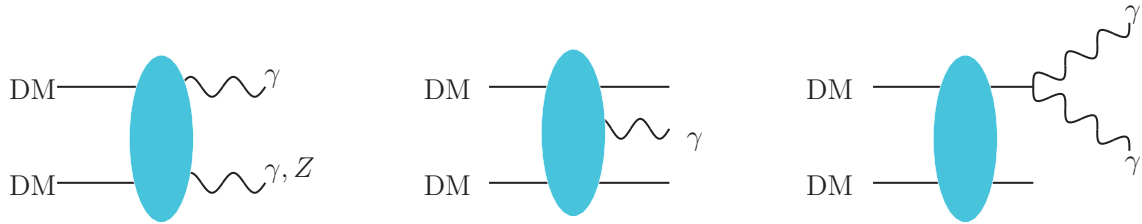
Figure 2.1: Example of three known processes that lead to spectral features in the photon spectrum: annihilation into photons (left), VIB (center) and gamma-ray boxes (right).

**Monochromatic Lines**

The simplest and best known case corresponds to monochromatic lines coming from dark matter annihilations [10, 72, 95–102]. An example of this is shown on Fig. 2.1 on the left. Indeed, if dark matter annihilates into a particle of mass $m$ and a photon, conservation of energy-momentum indicates that the energy of the latter in the center of mass frame is

$$E_\gamma = M_{DM} \left( 1 - \frac{m^2}{4M_{DM}^2} \right). \tag{2.18}$$

If the dark matter is a WIMP, this photon shows up as a line in the gamma-ray spectrum. Moreover, the line coincides with the dark matter mass, provided that this is much greater than $m$. Because known astrophysical processes do not produce monochromatic high-energy gamma-rays, it is practically impossible for the astrophysical background to mimic a signature like this. As a consequence, this spectral feature is usually considered a smoking-gun evidence of dark matter.

Since dark matter does not couple to photons directly, unfortunately these processes are generally loop-suppressed and the expected flux in Eq. (2.15) is generally small. In this work and in particular in chapters 4 and 6 we study monochromatic lines in the IDM.

**Virtual Internal Bremsstrahlung (VIB)**

Although dark matter can not couple to photons directly, it can couple to charged particles, and these can subsequently emit photons. As a result, dark matter annihilations at tree-level can produce photons as long as the final state has at least three particles. Accordingly, in this case there is no loop suppression but there is a phase-space suppression in comparison with the two-body final state of monochromatic lines.

An example of this sort process is shown in the central part of Fig. 2.1. Photons emitted in this way can be classified in two categories: as final state radiation and as virtual internal bremsstrahlung (VIB) [71, 103–112]. In the former case, photons are emitted from final state particles, whereas in the second case they are emitted from charged virtual states. We stress however that these definitions are not completely rigorous because emissions from individual

Feynman diagrams are not gauge-invariant in general. In fact, when there is VIB, there is typically final state radiation as well. Nevertheless, the converse is not true, and therefore speaking of only final state radiation is justified.

In general, final state radiation is dominated by collinear photons and the spectrum is therefore roughly model independent and characterized by a sharp cut-off at its kinematical end-point. On the other hand, VIB can produce line-like spectral features under certain circumstances:

- When the three-body state satisfies a symmetry of the initial state that cannot be satisfied by the two-body final state. For instance, this is the case of Majorana dark matter annihilation into chiral fermions, where the initial and final state necessarily have different helicities, and the emission of a photon anti-parallel to the chiral fermions restores the symmetry of the initial state. Moreover, the kinematics of this process allows only photons with energies close to the dark matter mass, and therefore in this case the gamma-ray spectrum presents a bump at its end-point.

- Line-like features in the spectrum can also be produced when the final state consists of bosons and there is a charged particle in the t-channel whose mass is similar to the one of the dark matter [105]. In this work and in particular in chapters 4 and 6 we study an example of VIB for the IDM, where this situation takes place.

**Boxes**

Likewise, a box-shaped photon spectrum is produced if dark matter annihilates into two intermediate neutral scalar particles and then these decay into photons. This can be understood from the fact that the intermediate particles have a fixed energy in the center of mass, but the photons that are produced in their decay might have different energies depending on the directions in which they are emitted with respect to the intermediate particle. From this argument one can see that that box is centered around half the dark matter mass and its width is determined by the mass of the intermediate particle.

Moreover, due to the resolution of the gamma-ray instruments, the box spectrum can resemble a line in certain limits as argued in [113], providing therefore another class of spectral feature. An example of this sort of processes is shown on Fig. 2.1 on the right. In chapter 10 we study an example of gamma-ray boxes. In this particular case, dark matter annihilates into a pseudo-Goldstone boson which subsequently decays into two photons.

## 2.4  Dark Radiation

Any relativistic particle in the dark sector that contributes to the radiation density of the Universe can be called dark radiation. Before discussing this topic in detail, we review the history of radiation in Standard Cosmology.

When the temperature of the Universe dropped below the muon mass, only photons, neutrinos, electrons and positrons were relativistic and therefore only they contributed to the radiation density of the Universe. Moreover, all these particles were in equilibrium due to electroweak interactions. In fact, weak processes such as $e^+e^- \rightleftharpoons \nu\bar{\nu}$ kept neutrinos in equilibrium with the positrons and electrons, which were in turn in equilibrium with photons. Nevertheless, the neutrinos decoupled from the rest of particles once the weak interactions were no longer efficient compared to the expansion rate of the Universe. Indeed, the neutrino decoupling happened when

$$\left. \frac{n_\nu^{eq} \, \langle\sigma v\rangle_{\nu\bar{\nu}\to e^+e^-}}{H} \right|_{T=T_\nu^d} \approx 1 \, . \tag{2.19}$$

Here $n_\nu^{eq}$ is the equilibrium density of neutrinos and $T_\nu^d$ is the temperature at which the decoupling took place. A careful analysis of the previous equation allows to conclude that $T_\nu^d \simeq 2-3$ MeV [40, 114–116].

Subsequently, at the end of the neutrino decoupling epoch, when the temperature of the Universe dropped below the electron mass, positrons could no longer be thermally produced and therefore disappeared from the thermal bath due to their annihilation with electrons. At the same time, electrons became gradually non-relativistic and therefore stopped contributing to the radiation density. These processes led to an increase in the temperature of the photons, which can be quantified by considering the conservation of the entropy per comoving volume $s$ during that period of time. This law implies that $s \propto g_* T^3$ remained constant, where $g_*$ stands for the effective number of relativistic degrees of freedom of the thermal plasma. Every bosonic helicity contributes to $g_*$ with a unit, whereas every fermionic helicity contributes with a factor of 7/8. As a consequence, the ratio of photon temperatures before and after the positron-electron annihilation satisfies (see Fig. 2.2 )

$$\left( \frac{T_{\text{before}}}{T_{\text{after}}} \right)^3 = \frac{g_{*\text{after}}}{g_{*\text{before}}} = \frac{2}{2 + \frac{7}{8}(2+2)} = \frac{4}{11} \, . \tag{2.20}$$

Consequently, the ratio between the neutrino and the photon temperatures after the electron-positron annihilation is given by

$$\frac{T_\nu^0}{T_\gamma^0} = \left( \frac{4}{11} \right)^{1/3} \, . \tag{2.21}$$

Here the superindex 0 refers to times after the electron-positron annihilation, for example to the recombination era, when the CMB was formed. In Fig. 2.2 we sketch the processes that the radiation of the universe underwent when the neutrinos decoupled from the photons and when the electron-positron pairs annihilated.

Ever since the electron-positron annihilation, only photons and neutrinos have contributed to the radiation density $\rho_R^0$ of the universe, that is, $\rho_R^0 = \rho_\gamma^0 + \rho_\nu^0$. Since any radiation density is
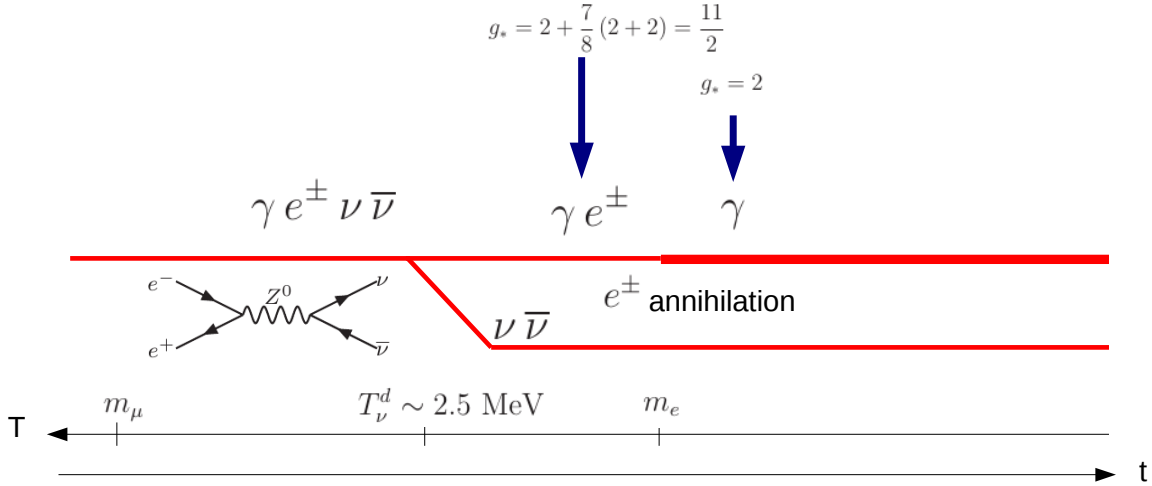
Figure 2.2: Sketch of the processes that the radiation of the universe underwent when the neutrinos went out of equilibrium with the photons and when the electron-positron pairs annihilated. The red line represents the *relative* temperature of the different fluids. The thicker the line, the higher the relative temperature. At first electrons, positrons, photons and neutrinos were in equilibrium. Subsequently weak interactions stopped being efficient and neutrinos decoupled. Afterwards, the electron-positron pairs annihilate, heating the photons with respect to the neutrinos.

proportional to the temperature to the fourth power and to the effective number of relativistic degrees of freedom, the total radiation density is given by

$$\rho_R^0 = \rho_\gamma^0 \left( 1 + \frac{7}{8} \left( \frac{4}{11} \right)^{4/3} N_{\text{eff}} \right) , \tag{2.22}$$

where the first term on the right hand side is the contribution of the photons and the second term is the contribution of the neutrinos. Here $N_{\text{eff}}$ is the number of neutrinos species, which we expect to equal 3. Nonetheless, in the Standard Model of Cosmology this is not the case, because neutrinos did not decouple instantaneously. In fact, the neutrino decoupling is not entirely complete by the time of electron-positron annihilation. In spite of that, Eq. (2.22) can be used to define $N_{\text{eff}}$ in terms of the total radiation density and the photon density. If the non-instantaneous neutrino decoupling is accounted for, the predicted value for the effective number of neutrino species is $N_{\text{eff}} = 3.046$ . By performing a detailed analysis of the CMB from Planck data, WMAP9 polarization data and ground-based observations of high-$\ell$ multipoles of the power spectrum, the Planck Collaboration has determined that $N_{\text{eff}} = 3.36^{+0.68}_{-0.64}$ at 95% C.L. [35].

If there exists a particle that contributes to the radiation density of the universe $\rho_R$, the predicted value for $N_{\text{eff}}$ would be different from 3.046. For instance, as mentioned before, a prediction of the models introduced in part III is the existence of (pseudo-)Goldstone bosons. We discuss their contribution to $N_{\text{eff}}$ and explain their phenomenological consequences in chapter 9.

# Part II

# The Inert Doublet Model

# Chapter 3

# Model I : Dark Matter as an Inert Higgs

## 3.1 The Inert Doublet Model (IDM)

The IDM is an extension the Standard Model with a colorless $SU(2)$ doublet $\Psi$ with hypercharge $1/2$. Furthermore, a discrete $Z_2$ symmetry is postulated so that the Standard Model particles are even under this group while the extra scalar $\Psi$ is odd. Because this symmetry forbids a coupling between the SM fermions and $\Psi$, the extra doublet is called inert. The Lagrangian of the model is

$$\mathcal{L}_{\text{IDM}} \supset \mathcal{L}_{\Phi,\Psi} = \mathcal{L}_{\text{Yukawa}} + (D_\mu\Phi)^\dagger(D^\mu\Phi) + (D_\mu\Psi)^\dagger(D^\mu\Psi) - m_1^2\Phi^\dagger\Phi - m_2^2\Psi^\dagger\Psi \quad (3.1)$$
$$-\lambda_1(\Phi^\dagger\Phi)^2 - \lambda_2(\Psi^\dagger\Psi)^2 - \lambda_3(\Phi^\dagger\Phi)(\Psi^\dagger\Psi) - \lambda_4(\Phi^\dagger\Psi)(\Psi^\dagger\Phi) - \frac{1}{2}\left(\lambda_5(\Phi^\dagger\Psi)(\Phi^\dagger\Psi) + \text{h.c.}\right) \,,$$

where $D_\mu$ stands for the covariant derivative and $\Phi$ is Standard Model doublet. We remark that, due to the $Z_2$ symmetry, $\mathcal{L}_{\text{Yukawa}}$ does not depend on the extra scalar and is therefore identical to the Yukawa Lagrangian of the Standard Model. In addition, it is assumed that the $Z_2$ symmetry remains unbroken after the electroweak symmetry breaking and consequently that only the Higgs doublet acquires an expectation value. With these assumptions the doublets can be cast as

$$\Phi = \begin{pmatrix} G^+ \\ \frac{v_h+h+iG^0}{\sqrt{2}} \end{pmatrix} \,, \qquad \Psi = \begin{pmatrix} H^+ \\ \frac{1}{\sqrt{2}}\left(H^0 + iA^0\right) \end{pmatrix} \,, \quad (3.2)$$

where $v_h = \sqrt{-\frac{m_1^2}{\lambda_1}} \approx 246\,\text{GeV}$, $G^0$ and $G^+$ provide the longitudinal components of the of the $Z$ and $W$ bosons through the Brout-Englert-Higgs mechanism and $h$ is the Standard Model Higgs. On the other hand, the inert scalars are two additional charged states $H^\pm$, one CP-neutral state $H^0$ and one CP-odd neutral state $A^0$. Because of the discrete symmetry, the lightest particle described by the inert doublet is stable. If it is neutral, it is also a dark matter candidate.

## 3.2 Gauge Interactions

The term in the Lagrangian (3.1) with the covariant derivatives gives rise to the gauge interactions between the inert scalars. These can be divided in two: cubic and quartic interactions

$$(D_\mu\Psi)^\dagger(D^\mu\Psi) \supset \mathcal{L}_{\text{Gauge},\Psi} = \mathcal{L}_{\text{Cubic}} + \mathcal{L}_{\text{Quartic}} \quad (3.3)$$

| Particle | | | | Feynman Rule |
|---|---|---|---|---|
| 1 | 2 | 3 | 4 | |
| $H^-$ | $H^+$ | $A$ | - | $-ie\,(p_1^{\mu_3} - p_2^{\mu_3})$ |
| $H^0$ | $H^-$ | $W^+$ | - | $\frac{ig}{2}\,(p_1^{\mu_3} - p_2^{\mu_3})$ |
| $A^0$ | $H^-$ | $W^+$ | - | $-\frac{g}{2}\,(p_1^{\mu_3} - p_2^{\mu_3})$ |
| $H^0$ | $A^0$ | $Z$ | - | $-\frac{g}{2c_W}\,(p_1^{\mu_3} - p_2^{\mu_3})$ |
| $H^-$ | $H^+$ | $Z$ | - | $\frac{ig(2c_W^2-1)}{2c_W}\,(p_1^{\mu_3} - p_2^{\mu_3})$ |
| $H^-$ | $H^+$ | $A$ | $A$ | $2ie^2 g_{\mu_3\mu_4}$ |
| $H^-$ | $H^0$ | $A$ | $W^+$ | $\frac{ieg}{2} g_{\mu_3\mu_4}$ |
| $H^-$ | $A^0$ | $A$ | $W^+$ | $-\frac{eg}{2} g_{\mu_3\mu_4}$ |
| $H^0$ | $H^0$ | $W^-$ | $W^+$ | $\frac{ig^2}{2} g_{\mu_3\mu_4}$ |
| $A^0$ | $A^0$ | $W^-$ | $W^+$ | $\frac{ig^2}{2} g_{\mu_3\mu_4}$ |
| $H^-$ | $H^+$ | $W^-$ | $W^+$ | $\frac{ig^2}{2} g_{\mu_3\mu_4}$ |
| $H^-$ | $H^+$ | $A$ | $Z$ | $\frac{ieg(2c_W^2-1)}{c_W} g_{\mu_3\mu_4}$ |
| $H^0$ | $H^-$ | $W^+$ | $Z$ | $-\frac{ie^2}{2c_W} g_{\mu_3\mu_4}$ |
| $A^0$ | $H^-$ | $W^+$ | $Z$ | $\frac{e^2}{2c_W} g_{\mu_3\mu_4}$ |
| $H^0$ | $H^0$ | $Z$ | $Z$ | $\frac{ie^2}{2c_W^2 s_W^2} g_{\mu_3\mu_4}$ |
| $A^0$ | $A^0$ | $Z$ | $Z$ | $\frac{ie^2}{2c_W^2 s_W^2} g_{\mu_3\mu_4}$ |
| $H^-$ | $H^+$ | $Z$ | $Z$ | $\frac{ie^2(2c_W^2-1)^2}{2c_W^2 s_W^2} g_{\mu_3\mu_4}$ |

Table 3.1: Feynman rules for the gauge interactions of the inert particles according to Eqs. (3.4) and (3.8).

**Cubic Gauge Interactions**  In this case the gauge bosons interact with the inert scalars by means of gauge currents

$$\mathcal{L}_{\text{Cubic}} = J_A^\mu A_\mu + J_Z^\mu Z_\mu + \left( J_{W^-}^{\mu\dagger} W_\mu^- + h.c. \right) , \tag{3.4}$$

with

$$J_A^\mu = ie \left( \partial^\mu H^+ H^- - H^+ \partial^\mu H^- \right) \tag{3.5}$$

$$J_Z^\mu = \frac{ig}{2c_W} \left( (-1 + 2c_W^2)(\partial^\mu H^+ H^- - H^+ \partial^\mu H^-) + iA^0 \partial^\mu H^0 - iH^0 \partial^\mu A^0 \right) \tag{3.6}$$

$$J_{W^-}^\mu = -\frac{ig}{2} \left( \partial^\mu H^- (H^0 + iA^0) - H^- \partial^\mu (H^0 + iA^0) \right) \tag{3.7}$$

**Quartic Gauge Interactions**  These are contact interactions between two gauge bosons and two scalars

$$\begin{aligned}
\mathcal{L}_{\text{Quartic}} &= e^2 A_\mu A^\mu H^+ H^- + \frac{eg}{c_W}(1 - 2c_W^2) A_\mu Z^\mu H^+ H^- \\
&+ \frac{g^2}{4c_W^2} Z_\mu Z^\mu \left( \frac{1}{2}(H^{0\,2} + A^{0\,2}) + (1 - 2c_W^2)^2 H^+ H^- \right)
\end{aligned}$$

$$+ \quad \frac{g^2}{2} W_\mu^- W^{+\mu} \left( \frac{1}{2}(H^{0\,2} + A^{0\,2}) + H^+ H^- \right)$$

$$+ \quad \frac{eg}{2c_W} (-s_W Z_\mu + c_W A_\mu) \left( W^{-\mu} H^+ (H^0 - iA^0) + \text{h.c.} \right). \tag{3.8}$$

All the corresponding Feynman rules are listed on Table 3.1

## 3.3 Scalar Interactions and Parameters of the Model

In the Feynman Gauge the scalar potential reads

$$
\begin{aligned}
- \mathcal{L}_{\text{Scalar}} \quad = \quad & \frac{1}{2} \left( M_h^2 h^2 + M_{H^0}^0 H^{0\,2} + M_{A^0}^2 A^{0\,2} \right) + M_{H^+}^2 H^+ H^- \\
& + \quad \frac{\lambda_1}{4} \left( 4v_h h + h^2 + G^{0\,2} + 2G^+ G^- \right) \left( h^2 + G^{0\,2} + 2G^+ G^- \right) \\
& + \quad \lambda_2 \left( \frac{1}{2} A^{0\,2} + \frac{1}{2} H^{0\,2} + H^+ H^- \right)^2 + \lambda_5 (v_h + h) G^0 H^0 A^0 \\
& + \quad \frac{H^0}{2} \left( H^+ G^- \left( (\lambda_4 + \lambda_5)(v_h + h) + i(\lambda_4 - \lambda_5) G^0 \right) \right) + \text{h.c.} \\
& + \quad \frac{A^0}{2} \left( H^+ G^- \left( i(-\lambda_4 + \lambda_5)(v_h + h) + (\lambda_4 + \lambda_5) G^0 \right) \right) + \text{h.c.} \\
& + \quad \frac{H^{0\,2}}{2} \left( \left( \frac{\lambda_3 + \lambda_4 + \lambda_5}{2} \right) \left( 2v_h h + h^2 \right) + \left( \frac{\lambda_3 + \lambda_4 - \lambda_5}{2} \right) G^{0\,2} + \lambda_3 G^+ G^- \right) \\
& + \quad \frac{A^{0\,2}}{2} \left( \left( \frac{\lambda_3 + \lambda_4 - \lambda_5}{2} \right) \left( 2v_h h + h^2 \right) + \left( \frac{\lambda_3 + \lambda_4 + \lambda_5}{2} \right) G^{0\,2} + \lambda_3 G^+ G^- \right) \\
& + \quad \frac{H^+ H^-}{2} \left( \lambda_3 \left( 2v_h h + h^2 + G^{0\,2} \right) + 2(\lambda_3 + \lambda_4) G^+ G^- \right) + \frac{\lambda_5}{2} \left( (H^+ G^-)^2 + \text{h.c.} \right)
\end{aligned}
\tag{3.9}
$$

where

$$M_h^2 = -2m_1^2 \,, \qquad M_{H^+}^2 = m_2^2 + \frac{1}{2}\lambda_3 v_h^2 \,,$$

$$M_{H^0}^2 = m_2^2 + \frac{1}{2}(\lambda_3 + \lambda_4 + \lambda_5)v_h^2 \,, \qquad M_{A^0}^2 = m_2^2 + \frac{1}{2}(\lambda_3 + \lambda_4 - \lambda_5)v_h^2 \,. \tag{3.10}$$

The corresponding Feynman rules are listed on Table 3.2.

The scalar potential is determined by seven independent parameters, which can be the Higgs boson mass $M_h \approx 125\,\text{GeV}$, the vacuum expectation value of the Higgs field, the dark matter mass $M_{H^0}$ and the quartic couplings $\lambda_2, \lambda_3, \lambda_4$ and $\lambda_5$. These parameters are constrained from the requirement of vacuum stability [117, 118]

$$\lambda_1 > 0 \,, \quad \lambda_2 > 0 \,, \quad \lambda_3 > -2(\lambda_1 \lambda_2)^{\frac{1}{2}} \,, \quad \lambda_3 + \lambda_4 - |\lambda_5| > -2(\lambda_1 \lambda_2)^{\frac{1}{2}}. \tag{3.11}$$

Besides, the unitarity of the $S$-matrix for scalar-to-scalar scattering sets upper limits on certain combinations of couplings [119, 120]

$$
\begin{aligned}
\lambda_1 + \lambda_2 \pm \sqrt{(\lambda_1 - \lambda_2)^2 + \lambda_4^2} &< 8\pi, \qquad \lambda_3 \pm \lambda_4 < 8\pi \\
\lambda_1 + \lambda_2 \pm \sqrt{(\lambda_1 - \lambda_2)^2 + \lambda_5^2} &< 8\pi, \qquad \lambda_3 \pm \lambda_5 < 8\pi \\
3(\lambda_1 + \lambda_2) \pm \sqrt{9(\lambda_1 - \lambda_2)^2 + (2\lambda_3 + \lambda_4)^2} &< 8\pi, \qquad \lambda_3 + 2\lambda_4 \pm 3\lambda_5 < 8\pi \,.
\end{aligned}
\tag{3.12}
$$

Lastly, it is common to impose also perturbativity on the parameters of the model. This condition along with the vacuum stability requirement significantly constrain the mass splittings among the exotic particles. Moreover, for a heavy exotic neutral Higgs ($M_{H^0} \gg M_W$) the splitting is relatively small and we expect the particles belonging to the extra doublet to have nearly degenerate masses. This is consistent with the fact that at very high energies electroweak symmetry breaking effects are negligible and that therefore the members of any $SU(2) \times U(1)$ multiplet should have similar masses. Notice that $\lambda_4$ and $\lambda_5$ determine the mass splittings between the different inert scalars at tree level. Nevertheless, loops of SM gauge bosons between the neutral and charged components also give rise to a mass splitting. This effect has been calculated in [66] and is equal to

$$(M_{H^+} - M_{H^0})_{\text{Quantum}} = \frac{\alpha M_Z}{2} \approx 0.36 \,\text{GeV} \,. \tag{3.13}$$

The scalar potential is indeed $Z_2$ symmetric. Moreover, by performing $(H^0, A^0, H^+) \rightarrow (-A^0, H^0, iH^+)$ and $\lambda_5 \rightarrow -\lambda_5$ the potential remains invariant. This shows that $H^0$ and $A^0$ can be interchanged. We will then assume in what follows, and without loss of generality, that $H^0$ is the dark matter candidate. Due to its similarity to the Standard Model scalar, $H^0$ is usually called inert Higgs dark matter.

## 3.4 Inert Higgs Abundance

The inert scalars interact with the particles of the Standard Model by virtue of the electroweak interactions and via the scalar potential. The inert Higgs $H^0$ is thus a WIMP, which presumably was in thermal equilibrium with ordinary matter in the early universe until the moment in which its interaction rate became so small that its abundance remained fixed (see section 2.2). The thermal production has been studied extensively in the literature for the IDM (see *e.g.* [8, 9, 15, 121, 122]). In particular, it has been found that co-annihilations play a significant role in dark matter production, specially for masses above the electroweak scale. Accordingly, to calculate the relic abundance -as discussed in section 2.2- the following Boltzmann equation must be solved

$$\frac{dn}{dt} + 3Hn = -\langle \sigma_{\text{eff}} v \rangle \left( n^2 - (n^{eq})^2 \right) \qquad \text{where} \qquad n = n_{H^0} + n_{A^0} + n_{H^+} + n_{H^-} \,, \tag{3.14}$$

with equilibrium densities given by

$$n_i^{eq} = \frac{M_i^2 T}{\pi^2} K_2 \left( \frac{M_\pm}{T} \right) \,. \tag{3.15}$$

| Particle | | | | Feynman Rule |
|:---:|:---:|:---:|:---:|:---:|
| 1 | 2 | 3 | 4 | |
| $h$ | $H^0$ | $H^0$ | - | $-iv_h\left(\lambda_3 + \lambda_4 + \lambda_5\right)$ |
| $h$ | $A^0$ | $A^0$ | - | $-iv_h\left(\lambda_3 + \lambda_4 - \lambda_5\right)$ |
| $h$ | $H^+$ | $H^-$ | - | $-iv_h\lambda_3$ |
| $G^-$ | $H^0$ | $H^+$ | - | $-\frac{1}{2}iv_h\left(\lambda_4 + \lambda_5\right)$ |
| $G^-$ | $A^0$ | $H^+$ | - | $\frac{1}{2}v_h\left(\lambda_5 - \lambda_4\right)$ |
| $G^0$ | $H^0$ | $A^0$ | - | $-iv_h\lambda_5$ |
| $H^0$ | $H^0$ | $H^0$ | $H^0$ | $-6i\lambda_2$ |
| $H^0$ | $H^0$ | $A^0$ | $A^0$ | $-2i\lambda_2$ |
| $A^0$ | $A^0$ | $A^0$ | $A^0$ | $-6i\lambda_2$ |
| $H^0$ | $H^0$ | $H^+$ | $H^-$ | $-2i\lambda_2$ |
| $A^0$ | $A^0$ | $H^+$ | $H^-$ | $-2i\lambda_2$ |
| $H^+$ | $H^+$ | $H^-$ | $H^-$ | $-4i\lambda_2$ |
| $G^0$ | $G^0$ | $H^0$ | $H^0$ | $-i\left(\lambda_3 + \lambda_4 - \lambda_5\right)$ |
| $G^+$ | $G^-$ | $H^0$ | $H^0$ | $-i\lambda_3$ |
| $h$ | $h$ | $H^0$ | $H^0$ | $-i\left(\lambda_3 + \lambda_4 + \lambda_5\right)$ |
| $G^0$ | $G^0$ | $A^0$ | $A^0$ | $-i\left(\lambda_3 + \lambda_4 + \lambda_5\right)$ |
| $G^+$ | $G^-$ | $A^0$ | $A^0$ | $-i\lambda_3$ |
| $h$ | $h$ | $A^0$ | $A^0$ | $-i\left(\lambda_3 + \lambda_4 - \lambda_5\right)$ |
| $G^0$ | $G^0$ | $H^+$ | $H^-$ | $-i\lambda_3$ |
| $G^+$ | $G^-$ | $H^+$ | $H^-$ | $-i\left(\lambda_3 + \lambda_4\right)$ |
| $h$ | $h$ | $H^+$ | $H^-$ | $-i\lambda_3$ |
| $G^0$ | $G^-$ | $H^0$ | $H^+$ | $\frac{1}{2}\left(\lambda_4 - \lambda_5\right)$ |
| $G^-$ | $h$ | $H^0$ | $H^+$ | $-\frac{1}{2}i\left(\lambda_4 + \lambda_5\right)$ |
| $G^0$ | $G^-$ | $A^0$ | $H^+$ | $-\frac{1}{2}i\left(\lambda_4 + \lambda_5\right)$ |
| $G^-$ | $h$ | $A^0$ | $H^+$ | $\frac{1}{2}\left(\lambda_5 - \lambda_4\right)$ |
| $G^0$ | $h$ | $H^0$ | $A^0$ | $-i\lambda_5$ |
| $G^-$ | $G^-$ | $H^+$ | $H^+$ | $-2i\lambda_5$ |
| $G^+$ | $G^+$ | $H^-$ | $H^-$ | $-2i\lambda_5$ |

Table 3.2: Feyman rules for the scalar interactions of the inert particles according to Eq. (3.9).

The effective thermal cross section is given by [78]

$$\langle \sigma_{\text{eff}} v \rangle \;\; = \;\; \sum_{i,j=\pm} \langle \sigma^{ij} v \rangle \frac{n_i^{eq}}{n^{eq}} \frac{n_j^{eq}}{n^{eq}}, \tag{3.16}$$

with

$$\langle \sigma^{ij} v \rangle = \frac{\int_{(M_i+M_j)^2}^{\infty} \frac{ds}{\sqrt{s}} K_1\left(\frac{\sqrt{s}}{T}\right)(s-(M_i+M_j)^2)(s-(M_i-M_j)^2)\sigma(ij \to all)}{8T M_i^2 M_j^2 K_2(\frac{M_i}{T}) K_2(\frac{M_j}{T})} \,. \tag{3.17}$$

The observed abundance $\Omega h^2 = 0.1199 \pm 0.0027$ [123] in the IDM can be reproduced in three dark matter mass ranges:

- **Low-mass regime**. For masses in the GeV range below the $W$ boson mass, dark matter annihilates mostly into light fermions with a rate controlled by the size of the quartic couplings in order to match the observed abundance of dark matter. In this regime, three body annihilations of the type $H^0 H^0 \to WW^* \to W f \bar{f}'$ are also important in some regions of the parameter space [14].

- **Intermediate regime**. When the dark matter mass is above $M_W$ and below 535 GeV, the annihilations into weak gauge bosons is so efficient that the dark matter relic density is smaller than the observed abundance. There is an exception to this for dark matter masses in between $M_W \lesssim M_{H^0} \lesssim 150\,\text{GeV}$, if some annihilation diagrams are chosen so that they can cancel each other out, allowing for a relic density in agreement with observations. Nevertheless, this region has been ruled out by the XENON100 experiment [15, 124].

- **High-Mass Regime**. When $M_{H^0} \sim 535\,\text{GeV}$ and the quartic couplings vanish, the annihilation rate into gauge bosons is small enough to match the observed value of the relic density. It turns out that the effect of non-zero quartic couplings is to increase the annihilation cross section. Consequently for masses $M_{H^0} \gtrsim 535\,\text{GeV}$, the observed abundance of dark matter can also be obtained for an appropriated choice of the quartic couplings. As a consequence of this, the larger the dark matter mass, the larger the quartic couplings. Likewise, the upper limit on the dark matter is set by the perturbativity constraint, which is around 58 TeV for quartic couplings of order $4\pi$. In this work we do not consider quartic couplings so large, in fact we consider only $\lambda_i \lesssim 2$, for which $M \lesssim 6$ TeV.

In order to illustrate the dark matter production, we perform a scan over the five dimensional parameter space. For every point we require perturbativity and unitarity, by demanding that the quartic couplings satisfy Eqs. (3.11) and (3.13). For each of the points we then solve numerically the Boltzmann equation Eq. (3.14) by using micrOMEGAs 3.1 [79], working under an implementation of our model made with FeynRules [125], and select only those points for which the computed relic density is in agreement within $3\sigma$ with the observed value $\Omega_{\text{DM}} h^2 = 0.1199 \pm 0.0027$. In Fig. 3.1 we show the relic abundance obtained from the scan. The orange points correspond
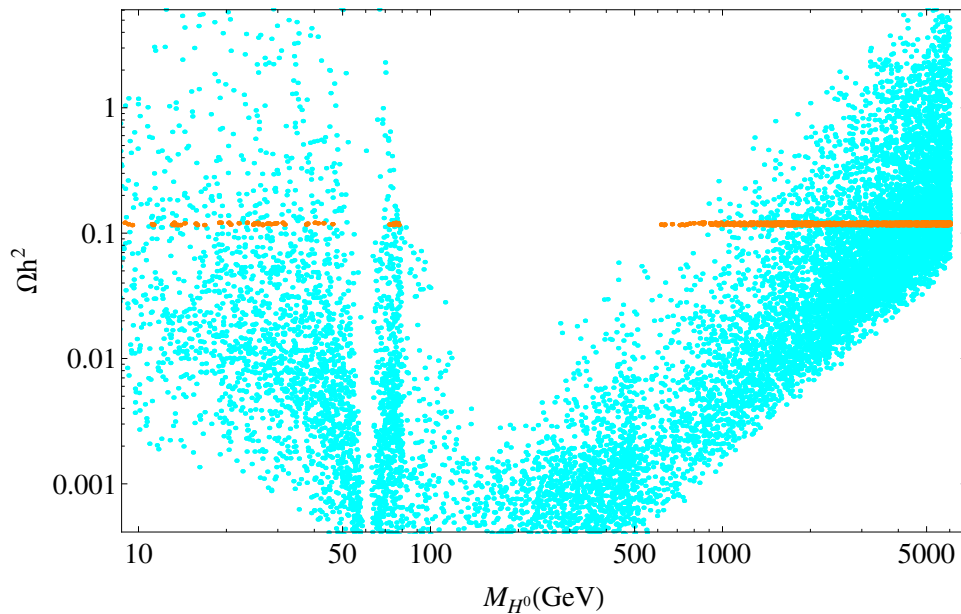
Figure 3.1: Relic abundance obtained from scanning the parameter space of the IDM. The orange points correspond to those choices that correctly reproduce the cold dark matter relic abundance.

to those choices that correctly reproduce the cold dark matter relic abundance. In this plot we can clearly see the low-mass and the high-mass regime. We do not tune any parameter of the model and as a result in the scan we do not find the intermediate regime.

Dark matter direct and indirect detection experiments as well as collider searches have severely constrained the IDM in the low-mass regime. Although some regions are still allowed, they either rely on coannihilation or on resonant effects [17]. We take this as motivation to study the high-mass regime and in this work we only consider that part of the parameter space.

# Chapter 4

# Gamma-Rays from Dark Matter Annihilations in the IDM

In the high-mass regime of the IDM, dark matter annihilations can produce gamma-rays in three different ways. On first place, when the gauge and Higgs bosons produced in annihilations decay and fragment. Secondly, from the VIB process $H^0 H^0 \to W^+ W^- \gamma$. And lastly, from the one-loop processes $H^0 H^0 \to \gamma\gamma$ and $H^0 H^0 \to \gamma Z$ [1]. In this chapter, we study $H^0 H^0 \to \gamma\gamma$ and VIB at the perturbative level. As we will see, non-perturbative effects must be included in order to satisfy the requirements from unitarity. These effects will be studied in chapter 5. After that, we will see that including the process $H^0 H^0 \to \gamma Z$ in the analysis is straightforward.

## 4.1 One-loop Annihilation of Inert Scalars into Photons

The invariant amplitude for the process $H^0 H^0 \to \gamma\gamma$ can be cast as

$$\mathcal{M} = \mathcal{M}^{\alpha_3 \alpha_4} \epsilon_{\alpha_3}(p_3) \epsilon_{\alpha_4}(p_4) \,, \qquad (4.1)$$
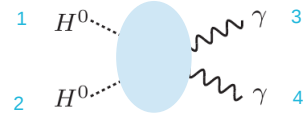


where $\epsilon$ stands for the photon polarization vectors and the subscripts 3 and 4 refer to the final state photons, as shown in the figure. As is well known, electromagnetic gauge invariance severely constrains this amplitude. In fact, $\mathcal{M}^{\alpha_3 \alpha_4}$ must satisfy the Ward Identities

$$p_{3\alpha_3} \mathcal{M}^{\alpha_3 \alpha_4} = p_{4\alpha_4} \mathcal{M}^{\alpha_3 \alpha_4} = 0. \qquad (4.2)$$

In the $s$-wave annihilation limit, both particles of the initial state have the same momentum $(p_3 + p_4)/2$ and therefore the tensor $\mathcal{M}^{\alpha_3 \alpha_4}$ depends only on $p_3$ and $p_4$. Using this fact, the transformations properties of $\mathcal{M}^{\alpha_3 \alpha_4}$ under Lorentz transformations and the Ward identities in

---

[1]The corresponding study for the low-mass regime of the IDM was done in [10]
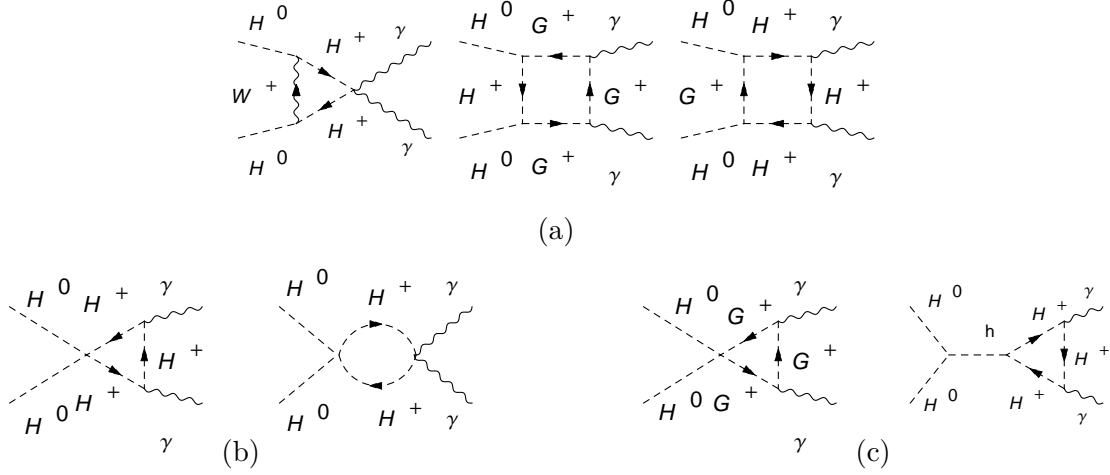
Figure 4.1: Examples of diagrams contributing to (a) $A_0$, (b) $A_2$ and (c) $A_3$.

Eq. (4.2), it is possible to prove that $\mathcal{M}^{\alpha_3\alpha_4}$ must take the form

$$\mathcal{M}^{\alpha_3\alpha_4}\Big|_{s-wave} = A\left(g^{\alpha_3\alpha_4} - \frac{p_4^{\alpha_3}p_3^{\alpha_4}}{2M_{H^0}^2}\right),\tag{4.3}$$

where $A$ is a complex scalar function of the dark matter mass and the quartic couplings. With a FeynRules [126] implementation of the IDM for FeynArts [127], we calculated the annihilation amplitude (4.1) in the Feynman gauge. In total there are one hundred and forty diagrams contributing to it, we only show a subset of them in Fig. 4.1. We found that s-wave piece effectively takes the form indicated in Eq. (4.3). Furthermore we deduced an analytical formula for $A$.

A careful look of the one-loop Feynman diagrams reveals that the only inert scalars in the loop propagators are $H^0$ and $H^+$. Furthermore, as explicit couplings in the diagrams $\lambda_4$ and $\lambda_5$ appear only in the combination $\lambda_4 + \lambda_5$, which equals $2\left(M_{H^0}^2 - M_{H^+}^2\right)/v_h^2$ if we neglect the quantum effects of Eq. (3.13). As a result the dependence on these quartic couplings can be written in terms of $M_{H^0}$ and $M_{H^+}$. A further look shows that the dependence on the other quartic couplings $\lambda_2$ and $\lambda_3$ can be separated explicitly. As a result we find convenient to write $A$ as

$$A = A_0(M_{H^0}, M_{H^+}) + A_2(M_{H^0}, M_{H^+}, \lambda_2) + A_3(M_{H^0}, M_{H^+}, \lambda_3).\tag{4.4}$$

Since the quartic couplings do not change under gauge transformations, the functions $A_0$, $A_2$ and $A_3$ are gauge-invariant and therefore physically meaningful. In Fig. 4.2 we plot their absolute values as a function of the dark matter mass, for different choices of the quartic couplings and the mass splitting between the charged scalar and the dark matter mass. From the plots is clear that $A_0$ dominates over $A_2$ and $A_3$, specially for heavy dark matter masses. This implies that the dependence on $\lambda_2$ and $\lambda_3$ of the annihilation amplitude is subdominant.
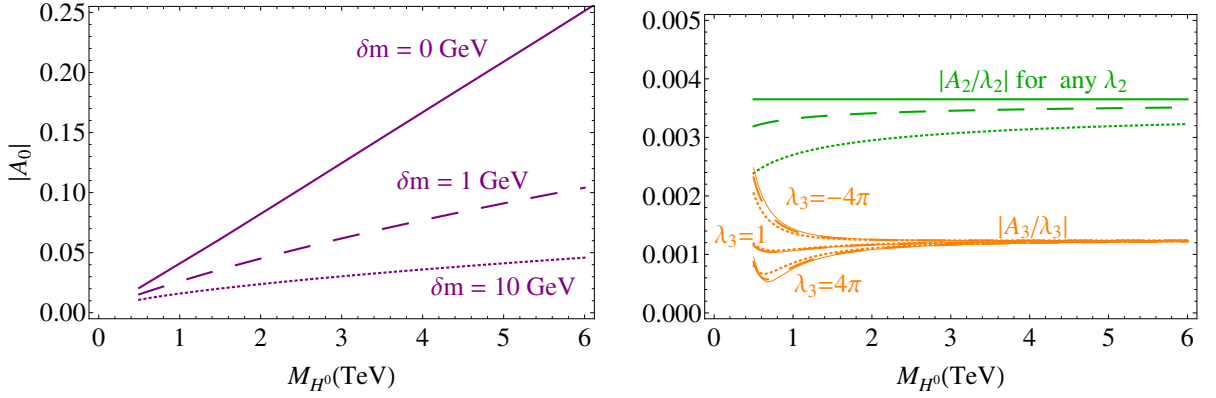
Figure 4.2: Absolute value of the functions $A_0$, $A_1$ and $A_2$ introduced in Eq. (4.4) for different quartic couplings combinations. Here $\delta m = M_{H^+} - M_{H^0}$. For the continuous lines $\delta m = 0$ GeV, for the dashed lines $\delta m = 1$ GeV and for the dotted lines $\delta m = 10$ GeV.

As a function of $A$, the cross section for dark matter annihilation into photons is given by the expression

$$\sigma v \left( H^0 H^0 \to \gamma\gamma \right) \Big|_{s-wave} = \frac{|A|^2}{32\pi M_{H^0}^2}. \qquad (4.5)$$

In order to study the dependence with the mass, we plot $\sigma v \left( H^0 H^0 \to \gamma\gamma \right)\big|_{s-wave}$ in the left panel of Fig. 4.3 for three mass splittings, namely $\delta m = M_{H^+} - M_{H^0} = 0, 1$ and $10$ GeV in continuous, dashed and dotted lines, respectively. In addition, we show the effect of the quartic couplings by plotting the annihilation cross section when $\lambda_2 = \lambda_3 = 0$ in black, when $\lambda_2 = 2, \lambda_3 = 0$ in pink and finally when $\lambda_2 = 0, \lambda_3 = 2$ in magenta. We can see that the cross sections depend mildly on the quartic couplings $\lambda_2$ and $\lambda_3$ , and depend strongly on the quartic coupling combination $\lambda_4 + \lambda_5$, as expected from Fig. 4.2, because this combination determines the mass splitting $\delta m$.

When all the quartic couplings vanish, the cross section is a constant function of the dark matter mass. This behavior can be traced back to the fact that for TeV dark matter $A_0 \propto M_{H^0}/M_W$, as shown in Fig. 4.2. Partial-wave unitarity [128] sets an upper bound on the total s-wave cross section

$$\sigma v|_{s-wave} \lesssim \frac{4\pi}{M_{H^0}^2 v} \approx \frac{1}{v}\left(\frac{1\,\mathrm{TeV}}{M_{H^0}}\right)^2 1.47 \times 10^{-22} \mathrm{cm}^3/\mathrm{s} \ . \qquad (4.6)$$

Therefore, we are forced to conclude that the *one-loop* cross section exceeds the upper bound set by unitarity for extremely large masses. This violation of perturbative unitarity does not appear when relativistic velocities are considered. This is shown in the right panel of Fig. 4.3, where it is possible to see that for heavy dark matter with large velocities the cross section goes like $\sim 1/M_{H^0}^2$ as opposed to the non-relativistic case.
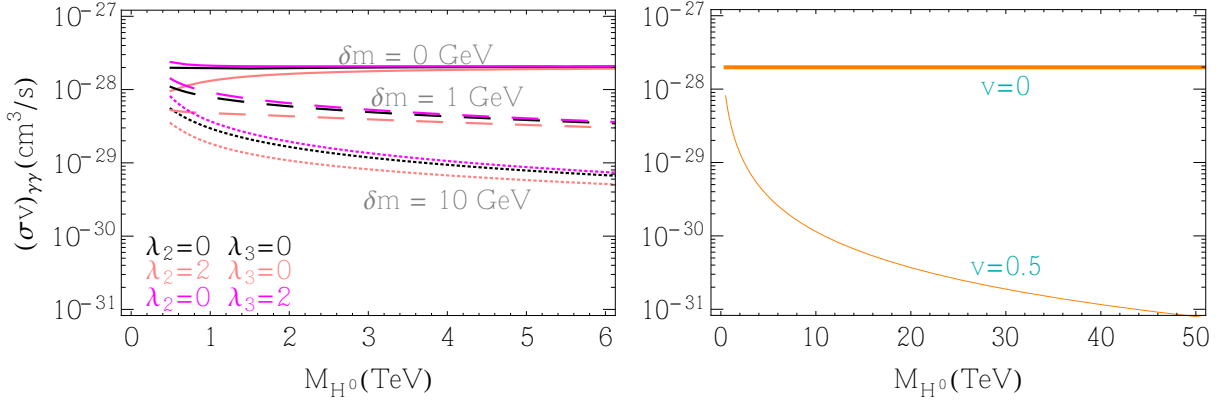
Figure 4.3: *Left plot:* s-wave cross sections for the one-loop processes $H^0 H^0 \to \gamma\gamma$ for three mass splittings, namely $\delta m = M_{H^+} - M_{H^0} = 0, 1$ and 10 GeV in continuous, dashed and dotted lines respectively. In addition we show the effect of the quartic couplings $\lambda_2$ and $\lambda_3$ in different colors. *Right plot:* One-loop cross sections for different dark matter relative velocities when $\delta m = 0$. Notice that only for $v = 0$ the cross section is a constant. In the other case, the cross section goes like $\sim 1/M_{H^0}^2$, as expected from unitarity arguments. Notice that horizontal scale is different on each plot.

Similar difficulties have been found for neutralino dark matter in the context of the MSSM [96]. In this scenario, one-loop annihilation cross sections into photons are not suppressed by the dark matter mass but rather by the W boson mass. It has been shown [22] that this anomalous behavior is alleviated when higher-order effects are included. The same problem arises in IDM. The origin of the problem and its solution will be studied in chapter 5.

## 4.2 Virtual Internal Bremsstrahlung (VIB)

### The Invariant Amplitude

The annihilation process into $W$ bosons with the associated emission of a photon, $H^0 H^0 \to W^+ W^- \gamma$, is described in the unitary gauge by the fourteen diagrams shown in Fig. 4.4. In general, the invariant amplitude for this process can be cast as

$$\mathcal{M} = \mathcal{M}_{\alpha_3 \alpha_4 \alpha_5} \epsilon^{\alpha_3}(p_3) \epsilon^{\alpha_4}(p_4) \epsilon^{\alpha_5}(p_5) \,, \quad (4.7)$$
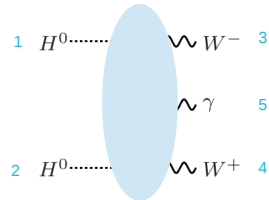
where $\epsilon$ stands for the spin-1 polarization vectors and $p_3$, $p_4$ and $p_5$ are the momenta of the $W^+$, $W^-$ and the photon respectively, as shown in the figure. If $p_1$ and $p_2$ are the momenta of the annihilating dark matter particles in the CM frame, their s-wave limit is given by $p_1 = p_2 = P = (M_{H^0}, 0, 0, 0)$. In terms of these variables, the s-wave amplitude can be cast as

$$
\begin{aligned}
\mathcal{M}_{\alpha_3\alpha_4\alpha_5}\Big|_{s-wave} &= \frac{g^2 e}{2}\Bigg[ -\frac{(p_3 + p_5)_{\alpha_4}(p_3 - p_4)_{\alpha_5}(p_4 + p_5)_{\alpha_3}}{((P - p_3)^2 - M_{H^+}^2)((P - p_4)^2 - M_{H^+}^2)} \\
&+ \frac{(p_{4\alpha_5}p_{3\alpha_4} - p_{5\alpha_4}p_{3\alpha_5} + p_5 \cdot (p_3 + p_4)g_{\alpha_5\alpha_4})\,(p_4 + p_5)_{\alpha_3}}{p_4 \cdot p_5((P - p_3)^2 - M_{H^+}^2)} \\
&- \frac{(p_{3\alpha_5}p_{4\alpha_3} - p_{5\alpha_3}p_{4\alpha_5} + p_5 \cdot (p_3 + p_4)g_{\alpha_5\alpha_3})\,(p_3 + p_5)_{\alpha_4}}{p_3 \cdot p_5((P - p_4)^2 - M_{H^+}^2)} \\
&+ \frac{p_{5\alpha_3}g_{\alpha_5\alpha_4} + p_{4\alpha_5}g_{\alpha_3\alpha_4} - p_{5\alpha_4}g_{\alpha_3\alpha_5}}{p_4 \cdot p_5} - \frac{p_{5\alpha_4}g_{\alpha_5\alpha_3} + p_{3\alpha_5}g_{\alpha_3\alpha_4} - p_{5\alpha_3}g_{\alpha_4\alpha_5}}{p_3 \cdot p_5}\Bigg] \\
&+ \frac{g(\lambda_3 + \lambda_4 + \lambda_5)\,e M_W v_h p_5^\lambda}{(4M_{H^0}^2 - M_h^2)p_5 \cdot p_3\ p_5 \cdot p_4}\big[(p_{5\alpha_3}\,g_{\alpha_4\alpha_5} - p_{5\alpha_4}\,g_{\alpha_3\alpha_5})\,(p_3 + p_4)_\lambda \\
&- (p_{3\alpha_5}\,p_{4\lambda} - p_{4\alpha_5}\,p_{3\lambda})\,g_{\alpha_3\alpha_4}\big].
\end{aligned}
\tag{4.8}
$$

As is well known, electromagnetic gauge invariance severely constrains this amplitude. In fact, the previous expression for $\mathcal{M}^{\alpha_3\alpha_4\alpha_5}$ satisfies the Ward Identities

$$
p_{5\alpha_5}\mathcal{M}^{\alpha_3\alpha_4\alpha_5} = 0.
\tag{4.9}
$$

In order to exploit gauge invariance, we can write the scattering amplitude only as a function of $M_{H^0}$, $\lambda_3$, $\lambda_4$ and $\lambda_5$ using Eq. (3.10), if we neglect the quantum effects of Eq. (3.13). Furthermore, we notice that $\mathcal{M}$ depends on $\lambda_4$ and $\lambda_5$ only through the combination $\lambda_4 + \lambda_5$. Now, since gauge transformations do not transform the quartic couplings, $\mathcal{M}$ can be separated in two gauge-invariant pieces

$$
\mathcal{M}(M_{H^0}, \lambda_3, \lambda_4 + \lambda_5) = \mathcal{M}_{\text{Gauge}}(M_{H^0}) + \mathcal{M}_{\text{Quartic}}(M_{H^0}, \lambda_3, \lambda_4 + \lambda_5),
\tag{4.10}
$$

where the first term is the scattering amplitude when the quartic couplings are set to zero. Accordingly, the squared amplitude can be cast as

$$
|\mathcal{M}|^2 = |\mathcal{M}_{\text{Gauge}}|^2 + |\mathcal{M}_{\text{Quartic}}|^2 + 2Re\left(\mathcal{M}_{\text{Gauge}}\mathcal{M}_{\text{Quartic}}^\dagger\right).
\tag{4.11}
$$

The expression for $|\mathcal{M}|^2$ is very complicated in general. However, in the limit of zero dark matter velocity, we find that

$$
|\mathcal{M}(M_{H^0}, \lambda_3, \lambda_4 + \lambda_5)|^2\Big|_{v\to 0} = |\mathcal{M}(M_{H^0}, \lambda_3, 0)|^2\Big|_{v\to 0} + \mathcal{O}\left(\frac{M_W^2}{M_{H^0}^2}(\lambda_4 + \lambda_5)\right),
\tag{4.12}
$$

since in the high-mass regime of the IDM $M_W \ll M_{H^0}$, the dependence on $\lambda_4 + \lambda_5$ is subdominant. As a result, it is a good approximation to neglect $\lambda_4 + \lambda_5$, especially for dark matter masses much heavier than the $W$ mass. Interestingly, this effect can be understood in the Feynman
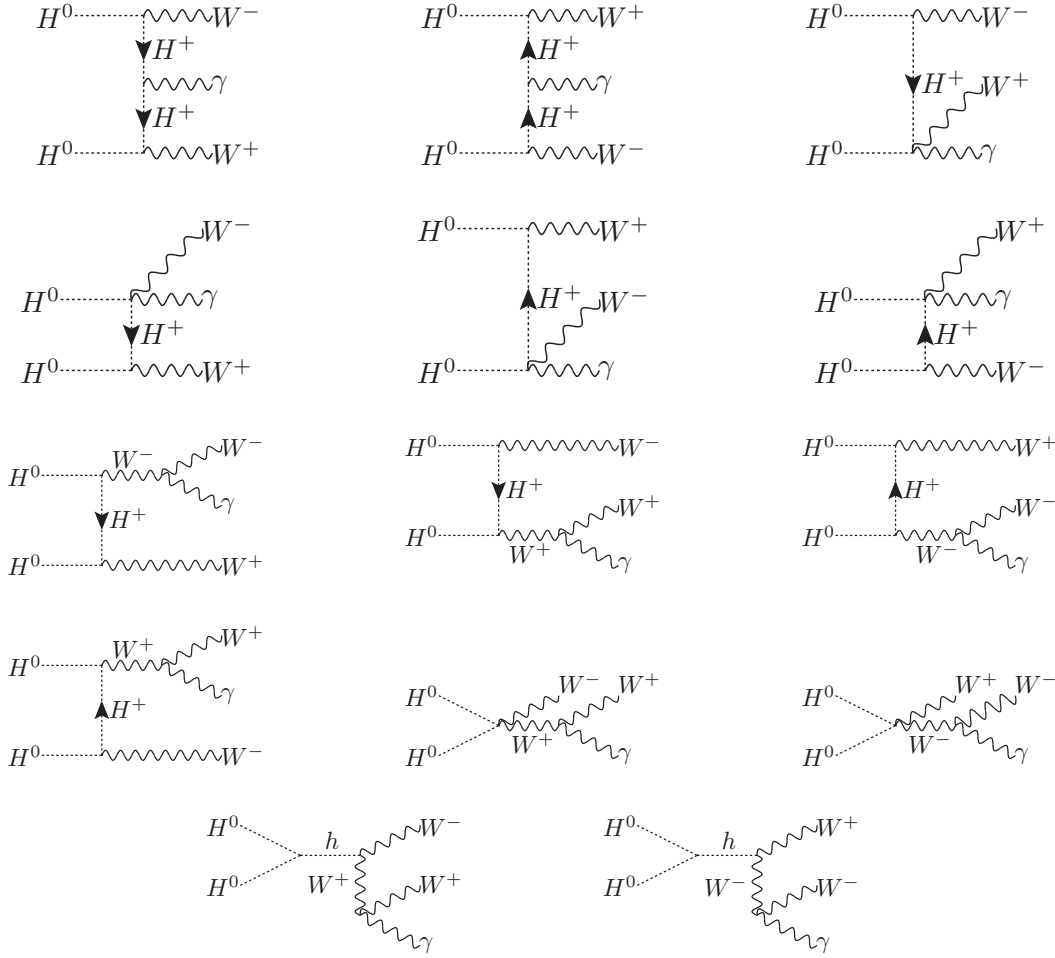
Figure 4.4: Feynman diagrams contributing to the annihilation process $H^0 H^0 \to W^+ W^- \gamma$ in the unitary gauge.

gauge from the Goldstone boson equivalence theorem [129, 130]. In the TeV scale the longitudinal components of the $W^\pm$ bosons are equivalent to the Goldstone bosons $G^\pm$. Furthermore, in that regime the vev $v_h$ can be neglected so that cubic interactions are effectively negligible and the dark matter annihilations into a pair of longitudinal $W$ bosons - or equivalently into a pair $G^+ G^-$ - can only take place via the quartic coupling $\lambda_3$ (see Table 3.2). The further emission of a photon in order to complete the final state $W^+ W^- \gamma$ does not alter this picture. This shows why the only quartic coupling on which the VIB spectrum strongly depends is $\lambda_3$ and why the dependence on $\lambda_4 + \lambda_5$ becomes more and more subdominant for higher masses.

Under the approximation $\lambda_4 + \lambda_5 \approx 0$ and dropping the label $v \to 0$, we find

$$|\mathcal{M}_{\text{Gauge}}|^2 = \frac{e^2 g^4}{2 M_{H^0}^2 (x_+ - 1)^2 (x + x_+ - 1)^2 (x_+ - 2\mu)^2 (2\mu + x + x_+ - 2)^2}$$

$$
\begin{aligned}
\Bigg[ & x^6\Big(-\mu + x_+ - 1\Big) + x^5\Big(3x_+^2 + (2\mu-9)x_+ - 4\mu^2 + 6\Big) + x^4\Big(5x_+^3 - (\mu+20)x_+^2 \\
& + 2(7\mu^2 - 6\mu + 15)x_+ - 10\mu^3 - 6\mu^2 + 11\mu - 15\Big) + x^3\Big(5x_+^4 - (6\mu+25)x_+^3 \\
& + 2(3\mu^2 + 6\mu + 25)x_+^2 + (40\mu^3 - 66\mu^2 + 20\mu - 50)x_+ - 4(6\mu^4 + 3\mu^3 - 12\mu^2 + 6\mu - 5)\Big) \\
& + x^2\Big(3x_+^5 - (3\mu+20)x_+^4 + \big(-16\mu^2 + 28\mu + 50\big)x_+^3 + (40\mu^3 + 2\mu^2 - 44\mu - 65)x_+^2 \\
& + 2(12\mu^4 - 72\mu^3 + 49\mu^2 - 2\mu + 24)x_+ - 16 - 24\mu^5 + 16\mu^4 + 78\mu^3 - 76\mu^2 + 22\mu\Big) \\
& + x(x_+ - 1)\Big(x_+^5 - 8x_+^4 + (-8\mu^2 + 8\mu + 22)x_+^3 + 4(10\mu^2 - 8\mu - 7)x_+^2 \\
& + (24\mu^4 - 64\mu^3 - 2\mu^2 + 20\mu + 20)x_+ - 4(12\mu^4 - 26\mu^3 + 14\mu^2 - 3\mu + 2)\Big) \\
& - (x_+ - 1)^2\Big(x_+^4 - 4x_+^3 + (-8\mu^2 + 4\mu + 6)x_+^2 + 4(4\mu^2 - 2\mu - 1)x_+ \\
& + 24\mu^4 - 40\mu^3 + 18\mu^2 - 4\mu + 2\Big)\Bigg],
\end{aligned}
\tag{4.13}
$$

$$
\begin{aligned}
|\mathcal{M}_{\text{Quartic}}|^2 = {} & \frac{e^2\lambda_3^2}{M_{H^0}^2(x_+ - 1)^2(x + x_+ - 1)^2(1 - \mu_h)^2} \\
& \Bigg[2\mu x^4 + 4\mu x^3(x_+ - 1) + x^2(4\mu x_+^2 + 12\mu^2 x_+ - 12\mu x_+ + x_+ - 12\mu^3 - 8\mu^2 + 7\mu - 1) \\
& + x(12\mu^2 - 4\mu + 1)(x_+^2 - 3x_+ + 2) - (12\mu^2 - 4\mu + 1)(x_+ - 1)^2\Bigg],
\end{aligned}
\tag{4.14}
$$

$$
\begin{aligned}
2Re\left(\mathcal{M}_{\text{Gauge}}\mathcal{M}_{\text{Quartic}}^\dagger\right) = {} & \frac{2e^2 g^2 \mu \lambda_3}{M_{H^0}^2(x_+ - 1)^2(x + x_+ - 1)^2(1 - \mu_h)(x_+ - 2\mu)(2\mu + x + x_+ - 2)} \\
& \Bigg[x^4(1 - x_+) + x^3\Big(x_+^2 + (3 - 12\mu)x_+ + 6\mu^2 + 9\mu - 4\Big) + x^2\Big(4x_+^3 - 3(4\mu + 3)x_+^2 \\
& - 6\mu(2\mu - 7)x_+ + 12\mu^3 - 27\mu + 5\Big) + x(x_+ - 1)\Big(2x_+^3 - 10x_+^2 + 2(-6\mu^2 + 9\mu + 4)x_+ \\
& + 24\mu^2 - 30\mu + 3\Big) - (x_+ - 1)^2\Big(-12\mu^2 + 12\mu + 2x_+^2 - 4x_+ - 1\Big)\Bigg],
\end{aligned}
\tag{4.15}
$$

where $\mu_h = \frac{M_h^2}{s} = \frac{M_h^2}{4M_{H^0}^2}$ and $\mu = \frac{M_W^2}{4M_{H^0}^2}$. Notice that the interference term is proportional to $\mu$ and it is therefore subdominant.

**The Cross Section**

The differential cross section for the process $H^0 H^0 \to W^+ W^- \gamma$ can be written as

$$
d\sigma \;=\; \frac{1}{(2\pi)^5 J}|\mathcal{M}|^2 d_3(PS),
\tag{4.16}
$$

where $\mathcal{M}$ is the scattering amplitude, $J$ the initial flux and $d_3(PS)$ the three-body phase-space factor. These are defined by

$$J \quad = \quad 4E_1 E_2 v, \qquad \text{where } v = \left| \frac{\vec{p_1}}{E_1} - \frac{\vec{p_2}}{E_2} \right|, \tag{4.17}$$

$$d_3(PS) \quad = \quad \delta^4(p_1 + p_2 - p_3 - p_4 - p_5) \frac{d^3 p_3}{2E_3} \frac{d^3 p_4}{2E_4} \frac{d^3 p_5}{2E_5}. \tag{4.18}$$

Here the labeling of the momenta is self-explanatory. We are interested in the limit of zero dark matter velocity, for which $E_1, E_2 \to M_{H^0}$ in the CM frame. Besides, the three-body phase-space factor after integration of the delta function can be written as

$$d_3(PS) \quad = \quad \pi^2 M_{H^0}^2 dx_+ dx, \qquad \text{where} \qquad x_+ = \frac{E_4}{M_H^0} \text{ and } x = \frac{E_5}{M_H^0}. \tag{4.19}$$

The ranges for $x_+$ and $x$ are determined by the energy range of the photon and the $W^+$ and are given by

$$0 < x < 1 - 4\mu \qquad \text{and} \qquad x_+ \lesseqgtr \frac{1}{2} \left( 2 - x \pm x \sqrt{1 - \frac{4\mu}{1 - x}} \right). \tag{4.20}$$

As a result we have

$$\left. \frac{d(\sigma v)}{dx} \right|_{v \to 0} = \frac{1}{128\pi^3} \int_{x_{+\min}}^{x_{+\max}} |\mathcal{M}|^2 \Big|_{v \to 0} dx_+. \tag{4.21}$$

Using the previous expressions for the invariant amplitude square, the total differential velocity weighted annihilation cross section can be cast as

$$\frac{d(\sigma v)_{W^+ W^- \gamma}}{dx} = \left. \frac{d(\sigma v)}{dx} \right|_{\text{Gauge}} + \left. \frac{d(\sigma v)}{dx} \right|_{\text{Quartic}} + \left. \frac{d(\sigma v)}{dx} \right|_{\text{Interference}}. \tag{4.22}$$

The expressions for each individual term are rather complicated and are presented in Appendix B[2]. Each of them is separately gauge invariant. In the unitary gauge, the part labeled as "gauge" receives contributions from the diagrams with a charged scalar in the t-channel and generates, in addition to the usual contribution from final state radiation, a spectral feature [105]. The piece labeled as "quartic", on the other hand, receives contributions from the diagrams with the SM Higgs in the s-channel and leads to a spectrum without distinctive spectral features. Then, the shape of the differential photon spectrum from VIB essentially depends on the relative weight of the gauge and the quartic contributions to the cross section, which is in turn determined by the quartic coupling $\lambda_3$.

We show in Fig. 4.5, the three different contributions in Eq. (4.22) as a function of $x = E_\gamma / M_{H^0}$ in the limit $M_{H^0} = M_{H^+}$ for the cases $M_{H^0} = 0.5$ TeV, 1 TeV and 5 TeV and for different values of the quartic coupling $\lambda_3$. We also multiply the spectrum by $x^2$ to emphasize the spectral structure. The blue, green and red lines represent, respectively, the gauge, quartic and interference terms,

---

[2]We have used CalcHEP [131, 132] for parts of the analytical as well as for numerical computations.
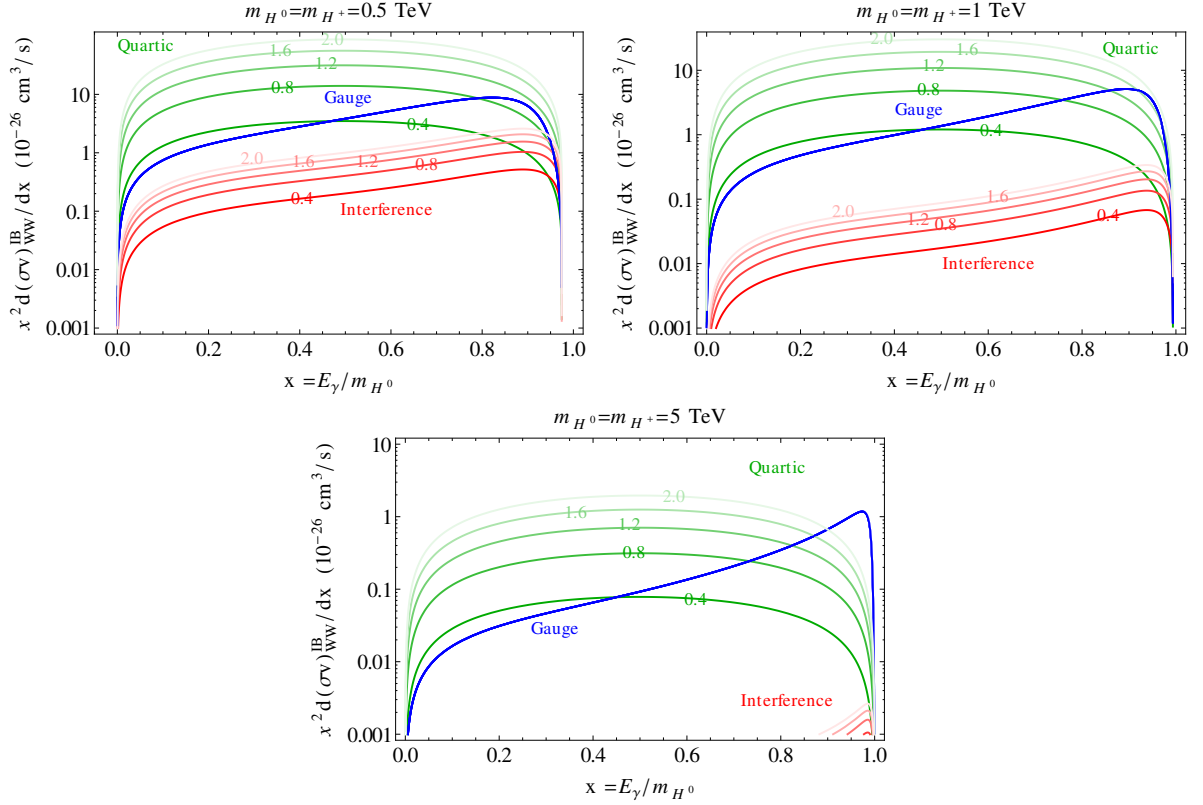
Figure 4.5: Cross section for the VIB process $H^0 H^0 \rightarrow W^+ W^- \gamma$, when the charged scalar is degenerate in mass with the dark matter particle. The blue, green and red lines correspond, respectively, to the gauge, quartic and interference terms, the latter in absolute value. The different darknesses of the lines correspond to varying the absolute value of the quartic coupling $|\lambda_3|$ between 0 (darkest lines) and 2 (lightest lines) in intervals of 0.4 (note that for $|\lambda_3| = 0$ the quartic and interference terms vanish).

the latter in absolute value. Besides, the darkest lines correspond to $|\lambda_3| = 0$ and the lines become lighter as $|\lambda_3|$ is increased in intervals of 0.4, the lightest lines corresponding to $|\lambda_3| = 2$. The pure gauge part produces a spectrum that depends only on the dark matter mass and that displays a feature close to the end-point of the spectrum which becomes sharper and sharper as $M_{H^0}$ increases. The quartic part is proportional to $\lambda_3^2$ and becomes more and more important as $|\lambda_3|$ increases, eventually dominating over the gauge part for values of $x$ closer and closer to one. For a dark matter mass $M_{H^0} = 0.5$ TeV and $|\lambda_3| = 2$ the sharp spectral feature is practically erased in the total spectrum due to the effect of the final state radiation, however, for large dark matter masses the sharp spectral feature remains clearly visible even for $|\lambda_3| = 2$.
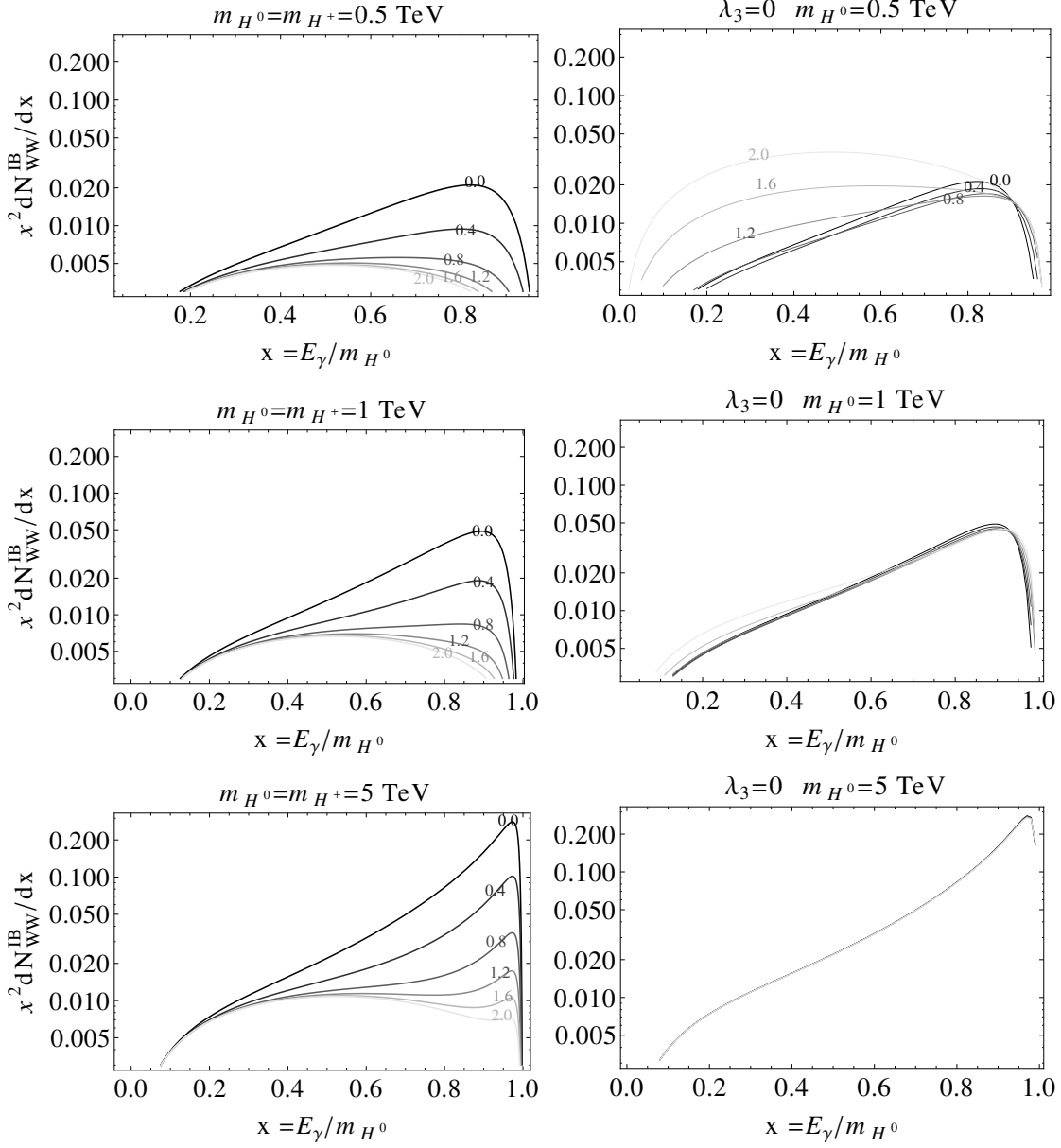
Figure 4.6: Total multiplicity of the VIB process $H^0 H^0 \to W^+ W^- \gamma$. *Left Panel:* the charged scalar is degenerate in mass with the dark matter particle and the different darknesses of the lines correspond to varying the absolute value of the quartic coupling $|\lambda_3|$ between 0 (darkest lines) and 2 (lightest lines) in intervals of 0.4. *Right panel:* $\lambda_3 = 0$ and $(\lambda_4 + \lambda_5)/2$, which controls the mass splitting between the charged scalar and the dark matter, varies between 0 (darkest lines) and $-2$ (lightest lines) in intervals of 0.4.

This behavior can be better appreciated in the left panel of Fig.4.6, where we show the photon multiplicity from VIB, defined as:

$$\frac{dN^{\text{IB}}_{\text{W}^+\text{W}^-\gamma}}{dx} = \frac{1}{(\sigma v)_{W^+W^-}} \frac{d(\sigma v)_{W^+W^-\gamma}}{dx} \ .$$

(4.23)

As before, we consider $M_{H^0} = M_{H^+} = 0.5$ TeV, 1 TeV and 5 TeV and for different values of the quartic coupling $\lambda_3$, the darkest line corresponds to $|\lambda_3| = 0$ and the lightest to $|\lambda_3| = 2$ and the intermediate lines correspond to changing $\lambda_3$ in intervals of 0.4.

For completeness, in the right panel of Fig. 4.6, we also analyze the photon multiplicity from VIB when the neutral and charged exotic Higgs particles are not degenerate in mass. We fixed $\lambda_3 = 0$ and we changed $(\lambda_4 + \lambda_5)/2$ from 0 to $-2$ in intervals of $-0.4$, from darkest to lightest; the mass splitting corresponding to that choice of quartic couplings can be easily derived from $M_{H^+}^2 - M_{H^0}^2 = -\frac{1}{2}(\lambda_4 + \lambda_5)v_h^2$. As expected from the previous discussion, the spectrum is quite insensitive to the mass splitting, as apparent from the plot, especially for large dark matter masses.

# Chapter 5

# Non-Perturbative Effects in Dark Matter Phenomenology

As shown in section 4.1, in the high-mass regime of the IDM, the one-loop annihilation into two photons is described by a cross section that is a constant function of the dark matter mass when all the quartic couplings vanish. For extremely large masses, this results exceeds the upper bound (4.6) set by unitarity. In this chapter we address this problem. In particular, in section 5.1 we identify its origin and argue that this anomalous behavior is alleviated when non-perturbative effects are included.

These effects, as we will see, are associated to long range interactions between the annihilating dark matter particles. In fact, they are related to the exchange of gauge bosons. While this exchange is normally described by the interaction between two currents (see Eq. (3.4)), for scalar particles gauge invariance dictates other interactions (see Eq. (3.8)). Consequently, including such non-perturbative effects demands to consider a formalism where gauge invariance requirements -and particularly the quartic terms from Eq. (3.8)- are accounted for. Such formalism was introduced in [20–24] in the context of neutralino dark matter.

This formalism rests upon the following observation. If the velocity of the dark matter is very small, its dynamics can be described using non-relativistic quantum mechanics. This is however not the situation for the gauge and the Higgs bosons produced in annihilations if the dark matter is very heavy, because in that case these particles are all relativistic. This is circumvented by integrating out these light particles. The resulting effective theory is the non-relativistic limit of the IDM, which we study in detail in this chapter.

## 5.1 Origin of the Problem with Perturbative Unitarity

As shown in section 4.1, the $s$-wave invariant amplitude for the process $H^0 H^0 \to \gamma\gamma$ can be cast as

$$\mathcal{M}\Big|_{s-wave} = A \left( g^{\alpha_3 \alpha_4} - \frac{p_4^{\alpha_3} p_3^{\alpha_4}}{2 M_{H^0}^2} \right) \epsilon_{\alpha_3}(p_3) \epsilon_{\alpha_4}(p_4) \, , \tag{5.1}$$

where $A$ is a complex scalar function of the dark matter mass and the quartic couplings, and the subscripts 3 and 4 refer to the final state photons. The dependence on the other quartic
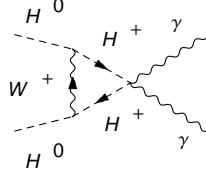
Figure 5.1: Two dark matter particles exchanging a $W$ boson. This diagram leads to a finite piece that violates perturbative unitarity.

couplings $\lambda_2$ and $\lambda_3$ can be separated explicitly as

$$A = A_0(M_{H^0}, M_{H^+}) + A_2(M_{H^0}, M_{H^+}, \lambda_2) + A_3(M_{H^0}, M_{H^+}, \lambda_3). \tag{5.2}$$

Since $\sigma v \left( H^0 H^0 \to \gamma\gamma \right)\big|_{s-wave} = |A|^2/32\pi M_{H^0}^2$, a constant annihilation cross section suggests that $|A| \propto M_{H^0}$. This is indeed the case for $A_0$ as shown in Fig. 4.2. Consequently, the problematic part of the annihilation amplitude must be in the diagrams contributing to this piece of the amplitude. In fact $A_2$ and $A_3$ approach constant values for large dark matter masses as shown in Fig. 4.2 and therefore they do not lead to any problem with unitarity.

This argument implies that the problem with unitarity arises on diagrams that depend only on gauge interactions. For instance, one of such diagrams is shown in Fig. 5.1. There, a $W$ boson is exchanged between the initial state particles. Before analyzing this case carefully, we consider first a similar but simpler process: the up-scattering of two dark matter particles into two charged scalars. For simplicity we assume that all the quartic couplings are set to zero. In that case there are only two Feynman diagrams, which correspond to the exchange of a $W$ boson in the t and u channels. The resulting *tree-level* scattering amplitude is given by

$$\mathcal{M}_{\text{Scattering}} = \left(\frac{g}{2}\right)^2 \left(\frac{-s+u}{t - M_W^2} + \frac{-s+t}{u - M_W^2}\right) \to 2g^2 \left(\frac{M_{H^0}}{M_W}\right)^2 \text{ when } v \to 0. \tag{5.3}$$

For dark matter masses much larger than the $W$ mass, this scattering amplitude is thus arbitrarily large for small velocities. Higher order diagrams are therefore needed to restore partial-wave unitarity. A similar situation happens in one-loop diagrams when a $W$ is exchanged between the initial state particles. As an example, we now consider the diagram of Fig. 5.1 assuming again vanishing quartic couplings. This diagram is divergent, nevertheless it contains a finite piece which exhibits the anomalous behavior that we want to understand. If $q$ is momentum that runs through the $W$ propagator and $P = (M_{H^0}, 0, 0, 0)$ is the dark matter momentum in the s-wave limit, then such finite piece is

$$A_0 \supset 2i(2e^2) \left(\frac{g}{2}\right)^2 (2P)_\mu (2P)_\nu g^{\mu\nu} \mathcal{J} = 64i\pi^2 \alpha \alpha_2 M_{H^0}^2 \mathcal{J}, \tag{5.4}$$

where

$$\mathcal{J} = \int \frac{d^4q}{(2\pi)^4} \frac{1}{(q^2 - M_W^2)\left((q-P)^2 - M_{H^0}^2\right)\left((q+P)^2 - M_{H^0}^2\right)} \tag{5.5}$$

$$= \frac{i}{16\pi^2 M_{H^0} M_W} \int_0^1 dx \frac{1}{\sqrt{1-x}} \arctan\left(\frac{M_{H^0}}{M_W}\frac{x}{\sqrt{1-x}}\right). \tag{5.6}$$

Notice that the loop integral is proportional to $1/(M_{H^0} M_W)$, instead of $1/M_{H^0}^2$, consequently we find that the corresponding piece of the diagram grows with the dark matter mass

$$A_0 \supset -\frac{4\alpha\alpha_2 M_{H^0}}{M_W} \int_0^1 dx \frac{1}{\sqrt{1-x}} \arctan\left(\frac{M_{H^0}}{M_W}\frac{x}{\sqrt{1-x}}\right). \tag{5.7}$$

This result corresponds to a constant contribution to the s-wave cross section according to $\sigma v \left(H^0 H^0 \to \gamma\gamma\right)\Big|_{s-wave} = |A|^2/32\pi M_{H^0}^2$. Although this is only one piece of an individual diagram, it is still possible that -after considering the total gauge-invariant amplitude- this behavior is somehow canceled. However, a posteriori we find that this is not the case, that is, we find that the s-wave cross section is indeed a constant, leading to a violation of unitarity.

Using similar arguments, it is possible to see that for each $W$ boson that is exchanged in the initial state one gets a factor that goes like $\alpha_2 M_{H^0}/M_W$, as we found in Eqs. (5.3) and (5.7). If $M_{H^0} \gtrsim M_W/\alpha_2 \approx 2\,\text{TeV}$, the perturbative calculation breaks down because higher-order loop diagrams become more and more important. For these masses and in general in the high-mass regime of the IDM, the one-loop calculation is not reliable until these effects are taken into account.

In this chapter, we show how to calculate the non-perturbative effects associated to the exchange of light bosons between two annihilating dark matter particles for the high-mass regime of the IDM. To this end, we use the formalism introduced in [20, 22, 24], whose starting point is the following observation. When the dark matter moves slowly, its phenomenology can be described using non-relativistic quantum mechanics. In contrast, this may not be done with the gauge and the Higgs bosons produced in annihilations for very heavy dark matter, because in that case these particles are relativistic. Because of this reason, light particles must be integrated out of the theory. We will see that this process leads to a non-relativistic potential that describes the interaction between pairs of dark matter particles and its $SU(2)_L$ partners. Moreover, since the dark matter and its partners can annihilate into the gauge and the Higgs bosons, there is an absorptive -or imaginary- potential that describes how the dark matter pairs disappear, and therefore the corresponding annihilation rates.

## 5.2 Non-relativistic Expansion of the Inert Fields

When the inert scalars move slowly, the inert doublet $\Psi$ of Eq. (3.2) can be expanded in terms of non-relativistic fields in the following way

$$H^0(x) = \frac{1}{\sqrt{2M_{H^0}}}\left(e^{-iM_{H^0}t}\zeta_{H^0}(x) + e^{+iM_{H^0}t}\zeta_{H^0}^\dagger(x)\right), \tag{5.8}$$

$$A^0(x) = \frac{1}{\sqrt{2M_{H^0}}}\left(e^{-iM_{H^0}t}\zeta_{A^0}(x) + e^{+iM_{H^0}t}\zeta_{A^0}^\dagger(x)\right), \tag{5.9}$$

$$H^+(x) = \frac{1}{\sqrt{2M_{H^0}}}\left(e^{-iM_{H^0}t}\zeta_{H^+}(x) + e^{+iM_{H^0}t}\zeta_{H^-}^\dagger(x)\right), \tag{5.10}$$

where $\zeta_i(\mathrm{x})$ is a non-relativistic field that *annihilates* particles $i$. Because $H^+$ is a charged field, it is expanded in terms of the annihilation field associated to particle $H^+$ and the creation field associated to the antiparticle $H^-$. For the neutral fields $H^0$ and $A^0$, since they are self-conjugate, the creation and annihilation fields in each expansion correspond to the same particle. Because $\zeta_i(\mathrm{x})$ is non-relativistic, its time variations are very small compared to the mass scale, that is,

$$\left|\frac{1}{\zeta_i}\frac{d\zeta_i}{dt}\right| \ll M_{H^0}. \tag{5.11}$$

As we saw in section 3.3, the mass splitting between the different inert particles is negligible compared to the dark matter mass. As a result, in this formalism all the non-relativistic fields are assumed to have the same mass and the corresponding splitting is taken as a perturbation in the action. With this, the kinetic part of the scalar Lagrangian as a function of the non-relativistic fields is given by

$$\begin{aligned}
\mathcal{L}_{\text{Kin}} &= \int d^4x \left(\frac{1}{2}(\partial H^0)^2 + \frac{1}{2}(\partial A^0)^2 + |\partial H^+|^2 - \frac{1}{2}M_{H^0}^2 H^{0\,2} - \frac{1}{2}M_{A^0}^2 A^{0\,2} - M_{H^+}^2|H^+|^2\right) \\
&= \int d^4x \left[\zeta^\dagger\left(i\dot{\zeta} + \frac{\Delta^2\zeta}{2M_{H^0}} - \delta m_\zeta\zeta\right)\right], \tag{5.12}
\end{aligned}$$

with

$$\zeta = \begin{pmatrix} \zeta_{H^0} \\ \zeta_{A^0} \\ \zeta_{H^-} \\ \zeta_{H^+} \end{pmatrix} \quad \text{and} \quad \delta m_\zeta = \begin{pmatrix} 0 & 0 & 0 & 0 \\ 0 & M_{A^0} - M_{H^0} & 0 & 0 \\ 0 & 0 & M_{H^+} - M_{H^0} & 0 \\ 0 & 0 & 0 & M_{H^+} - M_{H^0} \end{pmatrix}. \tag{5.13}$$

In this formula we also include the mass splitting of Eq. (3.13) which is due to quantum effects. Since our goal is to study dark matter annihilations, we must consider pairs $H^0H^0$. However, the exchange of $Z$ and $W$ bosons among the dark matter particles leads to pairs $A^0A^0$ and $H^+H^-$ respectively (see Fig. 5.2). As a result, what we do in the following sections is to derive an effective action that describes these pairs, that is, at a given time $x^0$ we consider

$$s(x,\boldsymbol{y}) = \begin{pmatrix} \frac{\zeta_{H^0}(x)\zeta_{H^0}(x^0,\boldsymbol{y})}{\sqrt{2}} \\ \frac{\zeta_{A^0}(x)\zeta_{A^0}(x^0,\boldsymbol{y})}{\sqrt{2}} \\ \zeta_{H^+}(x)\zeta_{H^-}(x^0,\boldsymbol{y}) \end{pmatrix}. \tag{5.14}$$

The difference in normalization for the first two components of $s(x,\boldsymbol{y})$ comes from the fact that they correspond to states with two identical particles.

## 5.3 Integrating out the Relativistic Particles

### 5.3.1 Gauge Bosons

Before integrating out the gauge bosons, we write their action in a compact way. In the IDM, the action describing the gauge bosons is the sum of a kinetic term and the interaction term of the gauge bosons with the scalar particles

$$\mathcal{S}_{\text{Gauge}} = \mathcal{S}_{\text{Gauge,Kin}} + \mathcal{S}_{\text{Gauge},\Psi}. \tag{5.15}$$

In this chapter we work in the Feynman Gauge, then $\mathcal{S}_{\text{Gauge},\Psi}$ is given by Eqs. (3.3), (3.4) and (3.8), whereas the kinetic term is

$$
\begin{aligned}
\mathcal{S}_{\text{Gauge,Kin}} \ = \ & \int d^4x \left( -\frac{1}{4} \left( F^A F^A + F^Z F^Z + 2 F^{W^-} F^{W^+} \right) + \frac{1}{2} M_Z^2 Z^2 + M_W^2 W^+ W^- \right. \\
& \left. - \frac{1}{2} \left( (\partial A)^2 + (\partial Z)^2 \right) - \partial W^- \partial W^+ \right).
\end{aligned}
\tag{5.16}
$$

As usual $F_{\mu\nu}^V = \partial_\mu V_\nu - \partial_\nu V_\mu$. In order to deal with the gauge bosons collectively, we introduce

$$
\mathcal{A} \ = \ \begin{pmatrix} A \\ Z \\ W^- \\ W^+ \end{pmatrix}.
\tag{5.17}
$$

Using this, the kinetic term can be written as

$$S_{\text{Gauge,Kin}} = \frac{1}{2} \mathcal{A}^\dagger \Delta_0 \mathcal{A} = \frac{1}{2} \int d^4x d^4y \mathcal{A}^\dagger(x) \Delta_0(x,y) \mathcal{A}(y), \tag{5.18}$$

with

$$
(\Delta_0)_{\mu\nu}(x,y) = g_{\mu\nu} \begin{pmatrix} \partial^2 & 0 & 0 & 0 \\ 0 & \partial^2 + M_Z^2 & 0 & 0 \\ 0 & 0 & \partial^2 + M_W^2 & 0 \\ 0 & 0 & 0 & \partial^2 + M_W^2 \end{pmatrix} \delta^{(4)}(x-y).
\tag{5.19}
$$

Similarly,

$$
\begin{aligned}
\mathcal{S}_{\text{Gauge},\Psi} \ & = \ S_{\text{Cubic}} + S_{\text{Quartic}}, && \text{(5.20)} \\
\mathcal{S}_{\text{Cubic}} \ & = \ \mathcal{J}^\dagger \mathcal{A} = \int d^4x \left( J_A^\mu(x) A_\mu(x) + J_Z^\mu(x) Z_\mu(x) + (J_{W^-}^{\mu\dagger}(x) W_\mu^-(x) + h.c.) \right), && \text{(5.21)} \\
\mathcal{S}_{\text{Quartic}} \ & = \ \mathcal{A}^\dagger \mathcal{Q} \mathcal{A} = \int d^4x \, d^4y \mathcal{A}^\dagger(x) \mathcal{Q}(x,y) \mathcal{A}(y), && \text{(5.22)}
\end{aligned}
$$

where

$$
\mathcal{J} = \begin{pmatrix} J_A \\ J_Z \\ J_{W^-} \\ J_{W^+} \end{pmatrix} \text{ and } \mathcal{Q}(x,y) = \begin{pmatrix} Q_{AA}(x) & Q_{AZ}(x) & Q_{AW}(x) & Q_{AW}^*(x) \\ Q_{AZ}(x) & Q_{ZZ}(x) & Q_{ZW}(x) & Q_{ZW}^*(x) \\ Q_{AW}^*(x) & Q_{ZW}^*(x) & Q_{WW}(x) & 0 \\ Q_{AQ}(x) & Q_{ZW}(x) & 0 & Q_{WW}(x) \end{pmatrix} \delta^{(4)}(x-y),
\tag{5.23}
$$

$$Q_{AA} = e^2 H^+ H^-, \qquad Q_{ZZ} = \frac{g^2}{4c_W^2}\left(\frac{1}{2}(H^{02} + A^{02}) + (1 - 2c_W^2)^2 H^+ H^-\right),$$

$$Q_{AZ} = \frac{eg(1-2c_W^2)}{2c_W} H^+ H^-, \qquad Q_{WW} = \frac{g^2}{4}\left(\frac{1}{2}(H^{02} + A^{02}) + H^+ H^-\right),$$

$$Q_{AW} = \frac{g^2 s_W}{4} H^+(H^0 - iA^0), \quad Q_{ZW} = -\frac{g^2 c_W}{4} H^+(H^0 - iA^0).$$

With this, the total action is

$$\mathcal{S}_{\text{Gauge}} = \frac{1}{2}\mathcal{A}^\dagger \Delta \mathcal{A} + \mathcal{J}^\dagger \mathcal{A}, \qquad \text{where} \qquad \Delta = \Delta_0 + 2\mathcal{Q}. \tag{5.24}$$

In order to integrate out the gauge fields, we perform the path integral with respect to $\mathcal{A}$. Notice that $\mathcal{A}^\dagger$ is not an independent variable because it is related to $\mathcal{A}$ by permuting its third and fourth components. Moreover, notice that $\mathcal{J}^\dagger \mathcal{A} = \mathcal{A}^\dagger \mathcal{J}$. Then the path integral is

$$Z_{\text{Gauge}} = \int \mathcal{D}\mathcal{A}\, e^{i\left(\frac{1}{2}\mathcal{A}^\dagger \Delta \mathcal{A} + \mathcal{J}^\dagger \mathcal{A}\right)}. \tag{5.25}$$

In order to perform the integration, we consider field oscillations around the stationary value of the action, that is, around the classical solution, which is given by

$$\mathcal{A}_{\text{cl}} = -\Delta^{-1}\mathcal{J}. \tag{5.26}$$

Consequently, in Eq. (5.25) we make the following replacement $\mathcal{A} \to \mathcal{A} + \mathcal{A}_{\text{cl}}$. After some simplifications one obtains

$$Z_{\text{Gauge}} = \left(\int \mathcal{D}\mathcal{A}\, e^{\frac{i}{2}\mathcal{A}^\dagger \Delta \mathcal{A}}\right) e^{-\frac{i}{2}\mathcal{J}^\dagger \Delta^{-1}\mathcal{J}}. \tag{5.27}$$

The integral in the parenthesis can be performed by means of a change of variables. In fact,

$$\int \mathcal{D}\mathcal{A}\, e^{\frac{i}{2}\mathcal{A}^\dagger \Delta \mathcal{A}} = \mathcal{N}\, (\text{Det}\Delta)^{-\frac{1}{2}} = \mathcal{N}e^{-\frac{1}{2}\text{Tr}\log\Delta}, \tag{5.28}$$

where $\mathcal{N}$ is an arbitrary constant. As a result,

$$Z_{\text{Gauge}} = \mathcal{N}e^{iS_{\text{eff}}}, \quad \text{and} \quad S_{\text{eff}} = -\frac{1}{2}\mathcal{J}^\dagger \Delta^{-1}\mathcal{J} + \frac{i}{2}\text{Tr}\,\log\Delta\,. \tag{5.29}$$

Our goal now is to simply $S_{\text{eff}}$ as much as possible. On the one hand, by expanding $\Delta$ in terms of $\mathcal{Q}$, which is proportional to the gauge coupling constants, one obtains at leading order

$$\Delta^{-1} = (\Delta_0 - 2\mathcal{Q})^{-1} = \Delta_0^{-1} - 2\Delta_0^{-1}\mathcal{Q}\Delta_0^{-1}. \tag{5.30}$$

The second term in the previous equation and each current $\mathcal{J}$ are quadratic in the inert fields. Since in this work we do not consider effective interactions with six legs of inert scalars, we can assume in Eq. (5.29) that

$$\mathcal{J}^\dagger \Delta^{-1}\mathcal{J} = \mathcal{J}^\dagger \Delta_0^{-1}\mathcal{J}. \tag{5.31}$$

Likewise, we can expand the second term of the effective action in terms of $\mathcal{Q}$. Indeed,

$$
\begin{aligned}
\frac{i}{2}\mathrm{Tr}\ \log \Delta &= \frac{i}{2}\mathrm{Tr}\ \log \left[\Delta_0(1 + 2\Delta_0^{-1}\mathcal{Q})\right] = \frac{i}{2}\mathrm{Tr}\left[\log \Delta_0 + \log\left(1 + 2\Delta_0^{-1}\mathcal{Q}\right)\right] \\
&= \frac{i}{2}\left[\mathrm{Tr}\ \log \Delta_0 + 2\,\mathrm{Tr}\log\left(\Delta_0^{-1}\mathcal{Q}\right) - 2\,\mathrm{Tr}\log\left(\Delta_0^{-1}\mathcal{Q}\Delta_0^{-1}\mathcal{Q}\right)\right].
\end{aligned} \tag{5.32}
$$

Here the first term only contributes to $\mathcal{N}$ and it is therefore irrelevant. The second term is quadratic in the scalar fields and it accounts for radiative corrections to the mass. After moving these corrections into the scalar mass terms, we obtain the following effective action

$$
S_{\mathrm{eff}} = S_{\mathrm{eff},1} + S_{\mathrm{eff},2}, \tag{5.33}
$$

$$
S_{\mathrm{eff},1} = -\frac{1}{2}\mathcal{J}^\dagger \Delta_0^{-1}\mathcal{J}, \tag{5.34}
$$

$$
S_{\mathrm{eff},2} = -i\,\mathrm{Tr}\log\left(\Delta_0^{-1}\mathcal{Q}\Delta_0^{-1}\mathcal{Q}\right). \tag{5.35}
$$

From this procedure we can clearly see that $S_{\mathrm{eff},1}$ is the contribution of the cubic gauge terms to the effective interactions between the scalars once the gauge bosons are integrated out, whereas $S_{\mathrm{eff},2}$ is associated to the quartic guage interactions.

**Coulomb and Yukawa Interactions**   We now calculate $S_{\mathrm{eff},1}$ in the non-relativistic limit. We start by noticing that

$$
(\Delta_0)_{\mu\nu}^{-1}(x,y) = -\int \frac{d^4q}{(2\pi)^4}e^{iq(x-y)}\begin{pmatrix} \frac{1}{q^2+i\epsilon} & 0 & 0 & 0 \\ 0 & \frac{1}{q^2-M_Z^2+i\epsilon} & 0 & 0 \\ 0 & 0 & \frac{1}{q^2-M_W^2+i\epsilon} & 0 \\ 0 & 0 & 0 & \frac{1}{q^2-M_W^2+i\epsilon} \end{pmatrix}g_{\mu\nu} \tag{5.36}
$$

and hence

$$
S_{\mathrm{eff},1} = \int \frac{d^4x\,d^4y\,d^4q}{2(2\pi)^4}e^{iq(x-y)}\left(\frac{J_A^\mu(x)J_{A\mu}(y)}{q^2+i\epsilon} + \frac{J_Z^\mu(x)J_{Z\mu}(y)}{q^2-M_Z^2+i\epsilon} + \frac{2J_{W^+}^\mu(x)J_{W^-\mu}(y)}{q^2-M_W^2+i\epsilon}\right). \tag{5.37}
$$

We would like to calculate this action in the non-relativistic limit. To this end, we write each current as $J_V = (J_V^0, \boldsymbol{J_V})$, where $V$ is any of the gauge bosons. With this, each term of Eq. (5.34) can be written as

$$
\frac{J_V^\mu(x)J_{V\mu}(y)}{q^2-M_V^2+i\epsilon} = -\frac{J_V^0(x)J_V^0(y)}{\boldsymbol{q}^2+M_V^2} + \frac{J_V^0(x)J_V^0(y)\,q^{0\,2}}{(\boldsymbol{q}^2+M_V^2)(q^2-M_V^2+i\epsilon)} + \frac{\boldsymbol{J_V}(x)\boldsymbol{J_{V\mu}}(y)}{q^2-M_V^2+i\epsilon}. \tag{5.38}
$$

The third term of this equation contains the magnetic interactions between the currents. For non-relativistic currents, we expect $|\boldsymbol{J_V}| \ll J_V^0$ and consequently this term can be neglected. In addition, the second term is related to retarded effects on the interaction between the currents. In fact, integrating by parts it can be written as

$$
\int \frac{d^4x\,d^4y\,d^4q\ e^{iq(x-y)}J_V^0(x)J_V^0(y)\,q^{0\,2}}{(\boldsymbol{q}^2+M_V^2)(q^2-M_V^2+i\epsilon)} = \int \frac{d^4x\,d^4y\,d^4q\ e^{iq(x-y)}\dot{J}_V^0(x)\dot{J}_V^0(y)}{(\boldsymbol{q}^2+M_V^2)(q^2-M_V^2+i\epsilon)}. \tag{5.39}
$$
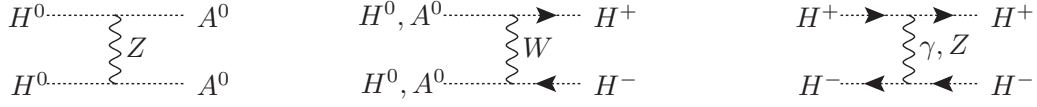
Figure 5.2: Feynman diagrams contributing to $V_{\text{Gauge}}(r)$.

Because of Eq. (5.11), we can conclude that $|\dot{J}_V^0| \ll J_V^0$ and therefore retarded effects can be neglected in the non-relativistic limit as well. In contrast, the first of Eq. (5.38) can not be neglected and the integration in the momentum space must be done. This is given by

$$\int \frac{d^4q}{(2\pi)^4} \frac{e^{iq(x-y)}}{\boldsymbol{q}^2 + M_V^2} = \delta(x^0 - y^0) \int \frac{d^3q}{(2\pi)^3} \frac{e^{iq(x-y)}}{\boldsymbol{q}^2 + M_V^2} = \frac{e^{-M_V|\boldsymbol{x}-\boldsymbol{y}|}}{4\pi|\boldsymbol{x}-\boldsymbol{y}|}\delta(x^0 - y^0). \tag{5.40}$$

Consenquently,

$$\begin{aligned}
S_{\text{eff},1} &= -\int \frac{d^4x d^3y}{8\pi|\boldsymbol{x}-\boldsymbol{y}|} \left( J_A^0(x)J_A^0(x^0,\boldsymbol{y}) + J_Z^0(x)J_Z^0(x^0,\boldsymbol{y})e^{-M_Z|\boldsymbol{x}-\boldsymbol{y}|} \right. \\
&\quad + \left. 2\, J_{W^+}^0(x)J_{W^-}^0(x^0,\boldsymbol{y})e^{-M_W|\boldsymbol{x}-\boldsymbol{y}|} \right).
\end{aligned} \tag{5.41}$$

Hence, in the non-relativistic limit the first term of $S_{\text{eff},1}$ describes the Coulomb force between the non-relativistic particles, whereas the other terms describe Yukawa interactions associated to the exchange of $W$ and $Z$ bosons.

As explained in the previous section, we consider only pairs $H^0 H^0$, $A^0 A^0$ and $H^+ H^-$. As a consequence we limit ourselves to describe interactions corresponding to these pairs of particles. With this in mind, we write the time-like components of the currents in terms of the non-relativistic fields of Eq. (5.10)

$$J_A^0 \supset e\left( -\zeta_{H^-}\zeta_{H^-}^\dagger + \zeta_{H^+}^\dagger \zeta_{H^+} \right) \tag{5.42}$$

$$J_Z^0 \supset \frac{g}{2c_W} \left[ (1 - 2c_W^2)\left( -\zeta_{H^-}\zeta_{H^-}^\dagger + \zeta_{H^+}^\dagger \zeta_{H^+} \right) + i\left( -\zeta_{A^0}\zeta_{H^0}^\dagger + \zeta_{H^0}\zeta_{A^0}^\dagger \right) \right] \tag{5.43}$$

$$J_{W^-}^0 \supset \frac{g}{2} \left[ -\zeta_{H^-}\left( \zeta_{H^0}^\dagger + i\,\zeta_{A^0}^\dagger \right) + \zeta_{H^+}^\dagger \left( \zeta_{H^0} + i\,\zeta_{A^0} \right) \right] \tag{5.44}$$

Here the terms that are omitted are the ones that do not lead to pairs $H^0 H^0$, $A^0 A^0$ and $H^+ H^-$. By plugging these currents in Eq. (5.41), we obtain

$$S_{\text{eff},1} = -\int d^4x d^3y\; s(x,\boldsymbol{y})^\dagger V_{\text{Gauge}}(|\boldsymbol{x}-\boldsymbol{y}|)s(x,\boldsymbol{y}) \tag{5.45}$$

where $s(x,\boldsymbol{y})$ was introduced in Eq. (5.14) and

$$V_{\text{Gauge}}(r) = -\frac{g^2}{4\pi r} \begin{pmatrix} 0 & \frac{e^{-M_Z r}}{4c_W^2} & \frac{e^{-M_W r}}{2\sqrt{2}} \\ \frac{e^{-M_Z r}}{4c_W^2} & 0 & \frac{e^{-M_W r}}{2\sqrt{2}} \\ \frac{e^{-M_W r}}{2\sqrt{2}} & \frac{e^{-M_W r}}{2\sqrt{2}} & s_W^2 + \frac{(1-2c_W^2)^2 e^{-M_Z r}}{4c_W^2} \end{pmatrix}. \tag{5.46}$$
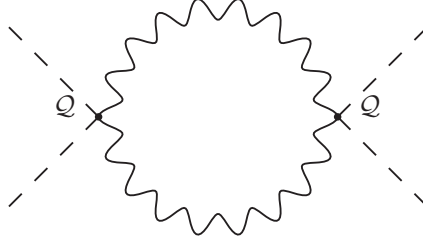
Figure 5.3: Sort of Feynman diagrams contributing to $S_{\text{eff},2} = -i \operatorname{Tr} \log \left( \Delta_0^{-1} \mathcal{Q} \Delta_0^{-1} \mathcal{Q} \right)$.

**Absorptive Term**   In general non-relativistic inert scalars can annihilate into relativistic particles, in this case into gauge bosons. Since we are integrating out the latter, in the effective theory the annihilations are described by an imaginary potential -or an absorptive term in the action- which allows for the disappearance of pairs of non-relativistic particles. We argue here that the absorptive term comes from $S_{\text{eff},2}$ given in Eq. (5.35). We first interpret $S_{\text{eff},2}$ in terms of Feynman diagrams by noticing that the matrix $\Delta_0^{-1}$ describes the propagators of the gauge fields, whereas each $\mathcal{Q}$ is a vertex with two gauge fields and two inert scalar fields. Consequently each term of $S_{\text{eff},2}$ is a diagram like the one shown in Fig. 5.3. Furthermore, for simplicity we neglect the mass of the gauge bosons and then we have

$$
\begin{aligned}
S_{\text{eff},2} &= -i \operatorname{Tr} \log \left( \Delta_0^{-1} \mathcal{Q} \Delta_0^{-1} \mathcal{Q} \right) \\
&= -4i \int d^4x d^4y d^4z d^4w \frac{d^4q}{(2\pi)^4} \frac{d^4k}{(2\pi)^4} \frac{e^{iq(x-y)}}{q^2 + i\epsilon} \frac{e^{ik(z-w)}}{k^2 + i\epsilon} \operatorname{Tr}[\mathcal{Q}(y,z)\mathcal{Q}(w,x)].
\end{aligned}
\tag{5.47}
$$

The factor of 4 is the trace over the space-time index of the gauge fields. Since we are interested in the imaginary part, we set the gauge bosons in the loop on-shell by performing

$$
\frac{1}{q^2 + i\epsilon} \to -2\pi i \delta(q^2).
\tag{5.48}
$$

Furthermore, we carry out the integration over the time-like component of the four-momenta by noticing that $d^4q \, \delta(q^2) \to \frac{d^3q}{2|\boldsymbol{q}|}$ when the gauge particles are on-shell. In this way the integration over the four-momenta can be cast as

$$
\begin{aligned}
\int \frac{d^4q}{(2\pi)^4} \frac{d^4k}{(2\pi)^4} \frac{e^{iq(x-y)}}{q^2 + i\epsilon} \frac{e^{ik(z-w)}}{k^2 + i\epsilon} \quad &\to \quad (-i)^2 \int \frac{d^3q}{(2\pi)^3(2|\boldsymbol{q}|)} \frac{d^3k}{(2\pi)^3(2|\boldsymbol{k}|)} e^{i(q-k)(x-y)} \\
&= -\int d^4Q \frac{d^3q}{(2\pi)^3(2|\boldsymbol{q}|)} \frac{d^3k}{(2\pi)^3(2|\boldsymbol{k}|)} \delta^{(4)}(Q - q + k) e^{iQ(x-y)} \\
&\to -\frac{1}{8\pi} \int \frac{d^4Q}{(2\pi)^4} e^{iQ(x-y)} = -\frac{i}{8\pi} \delta^{(4)}(x-y).
\end{aligned}
\tag{5.49}
$$

If we plug this into Eq. (5.47), we obtain

$$
S_{\text{eff},2} = \frac{i}{2\pi} \int d^4x \operatorname{Tr} \left\{ \begin{pmatrix} Q_{AA}(x) & Q_{AZ}(x) & Q_{AW}(x) & Q_{AW}^*(x) \\ Q_{AZ}(x) & Q_{ZZ}(x) & Q_{ZW}(x) & Q_{ZW}^*(x) \\ Q_{AW}^*(x) & Q_{ZW}^*(x) & Q_{WW}(x) & 0 \\ Q_{AQ}(x) & Q_{ZW}(x) & 0 & Q_{WW}(x) \end{pmatrix}^2 \right\}.
\tag{5.50}
$$
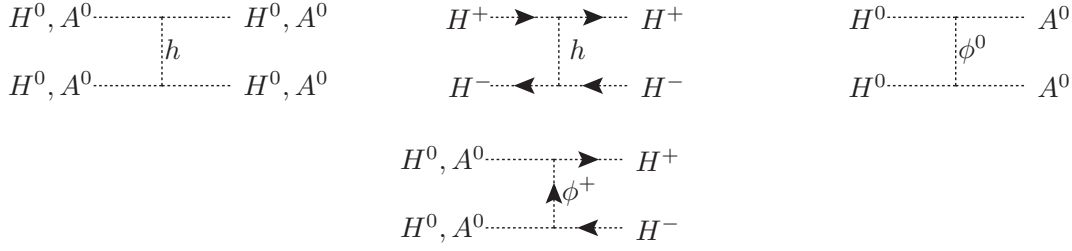
Figure 5.4: Feynman diagrams contributing to $V_{\text{Scalar}}(\text{r})$

Keeping again only the terms that give rise to pairs $H^0 H^0$, $A^0 A^0$ and $H^+ H^-$, one obtains

$$
\begin{aligned}
S_{\text{eff},2} &= \frac{i}{2\pi} \int d^4x \left( Q_{AA}(x)^2 + Q_{ZZ}(x)^2 + 2\, Q_{WW}(x)^2 + 2 Q_{AZ}(x)^2 \right) \\
&= \frac{ig^4}{16\pi} \int d^4x \left[ \left( 8s_W^4 + \frac{4s_W^2(1-2c_W^2)^2}{c_W^2} + \frac{(1-2c_W^2)^4}{2c_W^4} + 1 \right) (H^+H^-)^2 \right. \\
&\quad + \left. \frac{1}{4}\left( \frac{1}{2s_W^4} + 1 \right) \left( H^{02} + A^{02} \right)^2 + \left( \frac{(1-2c_W^2)^2}{2c_W^4} + 1 \right) \left( H^{02} + A^{02} \right) H^+H^- \right].
\end{aligned}
\tag{5.51}
$$

This expression is manifestly imaginary and therefore corresponds to an absorptive action as expected. In terms of the non-relativistic fields of Eq. (5.10), it can be written as

$$
S_{\text{eff},2} = 2i \int d^4x d^3y \; s(x,\boldsymbol{y})^\dagger \Gamma_{\text{Gauge}} \delta^{(3)}(|\boldsymbol{x} - \boldsymbol{y}|) s(x,\boldsymbol{y}),
\tag{5.52}
$$

where $s(x,\boldsymbol{y})$ was introduced in Eq. (5.14) and

$$
\Gamma_{\text{Gauge}} = \frac{1}{32\pi M_{H^0}^2}
\begin{pmatrix}
\frac{a}{2} & \frac{a}{2} & \frac{b}{\sqrt{2}} \\
\frac{a}{2} & \frac{a}{2} & \frac{b}{\sqrt{2}} \\
\frac{b}{\sqrt{2}} & \frac{b}{\sqrt{2}} & c
\end{pmatrix},
\tag{5.53}
$$

$$
a = \frac{g^4}{2}\left( \frac{1}{2s_W^4} + 1 \right), \qquad b = \frac{g^4}{2}\left( \frac{(1-c_W^2)^2}{2s_W^4} + 1 \right),
$$

$$
c = g^4 \left( 4s_W^4 + \frac{2s_W^2(1-2c_W^2)^2}{c_W^2} + \frac{(1-2c_W^2)^4}{4c_W^4} + \frac{1}{2} \right).
$$

Hence the path integral (5.29) after integrating out the gauge bosons is

$$
Z_{\text{Gauge}} = \mathcal{N} \exp\{i \int d^4x d^3y \; s(x,\boldsymbol{y})^\dagger \left( -V_{\text{Gauge}}(|\boldsymbol{x} - \boldsymbol{y}|) + 2i\Gamma_{\text{Gauge}} \delta^{(3)}(|\boldsymbol{x} - \boldsymbol{y}|) \right) s(x,\boldsymbol{y})\}.
\tag{5.54}
$$

## 5.3.2 The Higgs and the Goldstone Bosons

In the Feynman Gauge, the masses of the Goldstone bosons $G^\pm$ and $G^0$ from the doublet $\Phi$ of Eq. (3.2) are $M_W$ and $M_Z$. These along the Higgs particle are very light compared to the inert scalars in the high-mass regime of the IDM. Accordingly they must be integrated out. This is done in exactly the same way as in the previous section. Moreover, this integration is simpler

because $h, G^0$ and $G^\pm$ are scalars as opposed to the gauge bosons which are described by vector fields. After performing the integration one obtains

$$Z_{\text{Scalar}} = \mathcal{N} \exp\{i \int d^4x d^3y \; s(x,\boldsymbol{y})^\dagger \left(-V_{\text{Scalar}}(|\boldsymbol{x}-\boldsymbol{y}|) + 2i\Gamma_{\text{Scalar}}\delta^{(3)}(|\boldsymbol{x}-\boldsymbol{y}|)\right) s(x,\boldsymbol{y}), \} \quad (5.55)$$

where $V_{\text{Scalar}}$ arises from the exchange of light scalars between the pairs $H^0 H^0$, $A^0 A^0$ and $H^+ H^-$ as shown in Fig. 5.4, and it is given by

$$V_{\text{Scalar}}(r) = -\frac{v_h^2}{8\pi r M_{H^0}^2} \begin{pmatrix} \frac{(\lambda_3+\lambda_4+\lambda_5)^2}{2}e^{-M_h r} & \frac{\lambda_5^2}{4}e^{-M_Z r} & \frac{(\lambda_4+\lambda_5)^2}{4\sqrt{2}}e^{-M_W r} \\ \frac{\lambda_5^2}{4}e^{-M_Z r} & \frac{(\lambda_3+\lambda_4-\lambda_5)^2}{2}e^{-M_h r} & \frac{(\lambda_4-\lambda_5)^2}{4\sqrt{2}}e^{-M_W r} \\ \frac{(\lambda_4+\lambda_5)^2}{4\sqrt{2}}e^{-M_W r} & \frac{(\lambda_4-\lambda_5)^2}{4\sqrt{2}}e^{-M_W r} & \frac{\lambda_3^2}{2}e^{-M_h r} . \end{pmatrix} \quad (5.56)$$

Notice that this potential is suppressed by the dark matter mass squared. This is due to the fact that the cubic interactions -according to the potential of Eq. (3.9)- have dimensionful couplings proportional to $v_h^2$.

Similarly, $\Gamma_{\text{Scalar}}$ arises from the quartic interactions of the potential in Eq. (3.9) and it is

$$\Gamma_{\text{Scalar}} = \frac{1}{32\pi M_{H^0}^2} \begin{pmatrix} \lambda_3^2 + \lambda_4\lambda_3 + \frac{\lambda_4^2}{2} + \frac{\lambda_5^2}{2} & \lambda_3^2 + \lambda_4\lambda_3 + \frac{\lambda_4^2}{2} - \frac{\lambda_5^2}{2} & \sqrt{2}\lambda_3(\lambda_3+\lambda_4) \\ \lambda_3^2 + \lambda_4\lambda_3 + \frac{\lambda_4^2}{2} - \frac{\lambda_5^2}{2} & \lambda_3^2 + \lambda_4\lambda_3 + \frac{\lambda_4^2}{2} + \frac{\lambda_5^2}{2} & \sqrt{2}\lambda_3(\lambda_3+\lambda_4) \\ \sqrt{2}\lambda_3(\lambda_3+\lambda_4) & \sqrt{2}\lambda_3(\lambda_3+\lambda_4) & 2\lambda_3^2 + 2\lambda_4\lambda_3 + \lambda_4^2 \end{pmatrix}. \quad (5.57)$$

## 5.4 Effective Action for Pairs of Inert Particles

Putting together Eqs. (5.12),(5.54) and (5.55), one gets the path integral over the non-relativistic fields of Eq. (5.10), which reads

$$Z = \int \mathcal{D}\zeta \, \mathcal{D}\zeta^\dagger \; \exp\left\{ i \int d^4x \left[ \zeta(x)^\dagger \left( i\dot{\zeta}(x) + \frac{\Delta^2\zeta(x)}{2M_{H^0}} - \delta m_\zeta \zeta(x) \right) \right] \right. \quad (5.58)$$

$$+ \quad i \int d^4x d^3y \; s(x,\boldsymbol{y})^\dagger \left( -(V_{\text{Gauge}} + V_{\text{Scalar}})(|\boldsymbol{x}-\boldsymbol{y}|) + 2i(\Gamma_{\text{Scalar}} + \Gamma_{\text{Scalar}})\delta^{(3)}(|\boldsymbol{x}-\boldsymbol{y}|) \right) s(x,\boldsymbol{y}) \right\},$$

where

$$s(x,\boldsymbol{y}) = \begin{pmatrix} s_1(x,\boldsymbol{y}) \\ s_2(x,\boldsymbol{y}) \\ s_3(x,\boldsymbol{y}) \end{pmatrix} = \begin{pmatrix} \frac{\zeta_{H^0}(x)\zeta_{H^0}(x^0,\boldsymbol{y})}{\sqrt{2}} \\ \frac{\zeta_{A^0}(x)\zeta_{A^0}(x^0,\boldsymbol{y})}{\sqrt{2}} \\ \zeta_{H^+}(x)\zeta_{H^-}(x^0,\boldsymbol{y}) \end{pmatrix}. \quad (5.59)$$

In the previous expression $s(x,\boldsymbol{y})$, is not a dynamical field. However, we can apply the following identity to introduce a path integral over it [1]

$$1 \quad = \int \mathcal{D}s \, \mathcal{D}s^\dagger \, \mathcal{D}\sigma \, \mathcal{D}\sigma^\dagger \; \exp\left\{ i \int d^4x d^3y \left( \sigma_1(x,\boldsymbol{y})^\dagger \left( s_1(x,\boldsymbol{y}) - \frac{\zeta_{H^0}(x)\zeta_{H^0}(x^0,\boldsymbol{y})}{\sqrt{2}} \right) \right. \right. \quad (5.61)$$

$$+ \quad \sigma_2(x,\boldsymbol{y})^\dagger \left( s_2(x,\boldsymbol{y}) - \frac{\zeta_{A^0}(x)\zeta_{A^0}(x^0,\boldsymbol{y})}{\sqrt{2}} \right) + \sigma_3(x,\boldsymbol{y})^\dagger \left( s_3(x,\boldsymbol{y}) - \zeta_{H^+}(x)\zeta_{H^-}(x^0,\boldsymbol{y}) \right) + h.c. \right) \right\}.$$

---

[1]This identity is a generalization of

$$1 = \int \frac{dx \, dp}{2\pi} \; e^{i(x-a)}. \quad (5.60)$$

With this the path integral of Eq. (5.59) can be cast as

$$
Z = \int \mathcal{D}\zeta \, \mathcal{D}\zeta^\dagger \, \mathcal{D}s \, \mathcal{D}s^\dagger \, \mathcal{D}\sigma \, \mathcal{D}\sigma^\dagger \, \exp \left\{ i \int d^4x \zeta(x)^\dagger \left( i\dot\zeta(x) + \frac{\Delta^2 \zeta(x)}{2M_{H^0}} - \delta m_\zeta \zeta(x) \right) \right.
\tag{5.62}
$$

$$
+ \quad i \int d^4x d^3y \left[ s(x,\boldsymbol{y})^\dagger \left( -(V_{\text{Gauge}} + V_{\text{Scalar}})(|\boldsymbol{x}-\boldsymbol{y}|) + 2i(\Gamma_{\text{Scalar}} + \Gamma_{\text{Scalar}})\delta^{(3)}(|\boldsymbol{x}-\boldsymbol{y}|) \right) s(x,\boldsymbol{y}) \right.
$$

$$
+ \quad \left( \sigma_1(x,\boldsymbol{y})^\dagger \left( s_1(x,\boldsymbol{y}) - \frac{\zeta_{H^0}(x)\zeta_{H^0}(x^0,\boldsymbol{y})}{\sqrt{2}} \right) + \sigma_2(x,\boldsymbol{y})^\dagger \left( s_2(x,\boldsymbol{y}) - \frac{\zeta_{A^0}(x)\zeta_{A^0}(x^0,\boldsymbol{y})}{\sqrt{2}} \right) \right.
$$

$$
+ \quad \sigma_3(x,\boldsymbol{y})^\dagger \left( s_3(x,\boldsymbol{y}) - \zeta_{H^+}(x)\zeta_{H^-}(x^0,\boldsymbol{y}) \right) + h.c.) \Big] \Big\}.
$$

The full Lagrangian at this point is quadratic in the non-relativistic fields $\zeta$ and $\zeta^\dagger$, with coefficients that depend on the field $\sigma(x,\boldsymbol{y})$. Therefore, the path integral with respect to these variables can be performed using elementary methods of path integration. The result is

$$
\begin{aligned}
Z &= \int \mathcal{D}s \, \mathcal{D}s^\dagger \, \mathcal{D}\sigma \, \mathcal{D}\sigma^\dagger \, \exp \left\{ i \int d^4x d^3y \left( -\sigma(x,\boldsymbol{y})^\dagger \mathcal{K}^{-1}(x,\boldsymbol{y})\sigma(x,\boldsymbol{y}) - s(x,\boldsymbol{y})^\dagger \mathcal{V}(x,\boldsymbol{y}) s(x,\boldsymbol{y}) \right. \right. \\
&+ \quad \sigma(x,\boldsymbol{y})^\dagger s(x,\boldsymbol{y}) + s(x,\boldsymbol{y})^\dagger \sigma(x,\boldsymbol{y}) \Big) \Big\},
\end{aligned}
\tag{5.63}
$$

where

$$
\mathcal{K}(x,\boldsymbol{y}) = i\partial_{x^0} - \frac{\nabla_{\boldsymbol{x}}^2}{2M_{H^0}} - \frac{\nabla_{\boldsymbol{y}}^2}{2M_{H^0}} + 2 \, \delta m,
\tag{5.64}
$$

$$
\mathcal{V}(x,\boldsymbol{y}) = (V_{\text{Gauge}} + V_{\text{Scalar}})(|\boldsymbol{x}-\boldsymbol{y}|) - 2i(\Gamma_{\text{Scalar}} + \Gamma_{\text{Scalar}})\delta^{(3)}(|\boldsymbol{x}-\boldsymbol{y}|),
\tag{5.65}
$$

with

$$
\delta m = \begin{pmatrix} 0 & 0 & 0 \\ 0 & M_{A^0} - M_{H^0} & 0 \\ 0 & 0 & M_{H^+} - M_{H^0} \end{pmatrix}.
\tag{5.66}
$$

The stationary value of the action associated to Eq. (5.63) is given by

$$
\sigma(x,\boldsymbol{y}) = \mathcal{V}(x,\boldsymbol{y})s(x,\boldsymbol{y}) \qquad \text{and} \qquad s(x,\boldsymbol{y}) = \mathcal{K}^{-1}(x,\boldsymbol{y})\sigma(x,\boldsymbol{y}).
\tag{5.67}
$$

With this it is possible to integrate out the field $\sigma(x,\boldsymbol{y})$. The final result for the path integral over the filed $s(x,\boldsymbol{y})$ that describes the pairs $H^0 H^0$, $A^0 A^0$ and $H^+ H^-$ in the non-relativistic limit is

$$
Z = \int \mathcal{D}s \, \mathcal{D}s^\dagger \, \exp \left\{ i \int d^4x d^3r \, s^\dagger(x,\vec{r}) \left( i\partial_{x^0} + \frac{\nabla_x^2}{4M_{H^0}} + \frac{\nabla_r^2}{M_{H^0}} - V(r) + 2i\Gamma\delta(\vec{r}) \right) s(x,\vec{r}) \right\}.
\tag{5.68}
$$

Here $x$ is the position of the center of mass and $\vec{r}$ is the relative position vector for the pair of particles. In addition $V(r)$ is a $3 \times 3$ potential matrix and $\Gamma$ is a $3 \times 3$ matrix that characterizes the tree-level annihilation rates

$$
V(r) = 2 \, \delta m + V_{\text{Gauge}}(r) + V_{\text{Scalar}}(r) \qquad \text{and} \qquad \Gamma = \Gamma_{\text{Gauge}} + \Gamma_{\text{Scalar}}.
\tag{5.69}
$$

## 5.5 Another Way to Calculate the Annihilation Matrix Γ

Using the Optical Theorem, in [22] it was proven that the matrix $\Gamma$ can also be calculated by considering all the possible final states of the light particles that are integrated out. In fact,

$$\Gamma = \sum_f \Gamma_f, \tag{5.70}$$

where $f$ is any final state in which the pair of dark matter particles or its partners can annihilate into. For each of them

$$(\Gamma_f)_{ii',jj'} = \frac{N_{ii'}N_{jj'}}{4M_{H^0}^2} \int \left( \prod_{a \in f} \frac{d^3 q_a}{(2\pi)^3 2E_a} \right) (2\pi)^4 \delta^4 \left( p_i + p_i' - \sum_{a \in f} q_a \right) \mathcal{M}\left(ii' \to f\right) \mathcal{M}\left(jj' \to f\right)^* , \tag{5.71}$$

where $N_{H^0 H^0} = N_{A^0 A^0} = 1/\sqrt{2}$ and $N_{H^- H^+} = 1$. Also, $\mathcal{M}\left(ii' \to f\right)$ stands for the tree-level scattering amplitude for the corresponding annihilation process.

**Two-body final state processes**

For the IDM, in these cases the matrix $\Gamma_f$ can be cast as

$$\Gamma_f = \frac{1}{32\pi M_{H^0}^2} \left( V_G^{fT} V_G^f + V_S^{fT} V_S^f \right) , \tag{5.72}$$

where $V_G^f$ and $V_S^f$ are row vectors, that we report in Table 5.1. Their interpretation is clear for final states with gauge bosons: the first vector corresponds to the emission of transverse bosons, whereas the second vector corresponds to the emission of longitudinal bosons, which -by virtue of the Equivalence Theorem- is equivalent to the emission of Goldstone bosons in the high-mass regime.

If we add all the contribution of the two-body final states, we find again the same results of Eq. (5.53) and Eq. (5.57), which were derived using path-integral methods. That is, we find $\Gamma_{\text{Gauge}} + \Gamma_{\text{Scalars}} = \sum_f \Gamma_f$, for the states $f$ of Table 5.1.

| Final State $f$ | $V_G^f$ | $V_S^f$ |
|:---:|:---:|:---:|
| $W^+W^-$ | $\left( \frac{g^2}{2}, \frac{g^2}{2}, \frac{g^2}{\sqrt{2}} \right)$ | $\left( \frac{\lambda_3}{\sqrt{2}}, \frac{\lambda_3}{\sqrt{2}}, \lambda_3 + \lambda_4 \right)$ |
| $ZZ$ | $\left( \frac{g^2}{2\sqrt{2}c_W^2}, \frac{g^2}{2\sqrt{2}c_W^2}, \frac{g^2(1-2c_W^2)^2}{2c_W^2} \right)$ | $\left( \frac{-\lambda_3-\lambda_4+\lambda_5}{2}, \frac{-\lambda_3-\lambda_4-\lambda_5}{2}, -\frac{\lambda_3}{\sqrt{2}} \right)$ |
| $\gamma\gamma$ | $(0, 0, 2e^2)$ | $(0, 0, 0)$ |
| $\gamma Z$ | $\left( 0, 0, \sqrt{2}(1 - 2c_W^2)\frac{ge}{c_W} \right)$ | $(0, 0, 0)$ |
| $hh$ | $(0, 0, 0)$ | $\left( \frac{-\lambda_3-\lambda_4-\lambda_5}{2}, \frac{-\lambda_3-\lambda_4+\lambda_5}{2}, -\frac{\lambda_3}{\sqrt{2}} \right)$ |

Table 5.1: Row vectors $V_G^f$ and $V_S^f$ for calculating $\Gamma_f$ using Eq. (5.72) for each two-body final state. For the case of gauge bosons, they correspond to the emission of transversely and longitudinally polarized particles, respectively.

**Three-body final state processes and VIB**

This method is particularly useful for calculating the contribution from three-body final states. However, in this case the expression of $\Gamma_f$ is more complicated. In this work, we only consider the process $H^0 H^0 \to W^+ W^- \gamma$, since it is the only one playing an important role, specially for calculating the gamma-ray spectra. We follow section 4.2, in particular Eqs. (4.17),(4.18), (4.19) and (4.20), to manipulate the required three-body phase integration of Eq. (5.71). In this way, the matrix $\Gamma$ - differential in the variable $x$- can be written as

$$\frac{d\left(\Gamma_{W^+W^-\gamma}\right)_{ii',jj'}}{dx} = \frac{N_{ii'} N_{jj'}}{128\pi^3} \int_{x_{+\min}}^{x_{+\max}} \mathcal{M}\left(ii' \to W^+ W^- \gamma\right) \mathcal{M}\left(jj' \to W^+ W^- \gamma\right)^* dx_+. \quad (5.73)$$

Although $\mu$ is very small in the high-mass regime of the IDM, we can not neglect it in the last equation because it regularizes infrared divergences in the different VIB processes. Analytical expressions for the previous equation can be obtained, but they are in general very long and because of this we do not report them here.

## 5.6 The Sommerfeld Effect

Now we show how to include the non-perturbative effects in cross section calculations. Using the path integral of Eq. (5.68), it is possible to prove that the s-wave annihilation cross section can be calculated using the following algorithm [22]:

1. If $v$ is the relative velocity of the initial state particles, the differential equation

$$g''(r) + M_{H^0}\left(\frac{1}{4} M_{H^0} v^2 \mathbb{1} - V(r)\right) g(r) = 0 \quad (5.74)$$

for the $3 \times 3$ matrix $g(r)$ is solved for two boundary conditions [2]. At the origin

$$g(0) \;=\; \mathbb{1}\,, \quad (5.75)$$

whereas for large values of $r$, the solution describes the states $H^0 H^0$, $A^0 A^0$ and $H^- H^+$ according to the mass splitting:

- If the mass splitting $\delta m_{ii',ii'}$ associated to the inert pair $ii'$ is smaller than the initial kinetic energy $M_{H^0} v^2/4$, then there is enough energy to produce on-shell states of the corresponding pair, and therefore the matrix elements $g_{ii',jj'}(r)$ at infinity behave as an out-going wave, with momentum given according to Eq. (5.74) by

$$p_{ii'} = \sqrt{M_{H^0}\left(\frac{1}{4} M_{H^0} v^2 - V_{ii',ii'}(\infty)\right)} = \sqrt{M_{H^0}\left(\frac{1}{4} M_{H^0} v^2 - 2\,\delta m_{ii',ii'}\right)} \quad (5.76)$$

---

[2]Other boundary conditions have been considered in the literature (see, *e.g.*, [25, 27]). Moreover, in [27] it was proven that under certain circumstances, other choices for boundary conditions are equivalent to the prescription described in the present work.

The corresponding boundary condition at infinity is

$$\frac{dg_{ii',jj'}(\infty)}{dr} = i\, p_{ii'}\, g_{ii',jj'}(\infty)\,. \tag{5.77}$$

- In the opposite case, that is if $\delta m_{ii',ii'} > M_{H^0}v^2/4$, there is not enough energy to produce on-shell states of the corresponding pair, and therefore the matrix elements $g_{ii',jj'}(r)$ decays exponentially at infinity. Hence

$$g_{ii',jj'}(\infty) = 0\,. \tag{5.78}$$

2. Once the solution is obtained, the oscillating phases of $g(r)$ at large values of $r$ are factorized by writing it as

$$g(r) \to e^{ir\sqrt{M_{H^0}\left(\frac{1}{4}M_{H^0}v^2\mathbb{1}-2\,\delta m\right)}}d\,. \tag{5.79}$$

3. Subsequently, the s-wave cross section for the annihilation of the pair $(i,i')$ into a final state $f$ is calculated by means of the equation

$$\sigma v\,(ii' \to f)\Big|_{s-wave} = \frac{1}{N_{ii'}^2}(d\,\Gamma_f\,d^\dagger)_{ii',ii'}\,. \tag{5.80}$$

Notice that $d = \mathbb{1}$ when the potential in Eq. (5.74) is negligible, and therefore Eqs. (5.71) and (5.80) reduce to the standard expressions for calculating the cross section in the s-wave limit.

We are particularly interested in dark matter annihilation, in that case Eq. (5.80) can be cast as

$$\sigma v\,(H^0 H^0 \to f)\Big|_{s-wave} = \frac{1}{4M_{H^0}^2} \int \left(\prod_{a\in f}\frac{d^3q_a}{(2\pi)^3 2E_a}\right)(2\pi)^4\delta^4\left(p_{H^0} + p'_{H^0} - \sum_{a\in f}q_a\right)$$

$$\cdot\left|d_{11}\,\mathcal{M}\left(H^0 H^0 \to f\right) + d_{12}\,\mathcal{M}\left(A^0 A^0 \to f\right) + \sqrt{2}d_{13}\,\mathcal{M}\left(H^+ H^- \to f\right)\right|^2\,, \tag{5.81}$$

where $f$ here stands for any final state of light particles. The quantities $d_{11}$, $d_{12}$ and $d_{13}$ are therefore interpreted as non-perturbative enhancement factors that account for the long range interactions between the annihilating dark matter particles due to the exchange of gauge and Higgs bosons in the non-relativistic limit.

As an example, we show in Fig. 5.5 the absolute value of $d_{11}$, $d_{12}$ and $d_{13}$ as a function of the dark matter mass, for the case in which all the quartic couplings vanish. Observe that including these factors in the calculation is irrelevant for masses below approximately 2 TeV. However, once we approach higher values for the dark matter mass, the enhancement factors dramatically affect the annihilation cross sections, as shown in Eq. (5.81). Furthermore, we find a resonant behavior, in agreement with what was found in [22] for neutralino dark matter.
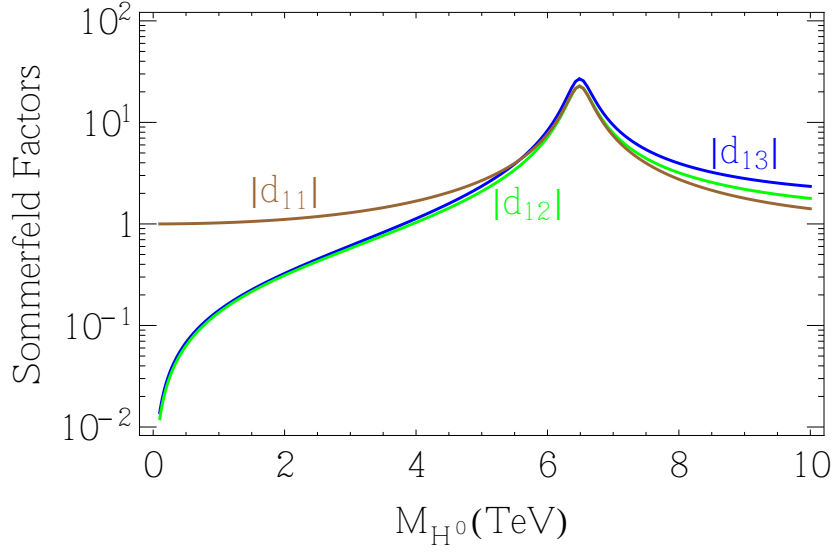
Figure 5.5: Absolute value of the Sommerfeld enhancement factors $d_{11}, d_{12}$ and $d_{13}$ as a function of the dark matter mass when all the quartic couplings vanish.
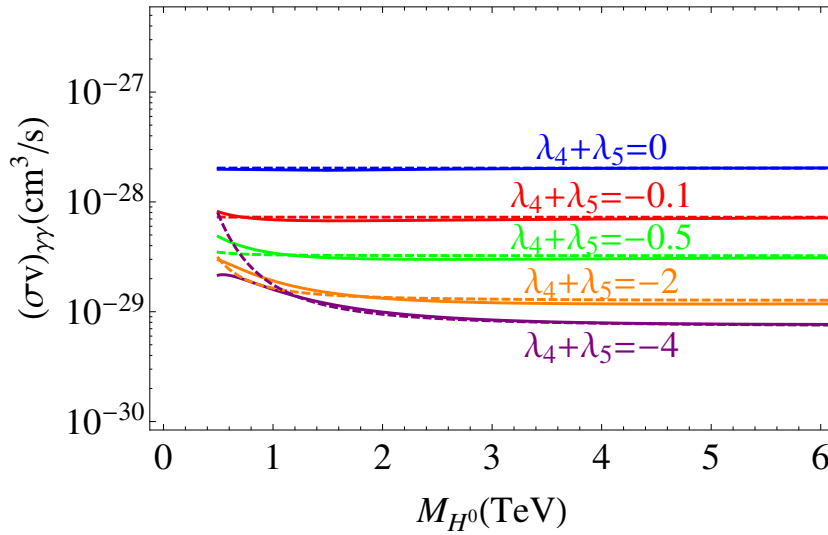


Figure 5.6: Cross section for the process $H^0 H^0 \to \gamma\gamma$ according to the one-loop calculation (dashed line) and according to the Born approximation described in Eq. (5.92) (continuous line).

**Annihilation into $\gamma\gamma$ and $\gamma Z$**     According to Table 5.1,

$$\Gamma_{\gamma\gamma} = \frac{2\pi\alpha^2}{M_{H^0}^2} \begin{pmatrix} 0 & 0 & 0 \\ 0 & 0 & 0 \\ 0 & 0 & 1 \end{pmatrix} , \qquad \Gamma_{\gamma Z} = \frac{\pi\alpha\alpha_2(1 - 2c_W^2)^2}{M_{H^0}^2 c_W^2} \begin{pmatrix} 0 & 0 & 0 \\ 0 & 0 & 0 \\ 0 & 0 & 1 \end{pmatrix} , \tag{5.82}$$

using Eq. (5.80) we then find that

$$\sigma v \left( H^0 H^0 \to \gamma\gamma \right) = \frac{4\pi\alpha^2 |d_{13}|^2}{M_{H^0}^2}, \qquad \sigma v \left( H^0 H^0 \to \gamma Z \right) = \frac{2\pi\alpha\alpha_2(1 - 2c_W^2)^2 |d_{13}|^2}{M_{H^0}^2 c_W^2}. \tag{5.83}$$

In [22] it was shown that for very high masses, these cross sections do not violate perturbative unitarity, in contrast to the one-loop results of chapter 4. This implies that the cross sections scale like $1/M_{H^0}^2$ for large dark matter masses.

## 5.7 The Born Approximation as the One-loop Result

In this section we study under which circumstances the one-loop calculation of section 4.1 matches the results of Eq. (5.83), which are obtained using the non-relativistic approach described previously. In order to do that, notice that in any one-loop calculation the interaction between the particles is treated perturbatively and corresponds to the first order in the expansion. We thus show that the calculation of section 4.1 matches the results obtained with Eq. (5.83) when one solves Eq. (5.74) by performing a perturbative expansion on the potential.

**Details of the Born Expansion**

The differential equation (5.74) for the Sommerfeld enhancement can be cast as

$$\frac{d^2g}{dr^2} + k^2 g(r) = M_{H^0} V(r) g(r) \qquad \text{with} \qquad k = \frac{1}{2} M_{H^0} v. \tag{5.84}$$

A formal solution of this equation is

$$g(r) = e^{ikr} g_0 + e^{-ikr} g_0' + \int_0^\infty dr' \, h(r - r') M_{H^0} V(r') g(r') , \tag{5.85}$$

where $h(r)$ is a Green's function of the harmonic oscillator

$$\frac{d^2h}{dr^2} + k^2 h(r) = \delta(r). \tag{5.86}$$

If the kinetic energy is smaller than the mass splitting, the matrix $g(r)$ admits only *out-going* waves for large r. In that case $g_0' = 0$ in Eq. (5.85). Similarly, the only Green's function $h(r)$ in agreement with this boundary condition is

$$h(r) = \frac{1}{2ik} \left( e^{ikr}\theta(r) + e^{-ikr}\theta(-r) \right), \tag{5.87}$$

and consequently the solution (5.85) is

$$g(r) = e^{ikr} g_0 + \frac{M_{H^0}}{2ik} \int_0^\infty dr \left( e^{ik(r-r')}\theta(r-r') + e^{-ik(r-r')}\theta(r'-r) \right) V(r')g(r'). \qquad (5.88)$$

If the potential is small enough, the previous equation can be solved by expanding in the potential. The first term of that expansion -the Born approximation- is

$$g(r) = \left( e^{ikr} + \frac{M_{H^0}}{2ik} \int_0^\infty dr \left( e^{ik(r-r')}\theta(r-r') + e^{-ik(r-r')}\theta(r'-r) \right) V(r')e^{ikr'} \right) g_0. \qquad (5.89)$$

After applying the boundary condition $g(0) = \mathbb{1}$ and factorizing out the oscillating phase at $r \to \infty$, one finds

$$d = \mathbb{1} - \frac{M_{H^0}}{k} \int_0^\infty dr' \sin(kr')V(r')e^{ikr'} , \qquad (5.90)$$

which gives for the 31 component

$$d_{13}|_{\text{Born Approx.}} = -\frac{1}{2\sqrt{2}} \left( \frac{M_{H^0}}{M_W + \sqrt{2M_{H^0}(M_{H^+} - M_{H^0})}} \right) \left( \alpha_2 + \frac{v_h^2(\lambda_4 + \lambda_5)^2}{16\pi M_{H^0}^2} \right) . \qquad (5.91)$$

**Annihilation into Photons under the Born Approximation**

Eqs. (5.91) and (5.83) implies then that

$$\sigma v(H^0 H^0 \to \gamma\gamma)|_{\text{Born Approx.}} = \frac{\pi\alpha^2}{2} \left( \frac{\alpha_2 + \frac{v_h^2(\lambda_4+\lambda_5)^2}{16\pi M_{H^0}^2}}{M_W + \sqrt{2M_{H^0}(M_{H^+} - M_{H^0})}} \right)^2 . \qquad (5.92)$$

In Fig. 5.6 we plot this cross section for different quartic couplings (continuous lines) and compare it with the one-loop calculation of section 4.1 (dashed lines). The agreement is very good, specially for masses in TeV range.

In general, the potential matrix is not small and can not be treated perturbatively. This happens when the exchange of gauge or Higgs bosons between the initial state particles has a significant effect. In that case Eq. (5.74) must be solved numerically in order to obtain the enhancement factors.

# Chapter 6

# Gamma-Ray Spectral Features from the IDM

In this chapter we calculate limits on the IDM, coming from indirect dark matter experiments with gamma-rays. In order to do that, we include the Sommerfeld Effect.

## 6.1 Scan over the Parameter Space

In order to study gamma-ray spectra in the high-mass regime of the IDM, we perform a scan over the five dimensional parameter space of the dark matter sector. More specifically, we let $M_{H^0}$ vary in between 500 GeV and 6 TeV, and the quartic couplings in the range $|\lambda_i| \lesssim 3$. We do not take larger masses, because in general they lead to thermally-produced dark matter with quartic couplings larger than three or more, and we do not consider such values in order to ensure perturbativity. In addition, for every point we impose vacuum stability by requiring that the quartic couplings satisfy Eq. (3.11). For each of the points we then solve numerically the Boltzmann equations for the relic abundance by means of micrOMEGAs 3.1 [79] and select only those points for which the result is in agreement within $3\sigma$ with the observed value $\Omega_{\text{DM}}h^2 = 0.1199 \pm 0.0027$.

Subsequently, for each point of our scan we numerically solve Eq. (5.74) and calculate the enhancement factors $d_{11}, d_{12}$ and $d_{13}$, assuming a dark matter relative velocity of $v = 10^{-3}$. For the points of the scan we calculate the total annihilation cross section by adding the contribution from the $2 \to 2$ annihilation channels, $H^0 H^0 \to W^+ W^-, Z^0 Z^0$ and $hh$ with (without) Sommerfeld enhancement and show the results in Fig. 6.1 in orange (yellow). They are safely below the limits on the cross section derived in [133] from the PAMELA data on the cosmic antiproton-to-proton fraction [134] assuming 100% branching fraction into $WW$ and $hh$. We also show the limits [135] on the total annihilation cross section coming from gamma-ray searches performed by the HESS collaboration, assuming a NFW profile. We see that some of the points of the scan are excluded by this limit.

In order to assess the effect of the Sommerfeld enhancement, for each point of the scan we calculate the ratio of the total enhanced cross section to the unenhanced cross section. The results are shown in Fig. 6.2. We find that Sommerfeld effect is not negligible.
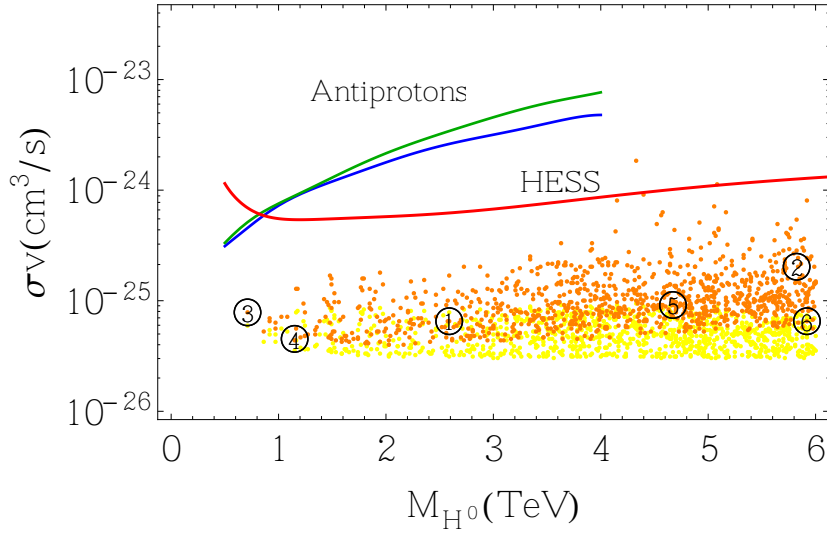
Figure 6.1: Total annihilation cross section for the points of the scan. The orange points take into account the Sommerfeld enhancement, whereas the yellow ones do not. We show the limits from antiprotons assuming 100% branching fraction into $WW$ (blue line) or $hh$ (green line) [133]. We also show the limits [135] on the total annihilation cross section coming from gamma-ray searches perfomed by the HESS collaboration (red Line). In addition, we display the benchmark points of Table 6.1.
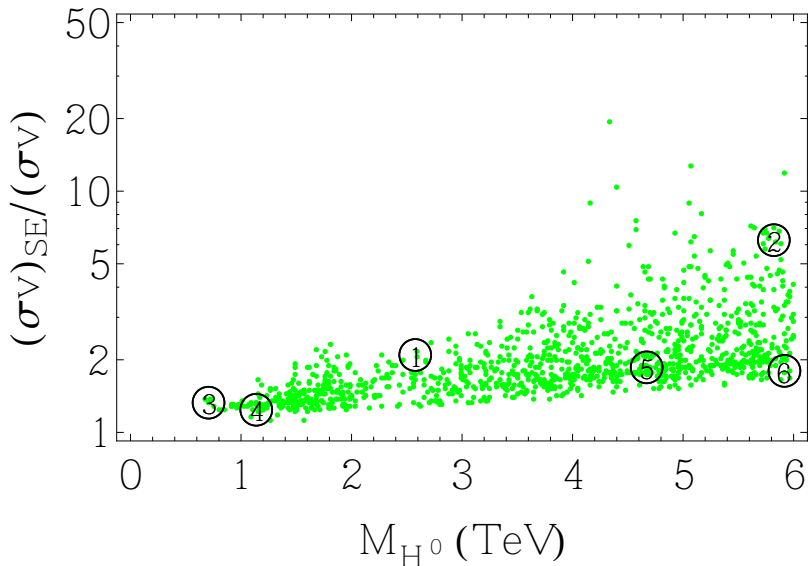


Figure 6.2: Impact of the Sommerfeld enhancement on the total annihilation cross section for the points of the scan. We also show the benchmark points of Table 6.1.

| Spectrum | Benchmarks | |
|---|---|---|
| Dominated by $\gamma$ lines | **BMP 1:** $M_{H^0} = 2.59$ TeV $\rho = 125.6$ $\kappa = 0.5$ <br><br> $\lambda_3 = -0.5$ $\lambda_4 = 1.05$ $\lambda_5 = -1.06$ | **BMP 2:** $M_{H^0} = 5.84$ TeV $\rho = 78.5$ $\kappa = 0.5$ <br><br> $\lambda_3 = -0.86$ $\lambda_4 = 2.46$ $\lambda_5 = -2.47$ |
| Dominated by VIB | **BMP 3:** $M_{H^0} = 0.71$ TeV $\rho = 46.9$ $\kappa = 0.9$ <br><br> $\lambda_3 = -0.23$ $\lambda_4 = 0.1$ $\lambda_5 = -0.15$ | **BMP 4:** $M_{H^0} = 1.15$ TeV $\rho = 43.9$ $\kappa = 2.3$ <br><br> $\lambda_3 = 0.23$ $\lambda_4 = -0.54$ $\lambda_5 = -0.31$ |
| Dominated by the continuum | **BMP 5:** $M_{H^0} = 4.68$ TeV $\rho = 10.9$ $\kappa = 4.7$ <br><br> $\lambda_3 = 2.9$ $\lambda_4 = -2.47$ $\lambda_5 = -0.79$ | **BMP 6:** $M_{H^0} = 5.92$ TeV $\rho = 36.5$ $\kappa = 1.1$ <br><br> $\lambda_3 = 0.53$ $\lambda_4 = 1.25$ $\lambda_5 = -2.73$ |

Table 6.1: Gamma-ray differential cross sections (black) for some benchmark points. The contributions of the VIB, the soft part, and the $\gamma\gamma$ and $\gamma Z$ monochromatic lines are in blue, green, magenta and pink, respectively. The spectra have been convoluted with a Gaussian detector response characterized by a standard deviation $\sigma(E) = 0.1E$. The dashed line is the spectra with no Sommerfeld enhancement.

In the IDM, the gamma-ray flux (2.15) can be cast as

$$\frac{d\Phi_\gamma}{dE_\gamma} = \frac{1}{8\pi} \left( \frac{1}{\Delta\Omega} \int_{\Delta\Omega} J d\Omega \right) \left( \frac{\sigma v}{M_{H^0}^3} \sum_f B_f \frac{dN^f}{dx} \right), \tag{6.1}$$

where we used $x = E_\gamma / M_{H^0}$ and the fact that all the processes proceed via s-waves which imply that we can safely take $\langle \sigma v \rangle = \sigma v$. In addition, the flux has different contributions. On first place, a soft part consisting on secondary photons from the decay and fragmentation of the gauge and Higgs bosons that are produced in dark matter annihilations. We calculate this contribution using PYTHIA 6.4 [136]. Secondly, from the monochromatic photons produced in the processes $H^0 H^0 \to \gamma\gamma$ and $H^0 H^0 \to \gamma Z$. And lastly, from the VIB photons. As a result we have

$$
\begin{aligned}
\sum_f B_f \frac{dN^f}{dx} &= \frac{1}{\sigma v} \left[ \frac{d(\sigma v)_{WW}^{\text{sec}}}{dx} + \frac{d(\sigma v)_{ZZ}^{\text{sec}}}{dx} + \frac{d(\sigma v)_{hh}^{\text{sec}}}{dx} \right. \\
&+ \left. 2(\sigma v)_{\gamma\gamma} \delta(x-1) + (\sigma v)_{\gamma Z} \delta\left( x - 1 + \frac{M_Z^2}{4M_{H^0}^2} \right) + \frac{d(\sigma v)_{WW\gamma}}{dx} \right].
\end{aligned} \tag{6.2}
$$

In this expression we include the Sommerfeld enhanced formulas of chapter 5. In order to illustrate each contribution, we show in Table 6.1 six benchmarks from the scan, and their corresponding gamma-ray differential cross sections. The contributions of the VIB, the soft part, and the $\gamma\gamma$ and $\gamma Z$ monochromatic lines are in blue, green, magenta and pink, respectively. The spectra have been convoluted with a Gaussian detector response characterized by a standard deviation $\sigma(E) = 0.1E$. We also show the effect of not including the Sommerfeld enhancement as a black dashed line. The six points were chosen following the next criteria: two points where the lines dominate, two points where the VIB dominates and two where the soft part is more significant. Also, in order to make the spectral features more noticeable and to establish gamma-ray limits, we multiply the differential cross sections by $x^{2.7}$.
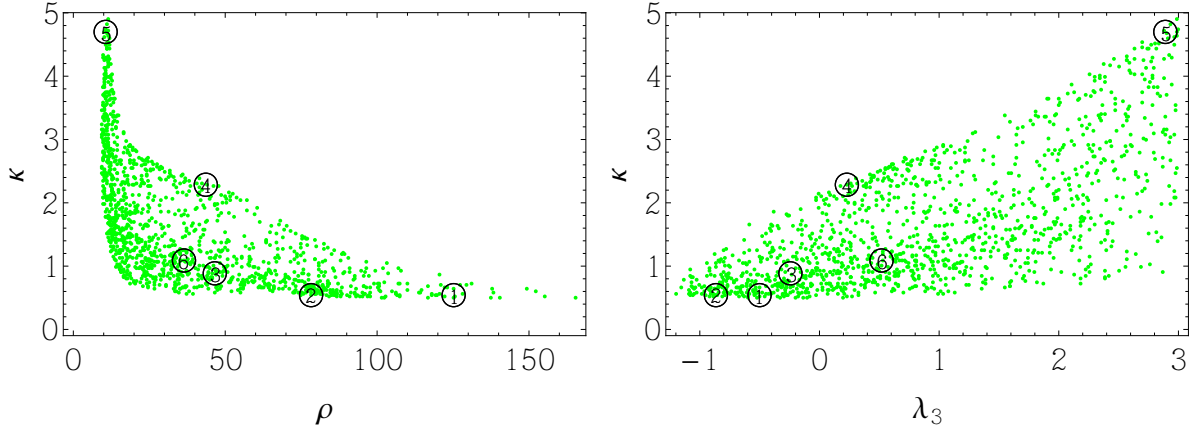


Figure 6.3: Interplay between the parameters $\rho$ and $\kappa$ from Eq. (6.3). See the text for details.

## 6.2 Monochromatic Lines and VIB

The relative importance of the VIB signature and the monochromatic lines can be quantified by introducing the following two quantities

$$\kappa = \frac{\int_{0.8}^{1-4\mu} \frac{d(\sigma v)_{WW\gamma}}{dx} dx}{2(\sigma v)_{\gamma\gamma} + (\sigma v)_{\gamma Z}}, \qquad \rho = \frac{2(\sigma v)_{\gamma\gamma} + (\sigma v)_{\gamma Z} + \int_{0.8}^{1-4\mu} \frac{d(\sigma v)_{WW\gamma}}{dx} dx}{\int_{0.8}^{1-4\mu} \left( \frac{d(\sigma v)_{WW}^{\text{sec}}}{dx} + \frac{d(\sigma v)_{ZZ}^{\text{sec}}}{dx} + \frac{d(\sigma v)_{hh}^{\text{sec}}}{dx} \right) dx} . \tag{6.3}$$

Similar variables were also used for analyzing spectral features in dark matter models of heavy neutralinos [105]. We expect the VIB signature to dominate over the monochromatic lines for large values of $\kappa$. Similarly, we expect the combination of the VIB spectrum and the monochromatic lines to dominate over the soft gamma-ray spectra for large values of $\rho$.

In order to study the relation between these two variables precisely we calculate them for the points of the scan. The results are shown in the left panel of Fig. 6.3. From this plot, we can conclude that if the VIB contribution is much greater than the monochromatic lines - for instance for values of $\kappa$ larger than 3- then the associated spectral feature is lost within the soft part of the spectrum due to the low values of $\rho$. An example of this is benchmark 5. On the other hand, when the combined spectral feature stands out of the spectrum, the monochromatic lines are at least as significant as the VIB. Nonetheless, this does not mean that the latter can be neglected, in fact, as it is apparent from the plot, in most cases the VIB and the monochromatic lines are of the same order of magnitude.

As shown in section 4.2, the internal bresmmstrahlung spectrum is composed of a gauge part -independent of the quartic couplings with a sharp spectral feature- and a featureless quartic piece proportional to the coupling $\lambda_3$. The former is associated to transverse $W$ bosons, whereas the latter to the longitudinal ones. A possible explanation for the fact that large values of $\kappa$ correspond to low values of $\rho$ is that, for these cases, the VIB signature dominates over the monochromatic lines because the quartic piece is much greater than both the gauge part and the lines. Accordingly, there should be no spectral feature in the spectrum. We corroborate this hypothesis in the right panel of Fig. 6.3, which shows that large values of $\kappa$ are obtained only when $\lambda_3$ is correspondingly large, and consequently, when the quartic piece of the VIB spectrum dominates over the gauge part, erasing the spectral feature.

## 6.3 H.E.S.S. Limits on the IDM

We now calculate the gamma-ray flux given by Eq. (6.1) corresponding to the first four benchmark models of Table 6.1. We do not consider benchmarks 4 and 5 because their overall spectral feature does not stand out over the soft part. We choose for our study NFW profile [88,89] (see section 2.3.2). We will compare our predicted flux to the limits recently derived by the H.E.S.S. collaboration from a search for line-like gamma-ray features in the central part of the Milky Way halo with energies between $\sim 500$ GeV and $\sim 25$ TeV [137], which adopts a complicated search region with a $J$-factor given $J = 6.4 \times 10^{24}$ GeV$^2$ cm$^{-5}$ for the NFW profile [135].
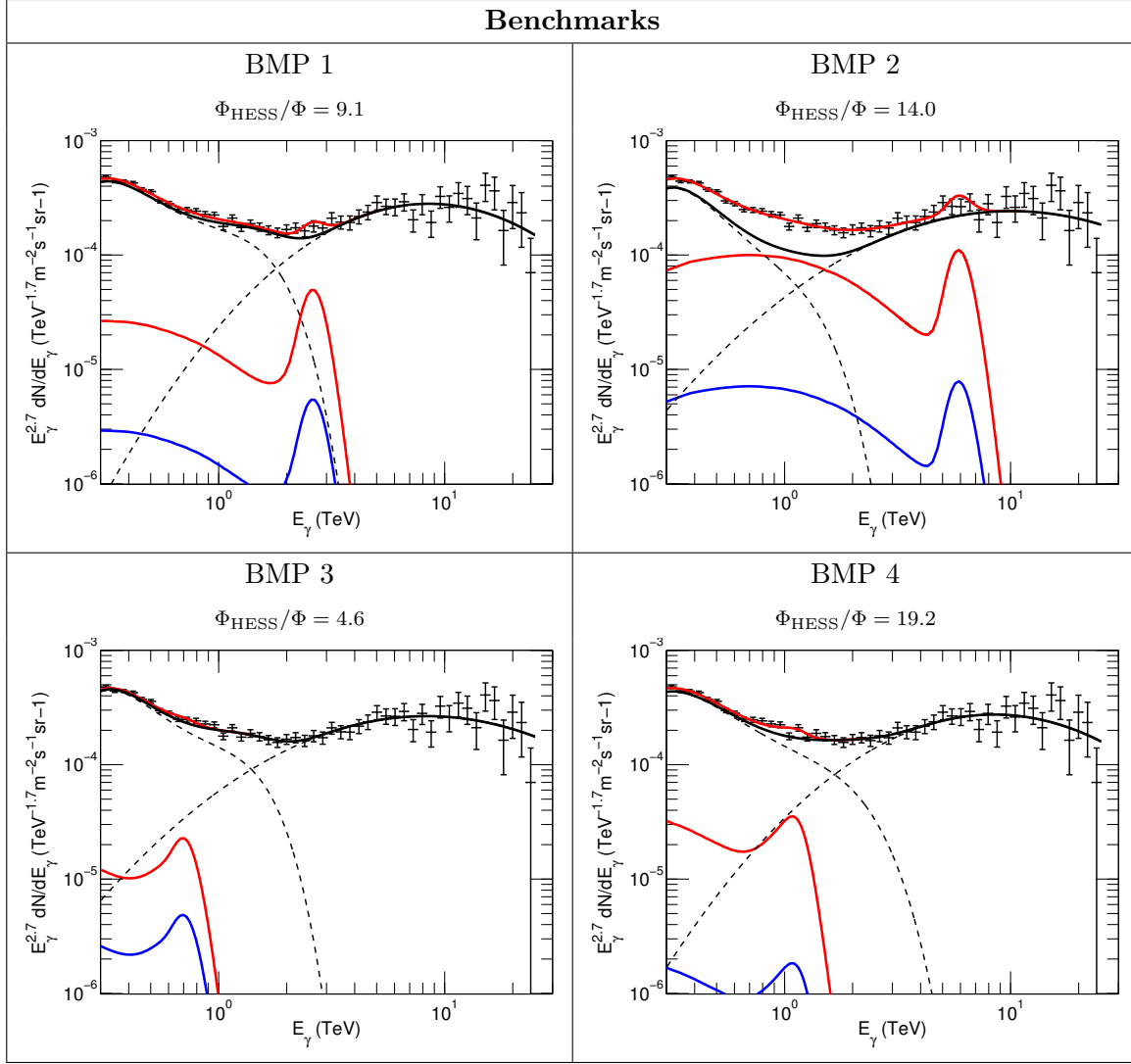
Table 6.2: H.E.S.S. limits on the benchmarks of Table 6.1. See text for details.

The predicted flux for each benchmark is shown as a blue curve in Table 6.2. The gamma-ray data measured by the collaboration with the respective error bars are also shown. In order to derive limits, we parametrize and fit the background as it was done in [137] and show it in black. Finally in red (upper lines) we show the total spectrum that would be excluded at a 95 % C.L. if the annihilation signal is multiplied by the factor that is shown in the upper part of the plots and that we call $\Phi_{\text{HESS}}/\Phi$. We also show in red (lower lines) the corresponding signal when multiplied by that factor. We add that for doing this study the $\chi^2$ method was used.

As apparent from the table, present instruments are not sensitive enough to observe the spectral of the IDM, unless the annihilation signal is boosted by astrophysical or particle physics effects by a factor $\mathcal{O}(10)$. Future instruments, such as DAMPE [138], GAMMA-400 [139] or CTA [140] will, however, close in on the signals from the IDM.

It is important to contrast these limits with the corresponding limits from direct detection. We calculate the latter following [16, 66, 122] and then compare them with the current sensitivity of the LUX experiment [82] . We show the results in Table 6.3. We conclude that gamma-ray limits can do much better than direct detection experiments when the dark matter mass is large.

| BMP | $M$ (TeV) | $\Phi_{\mathrm{HESS}}/\Phi$ | $\sigma_{\mathrm{LUX}}/\sigma_{\mathrm{SI}}$ |
|---|---|---|---|
| 1 | 2.59 | 9.1 | 31.9 |
| 2 | 5.84 | 14.0 | 103.9 |
| 3 | 0.71 | 4.6 | 2.6 |
| 4 | 1.15 | 19.9 | 2.4 |

Table 6.3: Gamma-ray limits vs. spin independent direct detection limits.

# Part III

# Dark Matter Stability from a Spontaneously Broken Global Group

# Chapter 7

# Model II: Dark Matter from a Dirac Fermion

As conjectured in section 2.1, the stability of the dark matter is very likely due to the existence of a symmetry in the Lagrangian. The simplest symmetry that ensures the absolute stability of the dark matter particle is a discrete $Z_2$ symmetry, under which all the Standard Model particles are even while the dark matter particle is odd. The discrete symmetry in the Lagrangian could be imposed by hand or could arise as a remnant of the breaking of a global symmetry. In fact, suppose that the global symmetry is described by an $U(1)$ group and that a scalar field with charge 2 in units of the smallest $U(1)-$charge acquires a vacuum expectation value, then the global symmetry is spontaneously broken and a discrete $Z_2$ symmetry emerges in the Lagrangian. Moreover, all the fields with even and odd charges under the global group will acquire, after the spontaneous symmetry breaking, an even and odd discrete charge under the $Z_2$ transformation, respectively. Therefore, the lightest particle with odd charge is absolutely stable and a potential candidate for dark matter.

The spontaneous breaking of a global continuous symmetry, as is well known, gives rise to massless Goldstone bosons in the spectrum [31–33]. While the presence of Goldstone bosons is usually an unwanted feature in model building, it was recently argued by Weinberg [34] that the Goldstone boson that arises in this framework could contribute to energy density of th Universe. More specifically, if the Goldstone bosons are in thermal equilibrium with the Standard Model particles until the era of muon annihilation, their contribution to the effective number of neutrino species $N_{\text{eff}}$ would be 0.39, in remarkable agreement with the central value obtained in [35] from combining Planck data, WMAP9 polarization data and ground-based observations of high-$\ell$, which imply $N_{\text{eff}} = 3.36^{+0.68}_{-0.64}$ at 95% C.L.

In this chapter we introduce these ideas in a particular model and show -as opposed to the original claim- that the Goldstone bosons associated to the stability of dark matter particle play a crucial role in the dark matter production. We leave for chapter 9 the discussion of $N_{\text{eff}}$.

## 7.1 Description of the Model

We consider the model proposed in [34], where the Standard Model (SM) is extended by one complex scalar field $\phi$ and one Dirac fermion field $\psi$. The new fields are singlets under the SM gauge group and are charged under a global $U(1)_{\text{DM}}$ symmetry, namely: $U(1)_{\text{DM}}(\psi) = 1$ and

$U(1)_{\mathrm{DM}}(\phi) = 2$. Besides, all the SM fields transform trivially under the global symmetry. As a consequence, the dark sector interacts with the SM fermions only through the Higgs portal. The corresponding interaction Lagrangian reads:

$$
\begin{aligned}
\mathcal{L} \;=\;& (D_\mu \Phi)^\dagger (D^\mu \Phi) \,+\, \mu_\Phi^2 \, \Phi^\dagger \, \Phi \,-\, \lambda_\Phi \left( \Phi^\dagger \, \Phi \right)^2 \\
&+ \partial_\mu \phi^* \partial^\mu \phi \,+\, \mu_\phi^2 \, \phi^* \, \phi \,-\, \lambda_\phi \left( \phi^* \, \phi \right)^2 \,-\, \kappa \left( \Phi^\dagger \, \Phi \right) \left( \phi^* \, \phi \right) + \mathcal{L}_{\mathrm{DM}} \,,
\end{aligned}
\tag{7.1}
$$

where $D_\mu$ is the covariant derivative, $\Phi$ is the SM Higgs doublet and

$$
\mathcal{L}_{\mathrm{DM}} = i \overline{\psi} \gamma^\mu \partial_\mu \psi - M \overline{\psi} \psi - \left( \frac{f}{\sqrt{2}} \phi \overline{\psi} \psi^c + h.c. \right) \,,
\tag{7.2}
$$

with $\psi^c \equiv C \overline{\psi}^T$. In the following we discuss separately the scalar sector and the dark matter sector.

### 7.1.1 The Scalar Sector

Both the scalar field $\phi$ and the neutral component of the Higgs doublet acquire non-zero vacuum expectation values (vev), which spontaneously break the symmetry group $SU(3)_{\mathrm{c}} \times SU(2)_{\mathrm{W}} \times U(1)_{\mathrm{Y}} \times [U(1)_{\mathrm{DM}}] \to U(1)_{\mathrm{em}} \times Z_2$. In order to analyze the physical mass spectrum of the theory, we conveniently parametrize the scalar fields in Eq. (7.1) as: [1]

$$
\Phi = \begin{pmatrix} G^+ \\ \frac{v_h + \tilde{h} + iG^0}{\sqrt{2}} \end{pmatrix} \,, \qquad \phi = \frac{v_\phi + \tilde{\rho} + i\eta}{\sqrt{2}} \,,
\tag{7.3}
$$

where the SM Higgs vev is $v_h \simeq 246$ GeV. Then, from the minimization of the scalar potential in Eq. (7.1) we get the following tree-level relations between the parameters of the Lagrangian and the vacuum expectation values:

$$
\mu_\Phi^2 = \frac{1}{2} \left( 2 v_h^2 \lambda_\Phi \,+\, v_\phi^2 \kappa \right) \,, \qquad \mu_\phi^2 = \frac{1}{2} \left( 2 v_\phi^2 \lambda_\phi \,+\, v_h^2 \kappa \right) \,.
\tag{7.4}
$$

The neutral $CP$-odd component of the Higgs doublet, $G^0$, provides the longitudinal polarization of the $Z$ boson through the Brout-Englert-Higgs mechanism. On the other hand, the pseudo-scalar field $\eta$ corresponds to the Goldstone boson that arises from the spontaneous breaking of the global $U(1)_{\mathrm{DM}}$ symmetry. Therefore, the physical mass spectrum consists of two $CP$-even massive real scalars, denoted by $h$ and $\rho$, which are linear combinations of the interaction fields $\tilde{h}$ and $\tilde{\rho}$ in Eq. (7.3), and a $CP$-odd massless scalar $\eta$. The mass matrix of the $CP$-even scalars in the basis of interaction fields $(\tilde{h}, \tilde{\rho})$ reads

$$
\mathcal{M}_S = \begin{pmatrix} 2 \lambda_\Phi v_h^2 & \kappa \, v_h \, v_\phi \\ \kappa \, v_h \, v_\phi & 2 \lambda_\phi v_\phi^2 \end{pmatrix} \,,
\tag{7.5}
$$

---

[1]In contrast to [34], with this parametrization only renormalizable terms in the Lagrangian are necessary to analyze, at lowest order, the phenomenology of the dark sector.

where we have used Eq. (7.4). The mass eigenstates $h$ and $\rho$ are thus obtained by the basis transformation:

$$\begin{pmatrix} \tilde{h} \\ \tilde{\rho} \end{pmatrix} = R_S \begin{pmatrix} h \\ \rho \end{pmatrix}, \tag{7.6}$$

with

$$R_S \equiv \begin{pmatrix} \cos\theta & \sin\theta \\ -\sin\theta & \cos\theta \end{pmatrix} \quad \text{and} \quad \tan 2\theta = \frac{\kappa \, v_h \, v_\phi}{\lambda_\phi \, v_\phi^2 - \lambda_\Phi \, v_h^2}. \tag{7.7}$$

The masses of the physical states are:

$$m_h^2 = 2\lambda_\Phi v_h^2 \cos^2\theta + 2\lambda_\phi v_\phi^2 \sin^2\theta - \kappa\, v_h\, v_\phi \sin 2\theta, \tag{7.8}$$

$$m_\rho^2 = 2\lambda_\Phi v_h^2 \sin^2\theta + 2\lambda_\phi v_\phi^2 \cos^2\theta + \kappa\, v_h\, v_\phi \sin 2\theta. \tag{7.9}$$

In the following, we assume that the $CP$-even state $h$ corresponds to the Standard Model Higgs boson with $m_h = 125$ GeV. Notice that, after the electroweak symmetry breaking, the scalar sector can be described in terms of three independent unknown parameters, $m_\rho$, $v_\phi$ and $\theta$, as well as the mass and the vev of the Higgs. With this choice, the quartic couplings are unambiguously given by

$$\lambda_\Phi = \frac{m_h^2 \cos^2\theta + m_\rho^2 \sin^2\theta}{2v_h^2}, \qquad \lambda_\phi = \frac{m_h^2 \sin^2\theta + m_\rho^2 \cos^2\theta}{2v_\phi^2}, \tag{7.10}$$

$$\kappa = \frac{(m_\rho^2 - m_h^2)\sin 2\theta}{2\, v_h\, v_\phi}.$$

The stability of the scalar potential implies the condition $4\lambda_\Phi \lambda_\phi - \kappa^2 > 0$, which is automatically satisfied by the previous equations as long as $m_\rho^2 > 0$ and $m_h^2 > 0$.

### 7.1.2 The Dark Matter Sector

The coupling constant $f$ of the interaction between the Dirac field $\psi$ and the complex scalar $\phi$ in Eq. (7.2) is in general complex. However, this phase can be absorbed by a redefinition of the scalar field $\phi$. As a result, the Lagrangian Eq. (7.2) conserves $CP$ and both $P$ and $C$ separately. Besides, the Dirac field $\psi$ is no longer a mass eigenstate after $\Phi$ and $\phi$ acquire non-zero vacuum expectation values. Indeed, it splits into two new mass-eigenstates, which correspond to the Majorana fermions:

$$\psi_+ = \frac{\psi + \psi^c}{\sqrt{2}}, \qquad \psi_- = \frac{\psi - \psi^c}{\sqrt{2}i}, \tag{7.11}$$

which are $C$-even and $C$-odd respectively (see Appendix A). In terms of them, the Lagrangian can be cast as

$$\begin{aligned} \mathcal{L} = \ & \frac{1}{2}\left(i\overline{\psi_+}\gamma^\mu\partial_\mu\psi_+ + i\overline{\psi_-}\gamma^\mu\partial_\mu\psi_- - M_+\overline{\psi_+}\psi_+ - M_-\overline{\psi_-}\psi_-\right) \\ & -\frac{f}{2}\left((-\sin\theta\, h + \cos\theta\, \rho)(\overline{\psi_+}\psi_+ - \overline{\psi_-}\psi_-) + \eta\,(\overline{\psi_+}\psi_- + \overline{\psi_-}\psi_+)\right), \end{aligned} \tag{7.12}$$

with $M_{\pm} = |M \pm f v_{\phi}|$. Notice that this Lagrangian is invariant under the $Z_2$ transformation $\psi_{\pm} \to -\psi_{\pm}$, which is a remnant of the spontaneously broken $U(1)_{\mathrm{DM}}$ symmetry. As a result, the lightest Majorana fermion is stable and, consequently, a dark matter candidate. If the coupling constant $f$ is positive, the lightest Majorana fermion is $\psi_-$. Without loss of generality, we will assume that this is the case. Notice that the dark sector contains five unknown parameters, for example, $M_-$, $m_{\rho}$, $\lambda_{\phi}$, $\theta$ and $f$. Nevertheless, in some instances we will find convenient to express observables in terms of the following dimensionless quantities:

$$r = \frac{m_{\rho}}{M_-}, \qquad z = \frac{M_+}{M_-} . \tag{7.13}$$

In this scenario, not only the dark matter particle survives until today, but also the Goldstone boson. In fact, all other particles of the dark sector are unstable. On the one hand, $\psi_+$ decays into a dark matter particle and a Goldstone boson with a decay rate:

$$\Gamma(\psi_+ \to \psi_- \eta) = \frac{f^2 (M_+^2 - M_-^2)(M_+ + M_-)^2}{16\pi \, M_+^3} . \tag{7.14}$$

On the other hand, the scalar $\rho$ decays into $\psi^{\pm}$ pairs, two Goldstone bosons or SM particles. Decays into SM particles are negligible since the corresponding decay rate is proportional to $\sin^2 \theta$, which, as we will see in the next subsection, should be very small. Therefore the relevant decay widths read:

$$\Gamma(\rho \to \eta\, \eta) = \frac{m_{\rho}^3 \cos^2 \theta}{32\,\pi\, v_{\phi}^2}, \tag{7.15}$$

$$\Gamma(\rho \to \psi_{\pm}\psi_{\pm}) = \frac{f^2 \cos^2 \theta}{16\,\pi\, m_{\rho}^2} \left(m_{\rho}^2 - 4\, M_{\pm}^2\right)^{3/2} . \tag{7.16}$$

### 7.1.3 Constraints from Invisible Higgs Decays

The enlarged scalar and fermion sectors affect the SM Higgs decay channels. The new decay modes and the corresponding decay rates are:

$$\Gamma(h \to \eta\, \eta) = \frac{m_h^3 \sin^2 \theta}{32\,\pi\, v_{\phi}^2}, \tag{7.17}$$

$$\Gamma(h \to \rho\, \rho) = \frac{\left(m_h^2 + 2\, m_{\rho}^2\right)^2}{128\,\pi\, m_h^2\, v_h^2\, v_{\phi}^2} \sqrt{m_h^2 - 4 m_{\rho}^2}\, (v_h \cos\theta - v_{\phi} \sin\theta)^2 \sin^2 2\theta, \tag{7.18}$$

$$\Gamma(h \to \psi_{\pm}\psi_{\pm}) = \frac{f^2 \sin^2 \theta}{16\,\pi\, m_h^2} \left(m_h^2 - 4\, M_{\pm}^2\right)^{3/2} . \tag{7.19}$$

It is possible to constrain the value of the scalar mixing angle $\theta$ from the experimental upper bound on the Higgs boson invisible decay width. Indeed, neglecting for simplicity the $h$ decays into a pair of $\rho$ or $\psi_{\pm}$, the total decay width of $h$ takes the form:

$$\Gamma_h^{\mathrm{tot}} = \cos^2 \theta\, \Gamma_{\mathrm{Higgs}}^{\mathrm{SM}} + \Gamma(h \to \eta\, \eta) , \tag{7.20}$$

where $\Gamma_{\text{Higgs}}^{\text{SM}} \simeq 4$ MeV is the total decay width of the Higgs boson within the Standard Model for a Higgs boson mass of $125$ GeV. Therefore, from Eq. (7.20) it follows that

$$\Gamma\left(h \to \eta\,\eta\right) \; < \; \frac{B_{\text{inv}}\,\cos^2\theta}{1 - B_{\text{inv}}}\,\Gamma_{\text{Higgs}}^{\text{SM}}\,, \tag{7.21}$$

where $B_{\text{inv}} \simeq 20\%$ (see, *e.g.*, [141, 142]) is the conservative experimental upper limit on the invisible branching ratio of the Higgs boson. Thus, from the expression of the $h$ decay rate into two Goldstone bosons, Eq. (7.17), the following upper limit on $\tan\theta$ can be derived [34]:

$$|\tan\theta| < \sqrt{\frac{32\,\pi\,v_\phi^2\,\Gamma_{\text{Higgs}}^{\text{SM}}\,B_{\text{inv}}}{m_h^3\,(1 - B_{\text{inv}})}} \; \lesssim \; 2.2 \times 10^{-3}\left(\frac{v_\phi}{10\,\text{GeV}}\right) \approx 1.6 \times 10^{-5}\lambda_\phi^{-1/2}\left(\frac{m_\rho}{0.1\,\text{GeV}}\right),\tag{7.22}$$

where in the last expression it was replaced $v_\phi \approx m_\rho/\sqrt{2\,\lambda_\phi}$ at leading order in $\theta$.

Including the other two decay processes, Eqs. (7.18) and (7.19), when kinematically allowed, would reduce the upper bound derived in Eq. (7.22) by up to 5%. As we will see in section 7.3, stronger limits on the scalar mixing angle $\theta$ can be derived from dark matter direct detection experiments.

## 7.2 Dark Matter Relic Abundance

As discussed in section 2.2, the dark matter relic abundance is obtained by solving the Boltzmann equation

$$\frac{dn}{dt} + 3Hn = -\langle\sigma_{\text{eff}}v\rangle\left(n^2 - (n^{eq})^2\right),\tag{7.23}$$

where $n = n_+ + n_-$, with $n_\pm$ being the number densities of the (co)annihilating species $\psi_\pm$. The equilibrium densities are

$$n_\pm^{eq} = \frac{M_\pm^2 T}{2\pi^2}K_2\left(\frac{M_\pm}{T}\right),\tag{7.24}$$

where $K_n(x)$ is the modified Bessel function of the second kind of $n$th order. The effective thermal cross section is given by [78]

$$\langle\sigma_{\text{eff}}v\rangle \;\; = \;\; \sum_{i,j=\pm}\langle\sigma^{ij}v\rangle\frac{n_i^{eq}\,n_j^{eq}}{n^{eq}\,n^{eq}},\tag{7.25}$$

with

$$\langle\sigma^{ij}v\rangle = \frac{\int_{(M_i+M_j)^2}^{\infty}\frac{ds}{\sqrt{s}}K_1\left(\frac{\sqrt{s}}{T}\right)(s - (M_i + M_j)^2)(s - (M_i - M_j)^2)\sigma(ij \to all)}{8TM_i^2M_j^2K_2(\frac{M_i}{T})K_2(\frac{M_j}{T})}\,.\tag{7.26}$$

### 7.2.1 Scan Over the Parameter Space

In order to study the dark matter production mechanism in this model, we perform scans over the five dimensional parameter space. More specifically, $m_\rho$ and $v_\phi$ vary in the range 200 MeV and 1 TeV, while the dark matter mass, between 1 GeV and 1 TeV. Besides, $|\tan\theta|$ varies between zero and the upper limit set by the invisible decay width of the Higgs, given in Eq. (7.22), and $f$ is taken between $10^{-2}$ and $4\pi$. Lastly, for every point we require perturbativity by requiring that the quartic couplings determined by Eq. (7.10) are smaller than $4\pi$. For each of the points we then solve numerically the Boltzmann equation Eq. (7.23) by using micrOMEGAs 3.1 [79], working under an implementation of our model made with FeynRules [125], and select only those points for which the computed relic density is in agreement within $3\sigma$ with the observed value $\Omega_{\mathrm{DM}}h^2 = 0.1199 \pm 0.0027$.

The results of two different scans, with $m_\rho = 500$ MeV and 250 GeV, are reported in Figs. 7.1 and 7.2 respectively, where we show the relative contribution to the relic density of each annihilation channel. In the former, the dominant annihilation channel is always into a pair of $\rho$ scalars, when this is kinematically open, *i.e.* for $r = m_\rho/M_- < 1$. Conversely, the annihilation into Goldstone bosons dominates in the region $r > 1$. As shown in the upper panel, the coannihilation process $\psi_-\psi_+ \to \eta\rho$ is relevant only in the limit $z = M_+/M_- \sim 1$. For this region of the parameter space the annihilation of dark matter into the SM sector is always subdominant because either these channels are kinematically closed or the coupling to SM particles is very small. We show in Fig. 7.2 the corresponding plot for the case $m_\rho = 250$ GeV. In this case, due to the large scalar mass, annihilation channels into SM fermions and gauge bosons might not be neglected. In general, channels with SM particles in the final state contribute significantly to the dark matter relic density only under two circumstances: when the mixing angle $\theta$ is non-negligible, or when the dark matter annihilation proceeds via resonant s-channel exchange of $CP$-even scalars, that is either $\rho$ or $h$. This is manifest in Fig. 7.2, where the Higgs resonance takes place at $M_- = m_h/2 \approx 63$ GeV, while the one corresponding to $\rho$ at $M_- = m_\rho/2 \approx 125$ GeV.

**Limit $\theta \ll 1$**

In the following we focus in the limit $\theta \ll 1$, which is motivated by the measurements of the invisible Higgs decay width. In this regime, it is enough to consider the (co)annihilation channels with only $\eta$ or $\rho$ in the final state. In the first column of Table 7.1, we show these channels and their corresponding Feynman diagrams. Some comments are in order:

- Not every channel is always kinematically allowed. In particular, $\psi_-\psi_- \to \rho\rho$, $\psi_+\psi_+ \to \rho\rho$ and $\psi_-\psi_+ \to \eta\rho$ are only open if $m_\rho < M_-$, $m_\rho < M_+$ and $m_\rho < (M_- + M_+)$ respectively, or equivalently if $r < 1$, $r < z$ and $r < 1 + z$. Consequently, a threshold effect (see section 2.2.3) associated to the opening of the channel $\psi_-\psi_- \to \rho\rho$ always takes place when $r \sim 1$. Furthermore, if coannihilations are relevant – that is if $z \sim 1$– a threshold effect appears also when $r \sim 2$ and $r \sim 1$, because of the opening of the channels $\psi_+\psi_- \to \eta\rho$ and

$\psi_+\psi_+ \to \rho\rho$ respectively.

- $\psi_\pm\psi_\pm \to \eta\eta$ is always open and exhibits a resonant behavior when the energy of the initial state approaches the $\rho$ mass (see section 2.2.3). This effect is more dramatic when $m_\rho > 2M_-$ –or equivalently when $r > 2$– because in this case the integration region of Eq. (7.26) contains the resonance. However, this effect might also be present when $r > 1$ because a part of the resonance peak might still be within the integration region.

As a result, when $r \gtrsim 0.8$, a full integration of the Boltzmann equations is needed without any approximation. In Appendix B, we show the exact formulas for the cross sections which should be used in this case. Conversely, when $r \lesssim 0.8$, both resonance and threshold effects can be safely neglected and a reliable estimate of the cross section can be derived from the so-called instantaneous freeze-out approximation by expanding in partial waves, as explained in section 2.2. In Table 7.1 we report such expansion, that is, we show the cross sections for each process to leading order in the relative velocity $v$ of the particles of the initial state, assuming a vanishing mixing angle $\theta$.

## 7.2.2 Dark Matter (Co-)Annihilations and the $C$ and $CP$ Symmetries

As can be seen from Table 7.1, all the annihilation channels are p-wave suppressed. In contrast, the coannihilation channels proceed via s-waves and are the dominant annihilation process in the Early Universe if $z \sim 1$. This can be understood from $CP$ conservation.

To this end, we use the standard notation $S$, $L$ and $J$ for the spin, the orbital and the total angular momenta with a subscript $i$ or $f$ for the corresponding quantities of the initial or final state. Then, for the annihilation processes $\psi_-\psi_- \to \rho\rho$ and $\psi_-\psi_- \to \eta\eta$, the $CP$ eigenvalues of the initial and final states are $(-1)^{L_i+1}$ and $(-1)^{L_f}$, respectively (as shown in Table A.1). Thus $CP$-conservation implies that $|L_f - L_i|$ must be an odd number. In addition, since $\rho$ and $\eta$ are scalars, then $J_f = L_f$. If the s-wave were allowed, that is if $L_i = 0$ or $J_i = S_i$, then we could only have $S_i = 1$ and $L_i = 0$, which is impossible for a pair of Majorana fermions due to the Pauli exclusion principle (see Eq. (A.9)). The only possibility is therefore $L_i \geq 1$. On the other hand, for the coannihilation process $\psi_-\psi_+ \to \eta\rho$, the $CP$ eigenvalues of the initial and final states are $(-1)^{L_i}$ and $(-1)^{L_f+1}$. We again have $J_f = L_f$ and therefore $|J_i - L_i|$ must be an odd number. Consequently, the s-wave is allowed as long as $J_i = S_i = 1$. Finally, we remark that the process $\psi_-\psi_- \to \rho\eta$ does not exist, despite $CP$ is conserved for some values of $L_i$. In fact, in this process the initial state is $C$-even whereas the final state is $C$-odd, hence it is forbidden by $C$ conservation (as shown in Table A.1).
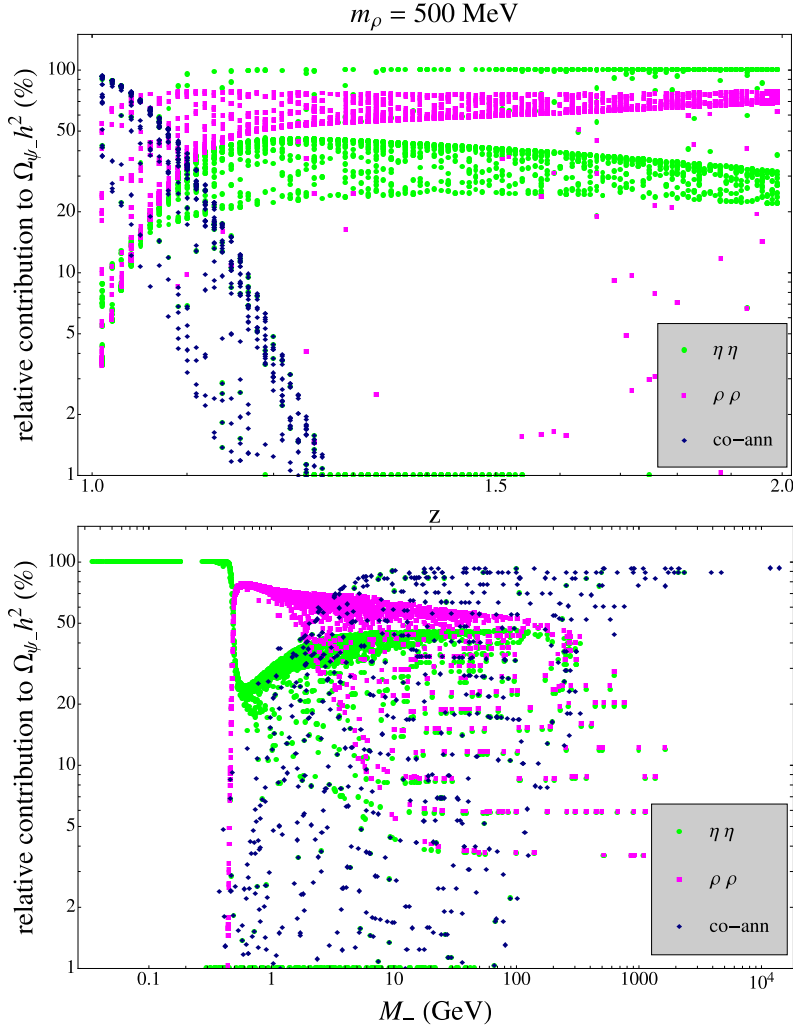
Figure 7.1: Relative contribution of each annihilation channel to the dark matter relic density versus the degeneracy parameter $z$ (upper panel) and the dark matter mass (lower panel) for $m_\rho = 500$ MeV. Only the the dark sector contributes to the relic density.
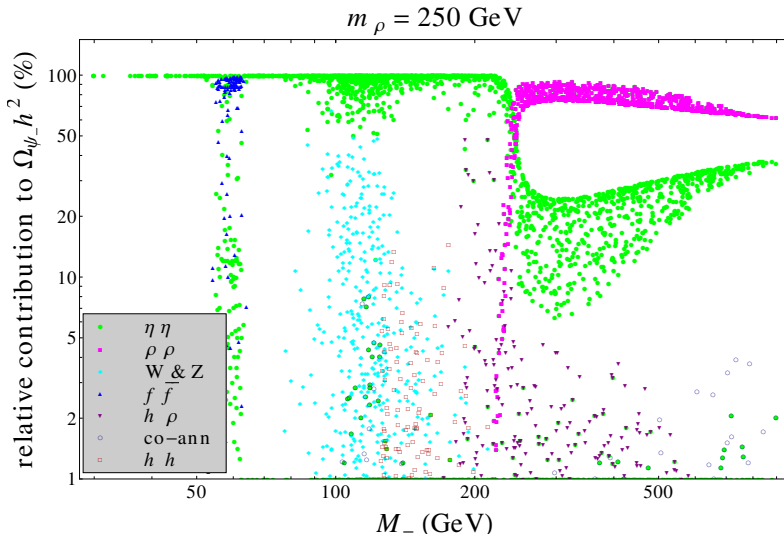


Figure 7.2: Relative contribution of each annihilation channel to the dark matter relic density versus the dark matter mass for $m_\rho = 250$ GeV.

| Process | Cross Section |
|---|---|
| Annihilation $\psi_-\psi_- \to \rho\rho$ <br><br> $\psi_- \quad \cdots\rho \quad \psi_- \quad \rho$ <br> $\quad \psi_- \quad \rho$ <br> $\psi_- \quad \cdots\rho \quad \psi_- \quad \rho$ | $\sigma v = \frac{f^4 v^2}{16\pi M_-^2} G_{\rho\rho}(r,z)$ <br><br> $G_{\rho\rho}(r,z) \equiv \sqrt{1-r^2}(27r^{12} + 24r^{10}z - 240r^{10}$ <br> $+8r^8 z^2 - 268r^8 z + 908r^8 - 96r^6 z^2 + 1152r^6 z$ <br> $-1920r^6 + 420r^4 z^2 - 2424r^4 z + 2436r^4$ <br> $-800r^2 z^2 + 2560r^2 z - 1760r^2 + 576z^2$ <br> $-1152z + 576)/(6(r^2-4)^2(r^2-2)^4(z-1)^2)$ |
| Annihilation $\psi_-\psi_- \to \eta\eta$ <br><br> $\psi_- \quad \cdots\eta \quad \psi_- \quad \eta$ <br> $\quad \psi_+ \quad \rho$ <br> $\psi_- \quad \cdots\eta \quad \psi_- \quad \eta$ | $\sigma v = \frac{f^4 v^2}{16\pi M_-^2} G_{\eta\eta}(r,z)$ <br><br> $G_{\eta\eta}(r,z) \equiv 2(3r^4 z^4 + 2r^4 z^3 + 5r^4 z^2 + 2r^4$ <br> $+12r^2 z^6 + 4r^2 z^5 + 8r^2 z^4 - 8r^2 z^3 - 12r^2 z^2$ <br> $+4r^2 z - 8r^2 + 12z^8 - 16z^5 - 8z^4 + 16z^2$ <br> $-16z + 12)/(3(r^2-4)^2(z-1)^2(z^2+1)^4)$ |
| Annihilation $\psi_+\psi_+ \to \rho\rho$ <br><br> $\psi_+ \quad \cdots\rho \quad \psi_+ \quad \rho$ <br> $\quad \psi_+ \quad \rho$ <br> $\psi_+ \quad \cdots\rho \quad \psi_+ \quad \rho$ | $\sigma v = \frac{f^4 v^2}{16\pi M_-^2 z^2} G_{\rho\rho}\left(\frac{r}{z}, \frac{1}{z}\right)$ |
| Annihilation $\psi_+\psi_+ \to \eta\eta$ <br><br> $\psi_+ \quad \cdots\eta \quad \psi_+ \quad \eta$ <br> $\quad \psi_- \quad \rho$ <br> $\psi_+ \quad \cdots\eta \quad \psi_+ \quad \eta$ | $\sigma v = \frac{f^4 v^2}{16\pi M_-^2 z^2} G_{\eta\eta}\left(\frac{r}{z}, \frac{1}{z}\right)$ |
| Coannihilation $\psi_-\psi_+ \to \rho\eta$ <br><br> $\psi_- \quad \cdots\eta \quad \psi_- \quad \eta$ <br> $\quad \psi_+ \quad \eta$ <br> $\psi_+ \quad \cdots\rho \quad \psi_+ \quad \rho$ <br><br> $\psi_- \quad \cdots\rho$ <br> $\quad \psi_-$ <br> $\psi_+ \quad \cdots\eta$ | $\sigma v = \frac{f^4}{16\pi M_-^2} G_{\rho\eta}(r,z)$ <br><br> $G_{\rho\eta}(r,z) \equiv ((z+1)^2 - r^2)^5/(4(r^2 z - z^2$ <br> $-2z-1)^2(r^2 - z^3 - 2z^2 - z)^2)$ |
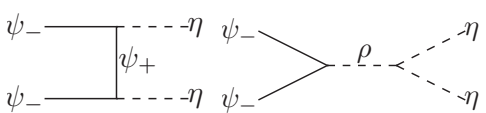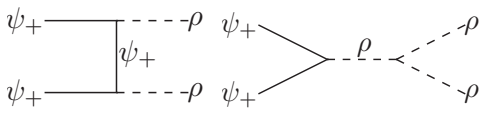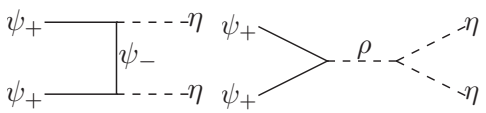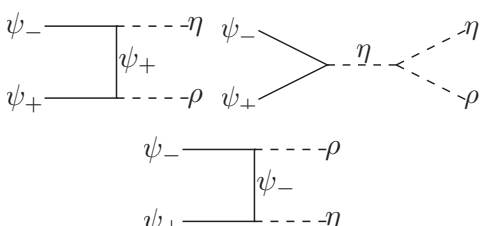
Table 7.1: (Co)annihilation channels of the dark matter particle and the corresponding cross sections to leading order in the relative velocity $v$ and the mixing angle $\theta$. The exact expressions are reported in Appendix B.

### 7.2.3 Dark Matter Coupling Constant in the Coannihilation Limit
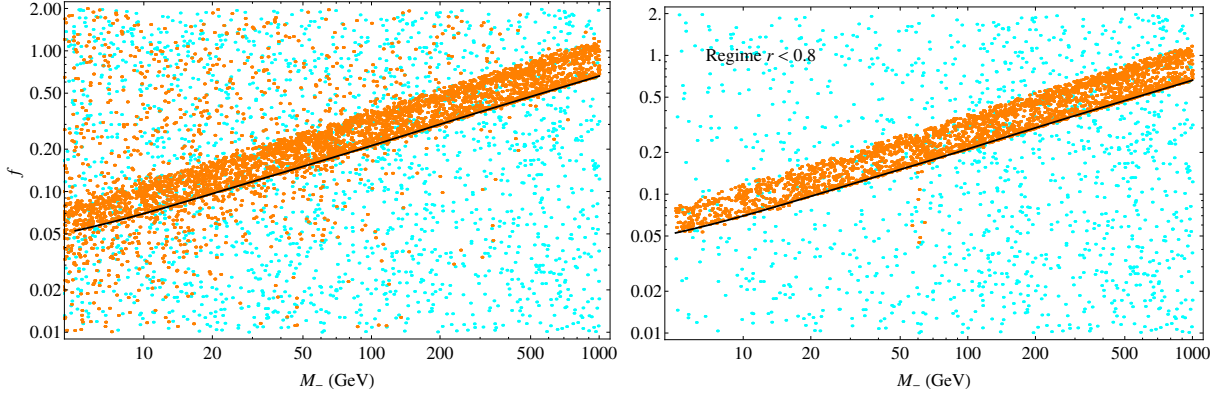


Figure 7.3: Coupling constant $f$ versus dark matter mass for random points of the five dimensional parameter space (see the text for details). Only the orange points reproduce the observed relic density. The black line in the lower plot corresponds to the coannihilation limit given in Eq. (7.27). In the right panel we include only the points for which $r \lesssim 0.8$.

For the points that reproduce the correct relic density we expect, in the regime where $r \lesssim 0.8$, a lower limit on the coupling $f$ as a function of the dark matter mass, corresponding to the points where $z \sim 1$, namely to the coannihilation limit. In this case, annihilations are p-wave suppressed while coannihilations are not. Consequently, in the former case larger values of $f$ are required in order to reproduce the same total annihilation cross section. The lower limit can be analytically estimated using that $\langle \sigma_{\text{eff}} v \rangle \to f^4/(32\,\pi\,M_-^2)$ when $z \to 1$. Then, using Eq. (2.11), we can solve for $f$ as a function of $M_-$

$$f\bigg|_{z \to 1} \simeq \left( \frac{1.07 \times 10^{11}\,\text{GeV}^{-1}\,x_f}{g_*(x_f)^{1/2}\,m_{\text{Pl}}\,\Omega_{\text{DM}}h^2} \right)^{1/4} M_-^{1/2}, \tag{7.27}$$

which corresponds to the lower bound on the coupling constant $f$. We show in Fig. 7.3 as cyan points the values of the coupling constant $f$ versus the dark matter mass $M_-$ obtained from a scan over the five dimensional parameter space following the procedure described before; the orange points correspond to the subset of points that reproduce the observed relic density $\Omega_{\text{DM}}h^2 = 0.1199 \pm 0.0027$. In the left plot we include all points, whereas in right plot we show only those for which $r \lesssim 0.8$. From the latter, it is apparent the correlation between the coupling and the dark matter mass, as well as the existence of a lower limit on the coupling. This lower limit is reasonably well reproduced by the analytic expression reported in Eq. (7.27), calculated for $x_f = 25$ and shown in the plot as a black line, except for the orange points around $M_- = m_h/2 \simeq 63$ GeV, due to the Higgs resonance. In contrast, a correlation does not exist in the left plot, due to the presence of resonance and threshold effects.

## 7.3 Constraints from Direct Detection Experiments

In Fig. 7.4, we show the diagrams that are relevant for dark matter direct detection experiments. Following [143], we calculate the corresponding WIMP-nucleon scattering cross section

$$\sigma_{\psi-N} \;=\; C^2 \, \frac{f^2 \, m_N^4 \, M_-^2}{4\pi \, v_h^2 \, (M_- + m_N)^2} \left( \frac{1}{m_h^2} - \frac{1}{m_\rho^2} \right)^2 \sin^2 2\theta \,, \tag{7.28}$$

where $m_N$ denotes the nucleon mass and $C \simeq 0.27$ [79] is a constant that depends on the nucleon matrix element.

As shown in Fig. 7.4, there is a relative sign between the Higgs and the $\rho$ particle amplitudes, which is responsible for the destructive interference term in Eq. (7.28). Note that the scattering cross section has a strong dependence with $m_\rho$ (concretely with $m_\rho^{-4}$) when $m_\rho < m_h$, while it is independent of $m_\rho$ when $m_\rho > m_h$. These two limiting behaviors correspond to the regimes where the scattering is dominated by the $\rho$ scalar or by the Higgs boson, respectively. Besides, the scattering cross section is suppressed when $m_\rho \simeq m_h$.

The limits on the scattering cross section of dark matter particles with protons from the LUX experiment [82] translate into limits on the parameter space of our scenario. In the left panel of Fig. 7.5, as black lines we show the bounds on $f|\sin 2\theta|$ as a function of $m_\rho$ for various dark matter masses in between 8 GeV and 1000 GeV; in blue, orange and green we show the bound for $M_- = 8, 30$ and 1000 GeV respectively. The limits are stronger for dark matter masses close to 30 GeV, as a result of the larger sensitivity of the LUX experiment to WIMP masses around this value. Also, the dependence of the cross section with $m_\rho$ described above is reflected in the bound on $f|\sin 2\theta|$, as apparent from the plot.

For small values of $m_\rho$, namely smaller than about 6 GeV, masses probed by LUX satisfy $r \lesssim 0.8$. Hence, if the dark matter was produced thermally, the lower limit on $f$ of Eq. (7.27) can be applied in order to get an upper bound on $|\sin\theta|$. This is shown in Fig. 7.6. As before, the left panel shows, as black lines, the upper limits on $|\sin\theta|$ as a function of $m_\rho$ for various dark matter masses between 8 GeV and 1000 GeV; the limits for the concrete masses $M_- = 8, 30$ and 1000 GeV are shown in blue, orange and green, respectively. Besides, in the right panel of Fig. 7.6, we report the same limits as a function of the dark matter mass for fixed values of $m_\rho$. Notice that, above dark matter masses of about 30 GeV, the LUX limits on $|\sin\theta|$ are almost independent of the dark matter mass. In fact, the green and the orange lines almost coincide.
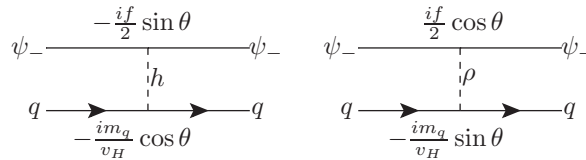


Figure 7.4: Relevant Feynman diagrams for dark matter direct detection experiments.
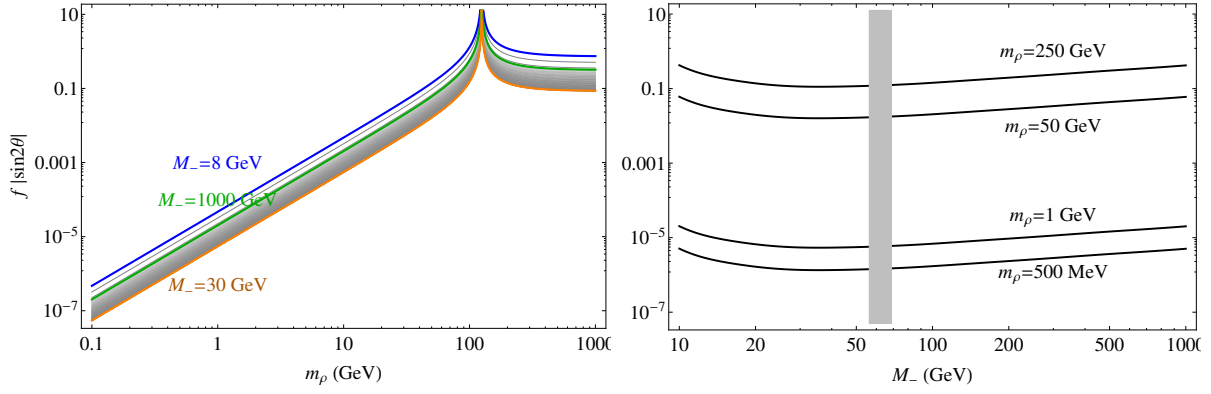
Figure 7.5: Upper bound on $f|\sin 2\theta|$ from LUX current limits on WIMP-nucleon cross sections (see the text for details).
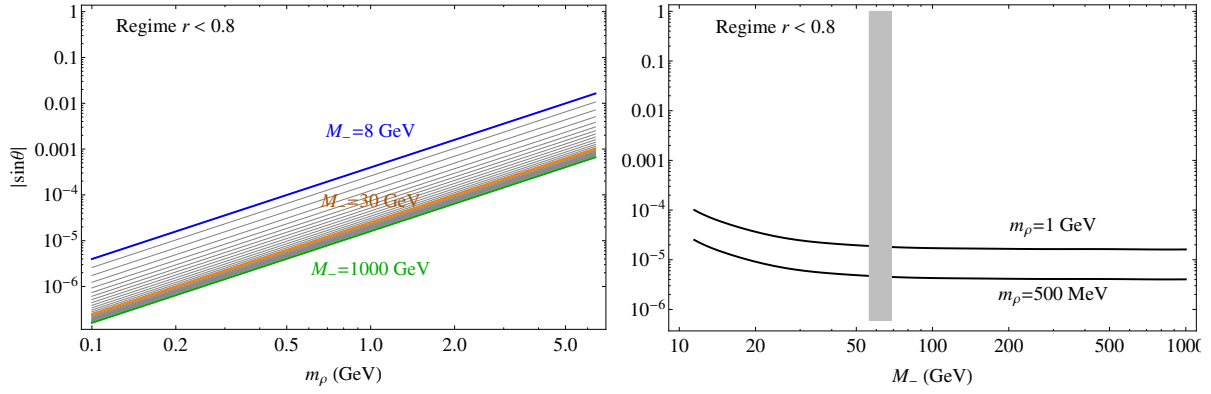


Figure 7.6: Same as Fig. 7.5, but for $|\sin\theta|$ in the region $r \lesssim 0.8$ (see text for details).

The region around the Higgs resonance in the right panel is not included since Eq. (7.27) does not apply.

# Chapter 8

# Model III: Dark Matter from a Chiral Fermion

As discussed in chapter 7, a plausible scenario for the dark sector consists in postulating a global $U(1)$ symmetry which is spontaneously broken to a remnant discrete $Z_2$ symmetry. In this way, the lightest particle with odd charge is absolutely stable and a potential candidate for dark matter. In the same chapter it was shown that the associated Goldstone boson plays a crucial role in dark matter production. Nevertheless, observing signatures of this model in indirect dark matter search experiments is challenging since all dark matter annihilation processes are p-wave suppressed.

In this chapter, we propose a variant of the model, where the Dirac fermion is replaced by a chiral fermion. We show that, due to the explicit $C$ and $P$ breaking, dark matter particles can annihilate in the s-wave, leading to non-negligible signals in indirect detection experiments. In fact, we consider a pseudo-Goldstone decaying into two photons, and show that under certain assumptions the corresponding gamma-ray flux from dark matter annihilations displays a characteristic box-shape spectrum with an intensity that could be at the reach of gamma-ray telescopes. These decays and the corresponding limits are discussed in chapter 10.

## 8.1 Description of the Dark Sector

We extend the Standard Model (SM) Lagrangian with one complex scalar field $\phi$, and one chiral fermion field, which we assume for concreteness left-handed, $\psi_L$ (the analysis for a right-handed field is analogous). These new fields are SM singlets and are charged under a global $U(1)_{\text{DM}}$ symmetry, namely $U(1)_{\text{DM}}(\psi_L) = 1$ and $U(1)_{\text{DM}}(\phi) = 2$. On the other hand, all the SM fields transform trivially under the additional global symmetry, which could be exact or nearly exact. Let us discuss each case separately.

### 8.1.1 Exact $U(1)_{\text{DM}}$ symmetry

If the global symmetry is exact, the interaction Lagrangian is

$$
\begin{aligned}
\mathcal{L} =\ & \mu_\Phi^2\, \Phi^\dagger\, \Phi - \lambda_\Phi \left( \Phi^\dagger\, \Phi \right)^2 + \mu_\phi^2\, \phi^\dagger\, \phi - \lambda_\phi \left( \phi^\dagger\, \phi \right)^2 - \kappa \left( \Phi^\dagger\, \Phi \right) \left( \phi^\dagger\, \phi \right) \\
& + i\overline{\psi_L}\gamma^\mu \partial_\mu \psi_L - \left( \frac{f}{\sqrt{2}} \phi\, \overline{\psi_L}\, \psi_L^{\text{c}} + h.c. \right),
\end{aligned}
\tag{8.1}
$$

where $\Phi$ is the SM Higgs doublet. Notice that the complex phase of the coupling constant $f$ can be absorbed by redefining the scalar field $\phi$. As a result, $CP$ is conserved in this model, while $C$ and $P$ are explicitly broken. Both the scalar field $\phi$ and the neutral component of the Higgs doublet acquire non-zero vacuum expectation values, which spontaneously break the symmetry group $SU(2)_{\mathrm{W}} \times U(1)_{\mathrm{Y}} \times [U(1)_{\mathrm{DM}}] \to U(1)_{\mathrm{em}} \times Z_2$. In order to analyze the physical mass spectrum of the theory, we conveniently parametrize the scalar fields in Eq. (8.1) as:

$$\Phi = \begin{pmatrix} G^+ \\ \frac{v_h + \tilde{h} + i G^0}{\sqrt{2}} \end{pmatrix} , \qquad \phi = \frac{v_\phi + \tilde{\rho} + i\eta}{\sqrt{2}} , \qquad (8.2)$$

where $v_h \simeq 246$ GeV.

**Scalar Sector:** This sector is identical to the one considered in the model of chapter 7. The scalar mass spectrum consists of a $CP$ odd massless scalar $\eta$, which is the Goldstone boson that arises from the spontaneous breaking of the global $U(1)_{\mathrm{DM}}$ symmetry, and two $CP$ even massive real scalars, denoted by $h$ and $\rho$ and with mass $m_h$ and $m_\rho$ respectively, which arise from the mixing of the interaction fields $\tilde{h}$ and $\tilde{\rho}$ by means of an angle $\theta$ [37]. The quartic couplings in the Lagrangian Eq. (8.1) can then be related to the masses and the mixing angle in the scalar sector by:

$$\lambda_\Phi = \frac{m_h^2 \cos^2\theta + m_\rho^2 \sin^2\theta}{2 v_h^2} , \qquad \lambda_\phi = \frac{m_h^2 \sin^2\theta + m_\rho^2 \cos^2\theta}{2 v_\phi^2} ,$$

$$\kappa = \frac{(m_\rho^2 - m_h^2)\sin 2\theta}{2\, v_h\, v_\phi} . \qquad (8.3)$$

**Fermionic Sector:** While the scalar potential of this model is identical to the one considered in chapter 7, the fermionic sector contains significant differences. Indeed, in this model only one Majorana fermion, which we denote by $\chi$, arises after the symmetry breaking. The corresponding mass-eigenstate and Majorana mass are

$$\chi = \psi_L + (\psi_L)^c , \qquad M_\chi = f v_\phi . \qquad (8.4)$$

With these definitions, the part of the Lagrangian involving $\chi$ can be cast as

$$\mathcal{L}_\chi = \frac{i}{2}\overline{\chi}\gamma^\mu\partial_\mu\chi - \frac{f}{\sqrt{2}}(\phi\overline{\chi}P_R\chi + \phi^*\overline{\chi}P_L\chi) , \qquad (8.5)$$

which after electroweak symmetry breaking becomes

$$\mathcal{L}_\chi = \frac{1}{2}(i\overline{\chi}\gamma^\mu\partial_\mu\chi - M_\chi\overline{\chi}\chi) - \frac{f}{2}((-\sin\theta h + \cos\theta\rho)\overline{\chi}\chi + i\eta\overline{\chi}\gamma^5\chi) . \qquad (8.6)$$

From Eqs. (8.3) and (8.4), it follows that there are four unknown independent parameters describing the dark sector, which can be taken as $m_\rho$, $\theta$, $M_\chi$ and $f$.

Notice that the Lagrangian in Eq. (8.5) is invariant under $U(1)_{\mathrm{DM}}$ upon the field transformations $\psi_L \to e^{i\alpha}\psi_L$, or equivalently, $\chi \to e^{-i\alpha\gamma^5}\chi$. [1] On the other hand, after the symmetry breaking,

---

[1]This transformation also leaves the Majorana condition $\chi = \chi^c$ invariant.

and due to the presence of the Majorana mass $M_\chi$, the Lagrangian is no longer invariant under the continuous transformation although, as expected, it preserves a remnant discrete symmetry $\chi \to -\chi$. The Majorana field $\chi$ then describes a stable neutral particle and is therefore a viable dark matter candidate.

We have assumed here the simplest scenario where the Majorana field $\chi$ transforms as a singlet of the global symmetry. More complicated scenarios can be constructed with identical properties regarding the dark matter stability, for example by assuming that the Majorana field transforms as a doublet of a global symmetry $SO(2) \cong U(1)$. This scenario is equivalent to the axion-mediated dark matter model discussed in [144, 145], in which the two components of the doublet form a Dirac fermion.

### 8.1.2 Nearly exact $U(1)_{\text{DM}}$ symmetry

We consider now the situation in which the global $U(1)_{\text{DM}}$ is not an exact symmetry of the Lagrangian. However, we assume that the Lagrangian Eq. (8.1) still describes to a very good approximation the phenomenology of the dark sector, *i.e.*, that the $U(1)_{\text{DM}}$ is a nearly exact symmetry. In particular, we demand that the stability of the dark matter is not affected by the explicit breaking of the global symmetry, that is we postulate that $Z_2$ is a symmetry of the part of the Lagrangian that breaks the global $U(1)_{\text{DM}}$ symmetry explicitly. If this is the case, the $\eta$ particle is a pseudo-Goldstone boson with a mass $m_\eta$ much smaller than the scale at which the global symmetry spontaneously breaks, namely $m_\eta \ll v_\phi$. We can therefore reasonably assume that $m_\eta \ll m_\rho$, and neglect the pseudo-Goldstone mass henceforth.

An important difference of this scenario compared to the one described in subsection 8.1.1 (or in chapter 7) is that, when the symmetry is nearly exact, the (massive) pseudo-Goldstone boson might decay into two photons. Such process is induced by the effective operator

$$\mathcal{L}_{eff} \supseteq -\frac{1}{4}\, g_{\eta\gamma}\, \epsilon^{\mu\nu\alpha\beta}\, F_{\mu\nu}\, F_{\alpha\beta}\, \eta \,, \tag{8.7}$$

where $g_{\eta\gamma}$ is a coupling constant with dimensions of inverse of energy and $F_{\mu\nu}$ is the electromagnetic field strength tensor. This Lagrangian arises in dark sectors with new chiral fermion representations charged under the SM group with masses of order $\Lambda \gg v_\phi$, that make the global $U(1)_{\text{DM}}$ symmetry anomalous. Consequently, in analogy to the neutral pions in the Standard Model, an effective coupling between the pseudo-Goldstone boson $\eta$ and the gauge fields might be generated by non-perturbative processes involving the new heavy degrees of freedom. For instance, this happens in axion-mediated dark matter models where the pseudo-Goldstone boson, the axion, arises from the spontaneous breaking of an anomalous Peccei-Quinn symmetry (see, *e.g.*, [144, 145]). In this work we adopt a phenomenological approach and simply assume that the operator given in Eq. (8.7) exists, without specifying the new physics responsible for its origin.

## 8.2 Constraints from Direct Searches and the Invisible Higgs Decay Width

**Higgs Decay:** The scalar $\rho$ and the Higgs boson $h$ might decay into two dark matter particles, two (pseudo-)Goldstone bosons or SM particles. The relevant decay widths for $\rho$ read

$$\Gamma(\rho \to \eta\,\eta) \;=\; \frac{f^2\,r^2}{32\,\pi}\,m_\rho \cos^2\theta, \tag{8.8}$$

$$\Gamma\left(\rho \to \chi\chi\right) \;=\; \frac{f^2}{16\,\pi}\left(1 - \frac{4}{r^2}\right)^{3/2} m_\rho \cos^2\theta\,, \tag{8.9}$$

$$\Gamma\left(\rho \to \text{SM particles}\right) \;=\; \sin^2\theta\,\Gamma^{\text{SM}}\left(\text{Higgs} \to \text{SM particles}\right), \tag{8.10}$$

where $r \equiv m_\rho/M_\chi$. The corresponding expressions for $h$ are obtained by exchanging $\cos\theta$ for $\sin\theta$ and $m_\rho$ for $m_h$. In addition, the heaviest $CP$ even scalar can decay into the lightest one with a phase space suppressed rate (in the same way as explained in subsection 7.1.3). From these equations and the experimental upper limit on the invisible decay width of the Higgs boson (see, *e.g.*, [141]), it follows that the mixing angle $\theta$ is bounded from above by [34]:

$$|\tan\theta| \;\lesssim\; 2.2 \times 10^{-3}\left(\frac{v_\phi}{10\,\text{GeV}}\right) \quad \text{or} \quad f\,|\sin 2\theta| \;\lesssim\; 4.4 \times 10^{-3}\left(\frac{M_\chi}{10\,\text{GeV}}\right), \tag{8.11}$$

where in the last expression we have used Eq. (8.4).

**Direct Detection Experiments:** Direct dark matter searches constrain the same combination of parameters, $f\,|\sin 2\theta|$. The calculation of the scattering cross section of dark matter off nucleons is analogous as in section 7.3, the result being

$$\sigma_{\chi N} \;=\; C^2\,\frac{m_N^4\,M_\chi^2}{4\pi\,v_h^2\,(M_\chi + m_N)^2}\left(\frac{1}{m_h^2} - \frac{1}{m_\rho^2}\right)^2 (f\,\sin 2\theta)^2\,, \tag{8.12}$$

where $m_N$ denotes the nucleon mass and $C \simeq 0.27$ [79] is a constant that depends on the nucleon matrix element. In Fig. 8.1 we show, as black lines, the upper limit on $f|\sin 2\theta|$ as a function of $m_\rho$ for various dark matter masses between 8 GeV and 1000 GeV from the invisible Higgs decay width, Eq. (8.11), and from the LUX experiment [82], Eq. (8.12); the blue, orange and green lines correspond to $M_\chi = 8, 30$ and 1000 GeV respectively. It follows from the plot that for $\rho$ masses below 10 GeV the bound on $f|\sin 2\theta|$ is determined by direct detection experiments, whereas for $m_\rho$ larger than 100 GeV, by the upper limit on the invisible Higgs decay width (dominated in this mass range by $h \to \eta\eta$).

## 8.3 Thermal Production of Dark Matter

The thermal production of dark matter is expected to be dominated by annihilation channels involving the $\rho$ scalar and the (pseudo-)Goldstone boson, as in the model introduced in chapter 7; the relevant diagrams are shown in Fig. 8.2 and the expressions for the corresponding cross
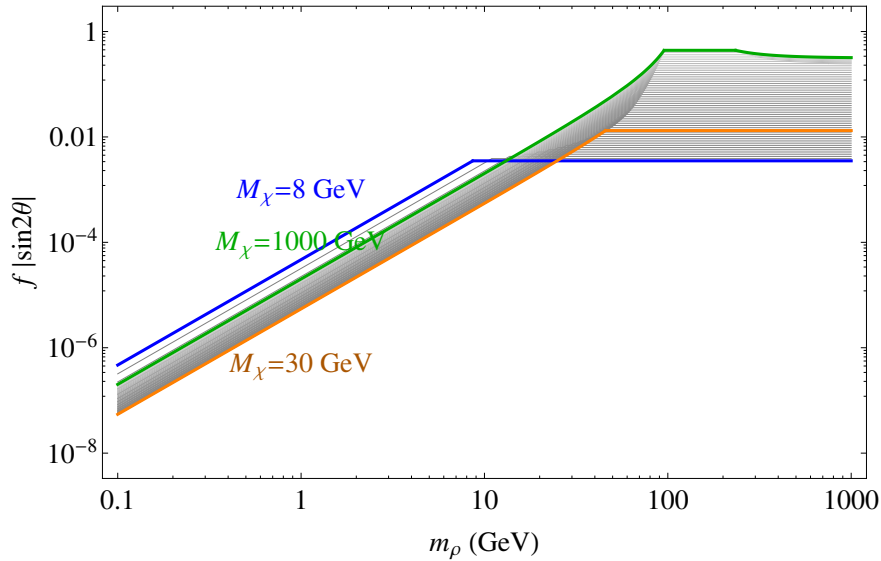
Figure 8.1: Combined upper limit on $f|\sin 2\theta|$ from direct dark matter searches and the invisible Higgs decay width as a function of the mass of the $CP$ even dark scalar for various values of the dark matter mass.

sections are reported in Appendix B. On the other hand, annihilations into SM particles are expected to have a fairly suppressed rate, due to the smallness of the mixing angle $\theta$, except when the dark matter annihilation proceeds via resonant s-channel exchange of $CP$ even scalars, that is, either $\rho$ or $h$.

These expectations are confirmed by our numerical analysis. We have performed scans over the four dimensional parameter space spanned by $m_\rho$, $M_\chi$, $f$ and $\theta$. More specifically, we have performed a logarithmic scan of $m_\rho$ between 200 MeV and 1 TeV, $M_\chi$ between 1 GeV and 1 TeV, $f$ between $10^{-2}$ and $4\pi$ and $|\tan\theta|$ between 0 and the maximal value allowed by the invisible decay width of the Higgs, given in Eq. (8.11) with $v_\phi = M_\chi/f$ (see Eq. (8.4)). We have also checked that the quartic couplings necessary to produce these parameters, inferred from Eq. (8.3), are smaller than $4\pi$, in order to ensure perturbativity. We have then calculated for each point the dark matter relic density using micrOMEGAs 3.1 [79], working under an implementation of our model made with FeynRules [125], and we have selected only those points for which $\Omega_{\text{DM}}h^2 = 0.1199 \pm 0.0027$ within $3\sigma$. We report the results of one scan in Fig. 8.3, where we show the relative contribution to the relic density of each annihilation process for the concrete case $m_\rho = 50$ GeV. Indeed, the dominant channel is $\chi\chi \to \rho\eta$, when this is kinematically open, *i.e.* for $m_\rho < 2M_\chi$, while $\chi\chi \to \eta\eta$ dominates when $m_\rho > 2M_\chi$. It is important to note that for certain values of $m_\rho$ threshold effects or resonant effects can have a dramatic impact in the calculation of the relic density (see section 2.2.3), concretely when $m_\rho \approx M_\chi$, close to the threshold of the process $\chi\chi \to \rho\rho$, or when $m_\rho \approx 2M_\chi$, close to the threshold of $\chi\chi \to \rho\eta$ and where moreover
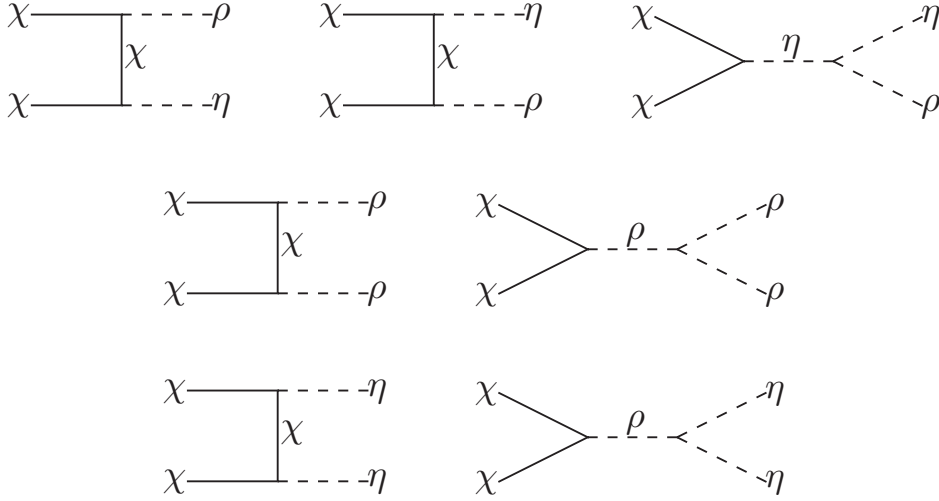
Figure 8.2: Relevant diagrams for dark matter production in the limit $\theta \ll 1$. The process into $\rho\eta$ (first row) proceeds via s-wave, whereas the other ones are p-wave suppressed.

the process $\chi\chi \to \eta\eta$ via the s-channel mediation of $\rho$ is resonantly enhanced. Resonance effects are manifest in Fig. 8.3 at $M_\chi = m_h/2 \approx 63$ GeV and $M_\chi = m_\rho/2 \approx 25$ GeV, where the Higgs and $\rho$ resonances take place, respectively.

In order to determine the precise regions where threshold and resonance effects have an important impact on the relic density, we have calculated the thermal average of the annihilation cross sections as a function of $r = m_\rho/M_\chi$; the result is shown in Fig. 8.4 for a typical freeze-out temperature, $T \sim M_\chi/20$, and for various values of $f$ which, following Eqs. (8.8) and (8.9), determine the width of $\rho$. As apparent from the plot, the threshold and resonant effects are most relevant in the region $1.5 \lesssim r \lesssim 3$. Furthermore, for $r \lesssim 1.5$ the largest annihilation cross section corresponds to the process $\chi\chi \to \rho\eta$, while for $r \gtrsim 3$ to $\chi\chi \to \eta\eta$. Notice that, for a given coupling $f$, the upper limit $r \lesssim \sqrt{8\pi}/f$ must hold from the requirement of perturbativity, as also reflected in Fig. 8.4.

In the regions where both resonance and threshold effects are negligible, namely $r \lesssim 1.5$ or $r \gtrsim 3$, the relic abundance can be accurately calculated using the instantaneous freeze-out approximation [80]. Casting the annihilation cross section in the form $\sigma v = a + bv^2$, according to Eq.(2.11),the relic density can be approximated by

$$\Omega_{\mathrm{DM}} h^2 \simeq \frac{\left(1.07 \times 10^9 \,\mathrm{GeV}^{-1}\right) x_f}{g_*(x_f)^{1/2} \, m_{\mathrm{Pl}} \left(a + 3(b - a/4)/x_f\right)} . \tag{8.13}$$
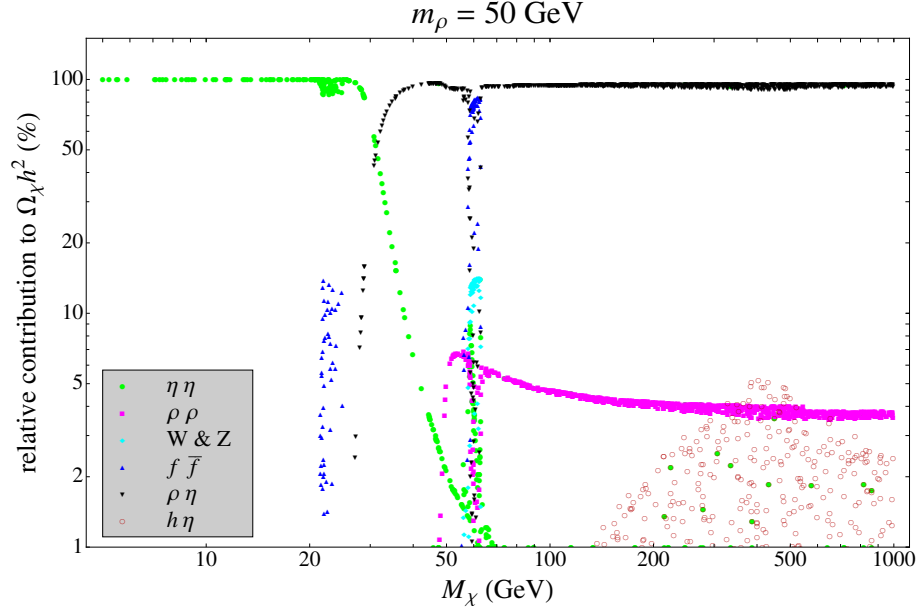
Figure 8.3: Relative contribution to the dark matter relic density from various annihilation channels as a function of the dark matter mass, assuming $m_\rho = 50$ GeV.
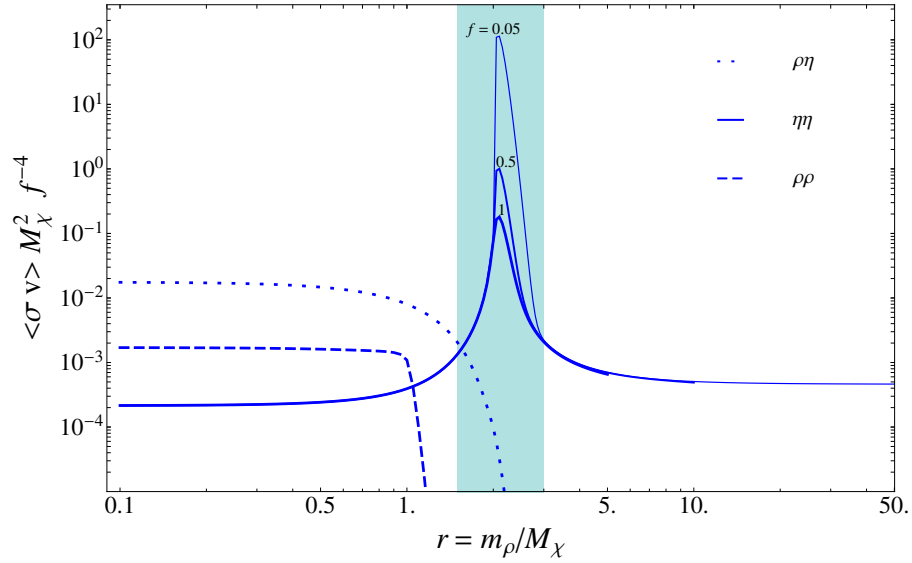


Figure 8.4: Thermally averaged cross section $\langle \sigma v \rangle$ for the annihilation channels $\chi\chi \to \rho\eta$, $\eta\eta$, $\rho\rho$ as a function of $r \equiv m_\rho/M_\chi$ at the typical freeze-out temperature $T = M_\chi/20$. The resonant behavior of the annihilation into $\eta\eta$ at $r = 2$ is due to the s-channel mediation of a $\rho$, with a width determined by the coupling constant $f$.

## 8.4 Dark Matter Annihilations and the $CP$ Symmetry

In the regime $r \lesssim 1.5$ the three annihilation processes into dark sector particles $\chi\chi \to \rho\rho$, $\eta\eta$, $\rho\eta$ and $\chi\chi \to$ SM SM are all kinematically accessible. The annihilations into $\rho\rho$ and $\eta\eta$ are, however, p-wave suppressed and can be safely neglected in the calculation of the relic density. This can be understood analyzing the $CP$ of the initial and final states. As in chapter 7, we use the standard notation $S$, $L$ and $J$ for the spin, the orbital and the total angular momenta with a subscript $i$ or $f$ for the corresponding quantities of the initial or final state. Then, the $CP$ eigenvalues of the initial and final states are $(-1)^{L_i+1}$ and $(-1)^{L_f}$ (as shown in Table A.1). $CP$ conservation thus implies that $|L_f - L_i|$ is an odd number. In addition, since $\rho$ and $\eta$ are scalars, we have $J_i = L_f$. If the s-wave were allowed $L_i = 0$ and $J_i = S_i$. As a result we could only have $S_i = 1$ and $L_i = 0$, which is impossible for a pair of Majorana fermions due to the Pauli exclusion principle (see Eq. (A.9)). The only possibility is then $L_i \geq 1$ and hence the cross sections are p-wave suppressed. Explicitly, they read

$$\sigma v(\chi\chi \to \rho\rho) = \frac{f^4 v^2 \sqrt{1-r^2}}{384\pi M_\chi^2} \frac{\left(3r^4 - 8r^2 + 8\right)\left(9r^8 - 64r^6 + 200r^4 - 352r^2 + 288\right)}{\left(r^2 - 4\right)^2 \left(r^2 - 2\right)^4} , \quad (8.14)$$

$$\sigma v(\chi\chi \to \eta\eta) = \frac{f^4 v^2}{192\pi M_\chi^2 \left(r^2 - 4\right)^2} \left(8 + r^4\right) , \quad (8.15)$$

which are manifestly velocity suppressed. In contrast, for the annihilation into $\rho\eta$ the $CP$ eigenvalues of the initial and final states are $(-1)^{L_i+1}$ and $(-1)^{L_f+1}$ (as shown in Table A.1). We again have $J_i = L_f$, and therefore $|J_i - L_i|$ is an even number. $CP$ conservation therefore allows the s-wave channel if $J_i$ is even. The corresponding cross section is

$$\sigma v(\chi\chi \to \rho\eta) = \frac{f^4}{16\pi M_\chi^2} \left(1 - \frac{r^2}{4}\right)^3 . \quad (8.16)$$

Lastly, annihilations into SM particles are p-wave suppressed due to $CP$ conservation, and are moreover $\theta$-suppressed. Therefore, they can be safely neglected in our analysis. Hence, in the regime $r \lesssim 1.5$ the relevant process for the calculation of the relic density is the annihilation $\chi\chi \to \rho\eta$. On the other hand, in the regime $r \gtrsim 3$, the only kinematically open channels are $\chi\chi \to \eta\eta$ and $\chi\chi \to$ SM SM. Both processes are p-wave suppressed, however the latter has an additional $\theta$-suppression. Therefore, the dominant annihilation process is in this case into $\eta\eta$ with a cross section given in Eq. (8.15).

Using Eq. (8.13) it is then possible to estimate the value of the dark matter coupling $f$ as function of $r$ and $M_\chi$ (and $x_f$) leading to the observed dark matter abundance $\Omega_{\rm DM}h^2 \simeq 0.12$ in the regime $r \lesssim 1.5$ (where the annihilation into $\rho\eta$ with a cross section given by Eq. (8.16) determines the dark matter freeze-out) and in the regime $r \gtrsim 3$ (where the annihilation into $\eta\eta$ is the relevant one, with cross section given by Eq. (8.15)). The coupling reads:
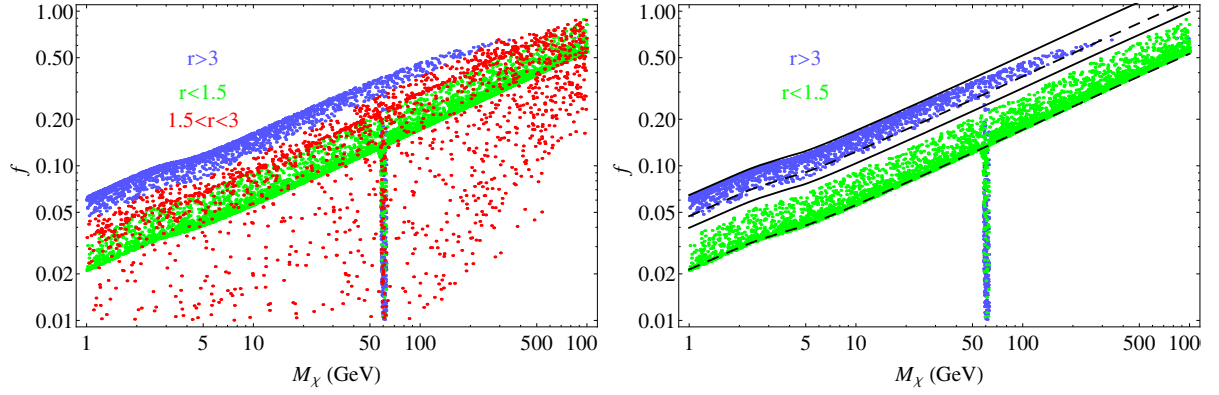
Figure 8.5: *Left plot*: value of the coupling constant $f$ required to produce thermally the observed dark matter abundance for various values of the dark matter mass and the $CP$-even scalar mass, expressed as $r = m_\rho/M_\chi$. The color code denotes $r > 3$, $r < 1.5$ and $1.5 < r < 3$ for blue, green and red respectively. Besides, the solid (dashed) line shows the maximum (minimum) values of the coupling predicted by Eq. (8.17). *Right plot*: The same as the left plot, but removing the points with $1.5 < r < 3$, to highlight the validity of the approximation Eq. (8.17).
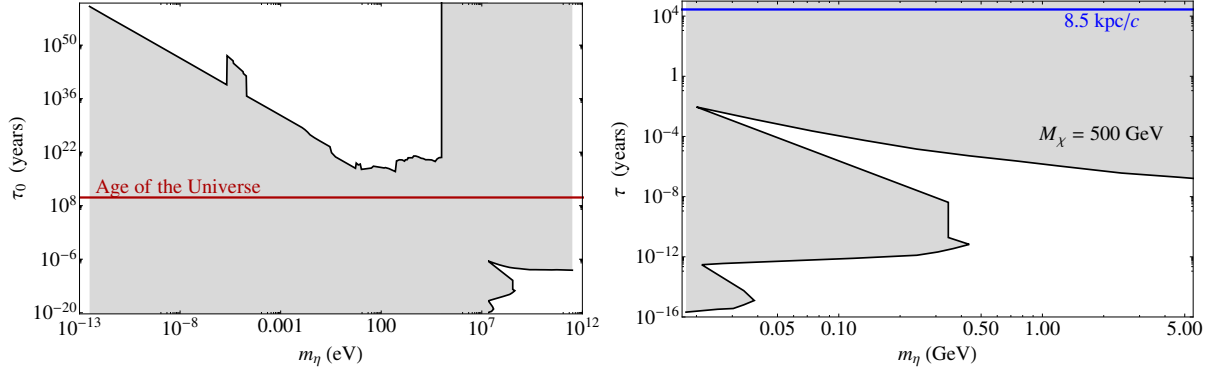


Figure 8.6: *Left plot*: allowed regions for the mass and proper lifetime of a pseudo-Goldstone boson (adapted from Fig. 6-1 of [146] using Eq. (8.18)). *Right plot*: allowed regions for the mass and lifetime of a pseudo-Goldstone bosons produced by dark matter annihilations assuming $M_\chi = 500$ GeV, compared to the time required to reach the earth from the galactic center. Here $\tau \simeq (M_\chi/m_\eta)\,\tau_0$ (see text for details).

$$f \simeq \begin{cases} 0.39 \left( \dfrac{x_f}{g_*(x_f)^{1/2} (4-r^2)^3} \right)^{1/4} \left( \dfrac{M_\chi}{100 \text{ GeV}} \right)^{1/2} & , \quad \text{if} \quad r \lesssim 1.5 \\[3mm] 0.20 \left( \dfrac{(4-r^2)^2 x_f^2}{g_*(x_f)^{1/2} (8+r^4)} \right)^{1/4} \left( \dfrac{M_\chi}{100 \text{ GeV}} \right)^{1/2} & , \quad \text{if} \quad r \gtrsim 3 \end{cases} . \tag{8.17}$$

To check the validity of our approximations, we have calculated the values of the coupling constant $f$ versus the dark matter mass $M_\chi$ leading to the observed dark matter abundance in a scan over the four dimensional parameter space performed as described at the beginning of this section. The result is shown in Fig. 8.5, left plot, where we have identified with a color the value of $r$ corresponding to each point: blue, green and red for $r > 3$, $r < 1.5$ and $1.5 < r < 3$, respectively. In the right plot, we have removed the points within the resonant and threshold region $1.5 < r < 3$, clearly showing the existence of two separate bands corresponding to the regimes $r < 1.5$ and $r > 3$. In the former case, the freeze-out is dominated by the s-wave annihilation channel into $\rho \eta$, whereas in the latter, by the p-wave annihilation into $\eta$ pairs. Consequently, in the case of $r > 3$, larger values of $f$ are required in order to reproduce the same relic abundance. We also show the lines corresponding to maximum (continuous) and minimum (dashed) values predicted by Eq. (8.17) for both $r < 1.5$ and $r > 3$, assuming $x_f = 22$. As apparent from the plot, the lines obtained using Eq. (8.17) describe fairly well each region except for the points around $M_\chi = m_h/2 \simeq 63$ GeV where, due to the existence of the Higgs resonance, Eq. (8.17) does not apply.

## 8.5 Signatures of Pseudo-Goldstone Bosons

The signatures of the pseudo-Goldstone bosons in this model crucially depend on their lifetime. If the pseudo-Goldstone bosons $\eta$ are long-lived, they could have survived until the recombination era, possibly leaving their footprints in the Cosmic Microwave Background (CMB) in the form of dark radiation [34, 37]. On the other hand, if they are short-lived, we could detect their decay products after being produced in dark matter annihilations, *e.g.*, in the center of our Galaxy.

The decay rate of $\eta$ into two photons can be straightforwardly calculated from the effective Lagrangian Eq. (8.7), the result being:

$$\Gamma(\eta \to \gamma \, \gamma) = \frac{g_{\eta\gamma}^2 \, m_\eta^3}{64\pi} . \tag{8.18}$$

The relevant parameters $m_\eta$ and $g_{\eta\gamma}$, or equivalently $m_\eta$ and the proper lifetime $\tau_0 = \mathrm{Br}(\eta \to \gamma\gamma)/\Gamma(\eta \to \gamma\,\gamma)$, are constrained by experimental searches for pseudo-Goldstone bosons. The allowed values of the pseudo-Goldstone lifetime as a function of the mass are shown in the left plot of Fig. 8.6, under the assumption $\mathrm{Br}(\eta \to \gamma\gamma) = 1$ (plot adapted from Fig. 6-1 of [146]). As apparent from the plot there are two disjoint allowed regions: either the pseudo-Goldstone has a lifetime longer than $\sim 10^{20}$ years or it has a lifetime shorter than one minute.

In the former case, if we assume that $\eta$ contributes to the radiation density of the Universe at the time of recombination or at Big Bang Nucleosynthesis, then the pseudo-Goldstone boson must be present in the Universe also today. On the other hand, for the latter case, if the pseudo-Goldstone has a lifetime much shorter than the age of the Universe, all the primordial pseudo-Goldstone bosons must have decayed today. Nevertheless, the model predicts a non-negligible pseudo-Goldstone production in regions with a high dark matter density, such as the Milky Way center, from the s-wave annihilations into a pseudo-Goldstone boson and a *CP* even dark scalar, provided this annihilation channel is kinematically open. These pseudo-Goldstone bosons have an energy of the order of $M_\chi$, which implies that their lifetime (in the Galactic frame) is given by $\tau \simeq (M_\chi / m_\eta) \, \tau_0$. In this window $m_\eta \gtrsim 10$ MeV, hence the lifetime of the pseudo-Goldstone bosons produced in dark matter annihilations is typically much shorter than one year, as shown in Fig. 8.6, right plot, for the particular case $M_\chi = 500$ GeV, compared to the lifetime required to reach the earth, shown as a blue line. Therefore, pseudo-Goldstone bosons decay in flight before reaching the earth producing a gamma-ray flux that could be detected in gamma-ray telescopes. A similar conclusion holds for other values of the dark matter mass. We analyze these two possibilities separately in chapters 9 and 10 respectively.

# Chapter 9

# Goldstone Bosons as Dark Radiation and the Interplay with Direct Searches

In this chapter we assume that the (pseudo-)Goldstone boson is absolutely stable or at least that it remained stable until the recombination era. If this is the case, it contributed to the radiation energy density of the Universe when the CMB was formed.

## 9.1 Contribution of the (Pseudo-)Goldstone Bosons to $N_{\text{eff}}$

Because the (pseudo-)Goldstone bosons are very light particles, they contribute to the radiation energy density of the Universe. In particular, as pointed out in [34], if they go out of equilibrium before the annihilation of the $e^{\pm}$ pairs, but after the decoupling of most of the SM fermions, they might fake extra neutrino species in the measurements of the anisotropies in the cosmic microwave background (CMB) [35]. This effect can be quantified in terms of the effective number of neutrino types, $N_{\text{eff}}$, present before the era of recombination.

In analogy to section 2.4 and following [147], we define $T_\eta^0$ and $T_\eta^d$ as the temperature of the Goldstone bosons at the recombination era and at their decoupling from the thermal bath, respectively. A similar notation is understood for all the other particles. In terms of these, the energy density associated to the (pseudo-)Goldstone bosons compared to the photon energy density is given by

$$\frac{\rho_\eta^0}{\rho_\gamma^0} = \frac{1}{2}\left(\frac{T_\eta^0}{T_\gamma^0}\right)^4.$$  (9.1)

The factor $1/2$ in front is because photons have two helicities states and the (pseudo-)Goldstone bosons only one. Using this expression and the definition of $N_{\text{eff}}$ from Eq. (2.22), it is possible to conclude that the contribution of the (pseudo-)Goldstone bosons to $N_{\text{eff}}$ is

$$\Delta N_{\text{eff}} = \frac{4}{7}\left(\frac{T_\eta^0}{T_\nu^0}\right)^4.$$  (9.2)

In the present scenario we expect the massless scalars to be very weakly interacting with the SM particles, in fact even more than neutrinos. Therefore, they must decouple at a temperature

$$g_* = 2 + \frac{7}{8}\left(2 + 2 + 2 + 2 + 3(1+1)\right) = \frac{57}{4}$$

$$g_* = 2 + \frac{7}{8}\left(2 + 2 + 3(1+1)\right) = \frac{43}{4}$$

$\gamma\, e^{\pm}\, \mu^{\pm}\, \nu\, \overline{\nu}\, \eta \qquad \gamma\, e^{\pm}\, \mu^{\pm}\, \nu\, \overline{\nu} \qquad \gamma\, e^{\pm}\, \nu\, \overline{\nu} \qquad\qquad \gamma\, e^{\pm} \qquad \gamma$

$T_\eta^d$ $\qquad$ $\mu^{\pm}$ annihilation $\qquad$ $T_\nu^d$ $\qquad$ $e^{\pm}$ annihilation

$\eta$ $\qquad\qquad\qquad\qquad$ $\nu\, \overline{\nu}$

T

t
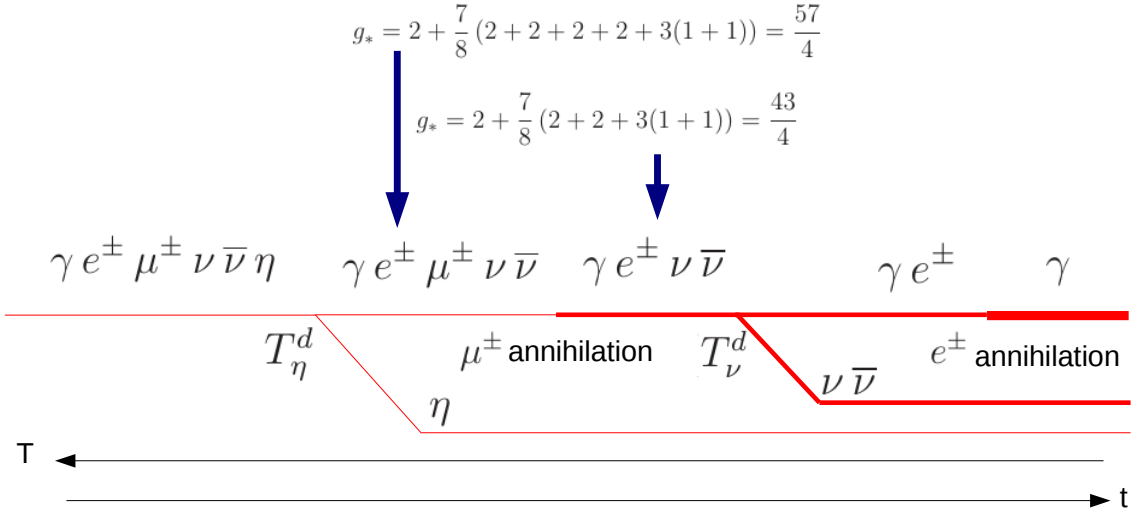
Figure 9.1: Sketch of the processes that the radiation of the universe underwent when the (pseudo-)Goldstone bosons went out of equilibrium. The red line represents the *relative* temperature of the different fluids. The thicker the line, the higher the relative temperature. See Fig. 2.2 for comparison.

$T_\eta^d > T_\nu^d$, with $T_\nu^d \simeq 2-3$ MeV [40, 114–116], which in turn implies that the ratio $T_\eta/T_\nu$ today is the same as it was at $T_\nu^d$ because neutrinos and Goldstone bosons have been decoupled from the thermal bath ever since the temperature dropped below $T_\nu^d$. Moreover, the temperature of the neutrinos and the Goldstone bosons are not the same at $T_\nu^d$ because in between the Goldstone boson and neutrino decoupling epochs, the thermal bath underwent a reheating process due to the annihilations of some of the fermions in the plasma. These processes are sketched in Fig. 9.1.

The difference in temperature can be quantified by considering the conservation of the entropy per comoving volume during that period of time. This implies that $g_* T^3$ remained constant, where $g_*$ stands for the effective number of relativistic degrees of freedom. As a consequence of all this, we have

$$\left(\frac{T_\eta^0}{T_\nu^0}\right)^3 = \left(\frac{T_\eta}{T_\nu}\right)^3_{T_\nu^d} = \frac{g_{*\text{after}}}{g_{*\text{before}}}, \tag{9.3}$$

with[1] $g_{*\text{after}} = 43/4 = 10.75$ (see Fig. 9.1). In this work we assume that the Goldstone bosons decouple just before muon annihilation. As a result $g_{*\text{before}} = 57/4$, which from Eq. (9.2) corresponds to an effective number of neutrinos $N_{\text{eff}} - 3 = (4/7)(43/57)^{4/3} \simeq 0.39$ [34]. This is consistent within $1\sigma$ with the recent experimental data [35], $N_{\text{eff}} = 3.36 \pm 0.34$.

---

[1]This results is strictly valid under the assumption that the neutrinos decouple instantaneously and that at $T_\nu^d$
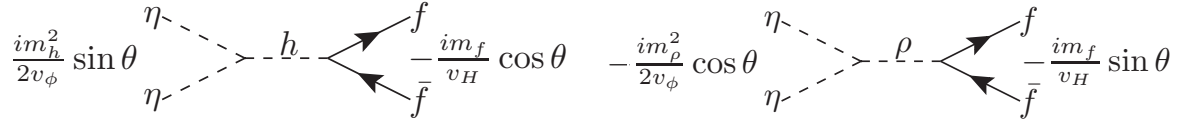
Figure 9.2: Relevant Feynman diagrams for Goldstone boson annihilation into SM fermions.

## 9.2 Boltzmann Equations for Dark Radiation

In order to analyze carefully the conditions under which the Goldstone bosons decouple from the thermal bath, we consider the Boltzmann equation describing the evolution in the early Universe of the Goldstone boson number density, $n_\eta$. We assume for simplicity that the $\rho$ scalar and the dark matter are no longer present in the thermal bath at the decoupling of the Goldstone. If that is the case, the evolution of $n_\eta$ is described by

$$\frac{dn_\eta}{dt} + 3\,H\,n_\eta = -\sum_f \langle \sigma v \rangle_{\eta\eta \to f\bar{f}} \left( n_\eta^2 - (n_\eta^{eq})^2 \right), \tag{9.4}$$

where the sum runs over the fermions that are in equilibrium the thermal bath. Besides, $n_\eta^{eq} = T^3/\pi^2$ is the number density of a massless (real) scalar and $H \simeq 1.66\sqrt{g_*(T)}\,T^2/m_{\text{Pl}}$ is the expansion rate of the Universe. This equation is valid under the assumptions that the SM fermions in Eq. (9.4) are always in thermal equilibrium and that the Goldstone bosons remain in kinetic equilibrium right after the decoupling [78], due to elastic scatterings. Moreover, we use the Boltzmann energy distribution for all the interacting particles, which is a good approximation for temperatures $T \lesssim 3\,m_f$, $m_f$ being the mass of the fermions produced in Goldstone boson annihilations.

The thermal averaged annihilation cross section $\langle \sigma v \rangle_{\eta\eta \to f\bar{f}}$ is given by (see *e.g.* [78]):

$$\langle \sigma v \rangle_{\eta\eta \to f\bar{f}} \equiv \frac{1}{32\,T^5} \int_{4\,m_f^2}^{\infty} \sigma(\eta\eta \to f\bar{f})\,s\,\sqrt{s}\,K_1\left(\sqrt{s}/T\right)\,ds, \tag{9.5}$$

with [2]

$$\sigma(\eta\eta \to f\bar{f}) = \frac{m_f^2\,\kappa^2}{8\pi}\,\frac{\left(1 - 4\,m_f^2/s\right)^{3/2}\left(s^2\left(m_h^2 - m_\rho^2\right)^2 + m_\rho^2\,m_h^2\,(m_\rho\,\Gamma_h - m_h\,\Gamma_\rho)^2\right)}{\left(m_h^2 - m_\rho^2\right)^2\left((s - m_h^2)^2 + \Gamma_h^2\,m_h^2\right)\left((s - m_\rho^2)^2 + \Gamma_\rho^2 m_\rho^2\right)}, \tag{9.6}$$

where $\Gamma_{h,\rho}$ is the decay width of the scalar particle mediating the s-channel annihilation cross section.

---

the $e^\pm$ pairs are essentially massless [148].

[2] Notice that in the definition (9.5) a factor $1/2$ should be introduced to avoid double counting of the initial particle states. On the other hand, the collision term in the Boltzmann equations (9.4) must be multiplied by 2 because of the annihilation of a pair of $\eta$'s. Therefore, the definitions (9.4) and (9.5) are consistent.
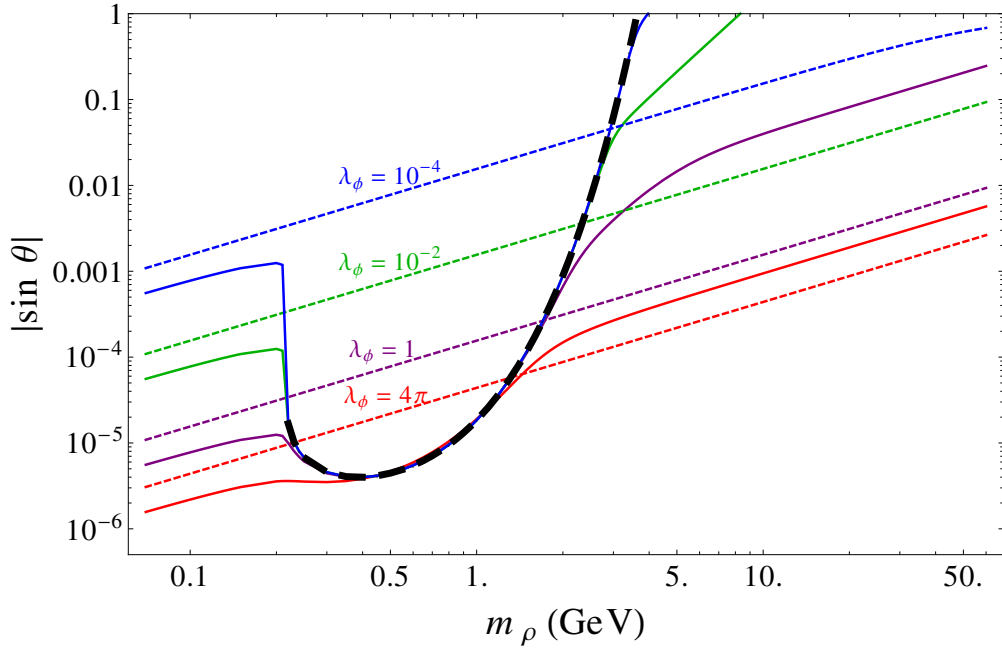
Figure 9.3: Lower limit on $|\sin\theta|$ for fixed values of $\lambda_\phi$ (continuous lines) corresponding to Goldstone boson decoupling at $T \approx m_\mu$. Upper limit on $|\sin\theta|$ for fixed values of $\lambda_\phi$ (dashed lines) given by the constraints on the Higgs boson invisible decay width. The thick dashed black curve is obtained using the analytic expression reported in Eq. (9.14).

The departure from equilibrium, in this case the decoupling of $\eta$ from the plasma, according to Eq. (9.4), takes place roughly at the temperature $T_\eta^d$ at which the following condition is satisfied:

$$
\left. \frac{n_\eta^{eq} \; \sum_f \langle \sigma v \rangle_{\eta\eta \to f\bar{f}}}{H} \right|_{T=T_\eta^d} = 1 \; . \tag{9.7}
$$

Using the previous expression, we can calculate the minimum value of $|\kappa|$ or, equivalently, $|\sin\theta|$ (see Eq. (7.10)), for which $\eta$ decouples from the thermal bath at temperature $T_\eta^d \approx m_\mu$. Notice that since the cross section (9.6) is proportional to the squared mass of the fermion, it is enough to consider only the annihilation into $\mu^\pm$ pairs in (9.7).

We report in Fig. 9.3 the full numerical calculation of the lower limit of $|\sin\theta|$, for fixed values of the quartic coupling $\lambda_\phi$ (continuous lines). We also show the corresponding upper bound derived from the invisible decay width of the Higgs boson (dashed lines). We can see from this plot that there are three different regimes according to the value of the $\rho$ mass. It turns out, that for each of them it is possible to find approximate analytical expressions.

**Regime I: $m_\rho \gtrsim 4$ GeV**

In this regime, the values of the center of mass energy contributing to the integral are always much smaller the masses of the scalar particles which mediate the annihilation. As a result we can neglect $s$ in the denominator of (9.6). Furthermore, if the decay width of the $\rho$ scalar can be neglected with respect to the other terms in Eq. (9.6), then the thermal annihilation cross section into $\mu^+ \mu^-$ in Eq. (9.5) is approximately:

$$\langle \sigma v \rangle_{\eta\eta\to\mu^+\mu^-} \;=\; \frac{\kappa^2}{128\,\pi}\,\frac{m_\mu^2\,T^4}{m_h^4\,m_\rho^4} \int_{2\,m_\mu/T}^{\infty} w^8\, K_1(w)\,\mathrm{d}w\,. \tag{9.8}$$

Taking $T = T_\eta^d \simeq m_\mu$ in the previous equation, then the requirement of having a scalar dark radiation component, Eq. (9.7), implies

$$|\kappa| \;\gtrsim\; \frac{m_h^2\,m_\rho^2}{m_{\mathrm{Pl}}^{1/2}\,m_\mu^{7/2}}\,. \tag{9.9}$$

This condition was derived for the first time in [34] and used to estimate a lower bound on $|\kappa|$ for $m_\rho \approx 500$ MeV. Finally, from relation (7.10) we can express the condition above as a lower limit on the scalar mixing angle $\theta$. Namely, in this mass range for $\rho$ we have

$$|\sin\theta| \;\gtrsim\; 1.3 \times 10^{-7}\,\lambda_\phi^{-1/2}\left(\frac{m_\rho}{0.1\,\mathrm{GeV}}\right)^3\,. \tag{9.10}$$

Such values of the mixing angle are excluded by the present collider constraints on the invisible decay width of the Higgs boson derived previously, Eq. (7.22).

In contrast, if the terms that depend on $\Gamma_\rho$ dominate in the numerator of (9.6), that is if $s < \Gamma_\rho\,m_\rho$ for the values of $s$ that contribute to the integral, then the annihilation cross section is described by

$$\begin{aligned}
\langle \sigma v \rangle_{\eta\eta\to\mu^+\mu^-} &\;=\; \frac{\kappa^2}{128\,\pi\,m_h^2}\left(\frac{m_\mu\,\Gamma_\rho}{m_h\,m_\rho}\right)^2 \int_{2\,m_\mu/T}^{\infty} w^4\, K_1(w)\,\mathrm{d}w \\
&\;=\; \frac{\kappa^2}{128\,\pi\,m_h^2}\left(\frac{m_\mu}{m_h}\right)^2\left(\frac{\lambda_\phi}{16\pi}\right)^2 \int_{2\,m_\mu/T}^{\infty} w^4\, K_1(w)\,\mathrm{d}w\,,
\end{aligned} \tag{9.11}$$

where in the last term we replaced, at leading order in $\theta$, $\Gamma_\rho \simeq \lambda_\phi\,m_\rho/(16\pi)$. We assume for simplicity $M_\pm \gtrsim 2$ GeV. Notice that in this case, the annihilation cross section, for fixed $\lambda_\phi$, does not depend on $m_\rho$.

The corresponding lower limits in $|\kappa|$ and $|\sin\theta|$ now result:

$$|\kappa| \;\gtrsim\; \frac{2 \times 10^3}{\lambda_\phi}\frac{m_h^2}{m_{\mathrm{Pl}}^{1/2}\,m_\mu^{3/2}}\,, \qquad |\sin\theta| \;\gtrsim\; 2.8 \times 10^{-4}\,\lambda_\phi^{-3/2}\left(\frac{m_\rho}{0.1\,\mathrm{GeV}}\right)\,. \tag{9.12}$$

Combining the previous bound with the upper limit given by the invisible decay width of the Higgs, we get that the two bounds are consistent only for a non-perturbative value of $\lambda_\phi$. Therefore, we conclude that the Goldstone bosons cannot play the role of a dark radiation for $m_\rho \gtrsim 4$ GeV, regardless of the value of $\Gamma_\rho$.

**Regime II: $2\,m_\mu \lesssim m_\rho \lesssim 4$ GeV**

In this mass range the thermal annihilation cross section is resonantly enhanced due to the fact that the annihilation proceeds via s-channel (see Fig. 9.2) and the typical center of mass energies contributing to the integral in (9.5) are close to the $\rho$ mass. In particular, in the case of a narrow resonance, that is $(\Gamma_\rho/m_\rho)^2 \ll 1$, we can safely approximate

$$\frac{1}{\pi}\,\frac{\Gamma_\rho\,m_\rho}{(s-m_\rho^2)^2 + \Gamma_\rho^2\,m_\rho^2} \;\to\; \delta(s - m_\rho^2)\,. \tag{9.13}$$

In this case the integral in (9.5) is easily computed and we obtain an analytic expression of the averaged annihilation cross section in the given mass range:

$$
\begin{aligned}
\langle\sigma v\rangle_{\eta\eta\to\mu^+\mu^-} &= \frac{\kappa^2}{256}\,\frac{m_\mu^2\,m_\rho^6}{T^5\,m_h^4\,\Gamma_\rho}\left(1 - \frac{4\,m_\mu^2}{m_\rho^2}\right)^{3/2} K_1(m_\rho/T) \\
&= \frac{\kappa^2\,\pi}{16}\,\frac{m_\mu^2\,m_\rho^5}{T^5\,m_h^4\,\lambda_\phi}\left(1 - \frac{4\,m_\mu^2}{m_\rho^2}\right)^{3/2} K_1(m_\rho/T)\,.
\end{aligned}
\tag{9.14}
$$

As we did above, we impose $T = T_\eta^d \simeq m_\mu$ and we derive the minimum value of $\kappa$ for which the Goldstone bosons may contribute to the effective number of relativistic neutrinos. Indeed, taking into account Eq. (9.14) we obtain

$$|\kappa| \;\gtrsim\; 17\,\frac{m_h^2\,\lambda_\phi^{1/2}}{m_{\rm Pl}^{1/2}\,m_\mu^{3/2}\,F(m_\rho/m_\mu)} \;>\; 5.3\,\frac{m_h^2\,\lambda_\phi^{1/2}}{m_{\rm Pl}^{1/2}\,m_\mu^{3/2}} \;\approx\; 7\times 10^{-4}\,\lambda_\phi^{1/2}\,, \tag{9.15}$$

with $F(w) \equiv w\,(w^2 - 4)^{3/4}\,K_1(w)^{1/2}$. In the second inequality we report the least stringent bound, which corresponds to $m_\rho = 5.0\,m_\mu \simeq 525$ MeV, where the function $F(m_\rho/m_\mu)$ is maximized. The corresponding lower bound of $|\sin\theta|$ is independent of the quartic coupling $\lambda_\phi$ and is given by

$$|\sin\theta| \;\gtrsim\; 17\,\frac{v_H\,m_\rho}{\sqrt{2\,m_\mu\,m_{\rm Pl}}\,F(m_\rho/m_\mu)\,m_\mu} \;>\; 3\times 10^{-6}\,, \tag{9.16}$$

where the minimum is obtained at $m_\rho = 3.7\,m_\mu \simeq 390$ MeV. We report in Fig. 9.3 the limit on $|\sin\theta|$ obtained using the analytic expression of the thermal annihilation cross section given in Eq. (9.14) (thick dashed line). We can see that the analytic expression describes precisely the numerical lower bound.

**Regime III: $m_\mu \lesssim m_\rho \lesssim 2\,m_\mu$**

In this case, at $T = T_\eta^d \approx m_\mu$ a fraction of the Goldstone bosons might have enough kinetic energy to produce $\rho$ particles. Consequently, the latter are still present in the thermal bath and the Boltzmann equation (9.4), strictly speaking, is not appropriate to describe the $\eta$ decoupling. In order to account for that effect, the cross section in Eq. (9.7) should also include annihilation of $\rho$ scalars into $\mu^\pm$ pairs. Nevertheless, such process is phase space suppressed at these temperatures

and as a result we can still use Eq. (9.7) to estimate a lower bound of the quartic coupling $\kappa$. Under this assumption, the thermal annihilation cross section is independent of $m_\rho$ and takes the form:

$$\langle \sigma v \rangle_{\eta\eta \to \mu^+ \mu^-} \quad \simeq \quad \frac{\kappa^2}{128\,\pi} \frac{m_\mu^2}{m_h^4} \int_{2\,m_\mu/T}^{\infty} w^4\, K_1(w)\, \mathrm{d}w \,, \tag{9.17}$$

and

$$|\kappa| \quad \gtrsim \quad \frac{40\,m_h^2}{m_\mu^{3/2}\, m_{\mathrm{Pl}}^{1/2}} \quad \approx \quad 5 \times 10^{-3} \,, \tag{9.18}$$

$$|\sin\theta| \quad \gtrsim \quad 8 \times 10^{-4} \left( \frac{v_\phi}{10\,\mathrm{GeV}} \right) \quad = \quad 5.7 \times 10^{-6}\, \lambda_\phi^{-1/2} \left( \frac{m_\rho}{0.1\,\mathrm{GeV}} \right) \,. \tag{9.19}$$

Notice that in this case the lower limit on $|\sin\theta|$ is compatible with the corresponding upper bound obtained from the invisible decay width of the Higgs boson, Eq. (7.22).

## 9.3 Interplay with Direct Detection Limits

**Model II** The results derived in section 7.3 can be applied to find the regions of the parameter space that allow for Goldstone bosons as dark radiation and that are compatible with the negative searches of present dark matter direct detection experiments. On the one hand, the requirement of producing the correct $N_{\mathrm{eff}}$, together with the requirement of perturbativity $\lambda_\phi < 4\pi$, gives a lower limit on $|\sin\theta|$ as a function of $m_\rho$, *cf.* Fig. 9.3. On the other hand, for thermally produced dark matter particles, the LUX experiment sets an upper limit on $|\sin\theta|$ as a function of $m_\rho$, as long as $m_\rho \lesssim 0.8\,M_-$, *cf.* Fig. 7.6. Therefore, only some windows for $|\sin\theta|$ are allowed from the requirement of Goldstone as dark radiation and the non-observation of a signal at LUX.

For illustration, we show this window in Fig. 9.4 for a dark matter mass of 25 GeV, highlighting the values of $m_\rho$ where both limits coincide (dashed lines), which define the allowed (white) and excluded regions (gray).

By applying the same procedure we calculate the allowed regions of $m_\rho$ (red thick lines) for dark matter masses in the range 10 GeV and 1000 GeV; the result is shown in Fig. 9.5, where we shaded in light red the areas excluded by LUX. For comparison we also show in dark red the regions excluded by the XENON100 experiment. The cyan area, $m_\rho > 4$ GeV, corresponds to the regime I discussed in section 9.2, for which it is not possible to have dark radiation due to the upper bound on $\theta$ from the invisible Higgs decay width. Again, close to the Higgs boson resonance (gray band) the limits previously derived do not apply.
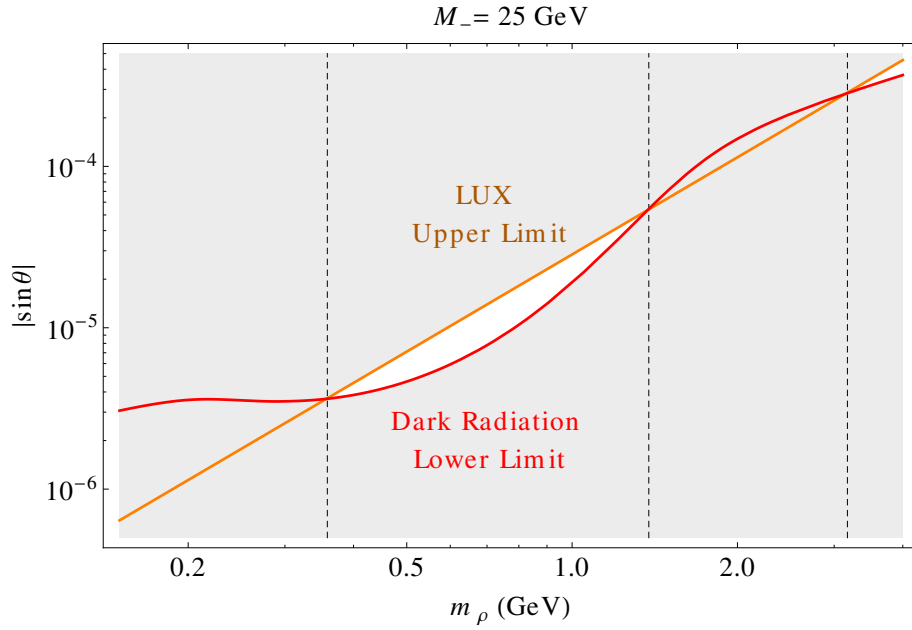
Figure 9.4: Allowed region of $m_\rho$ (white areas) consistent with both the dark radiation hypothesis and the LUX limits for a dark matter mass of 25 GeV.
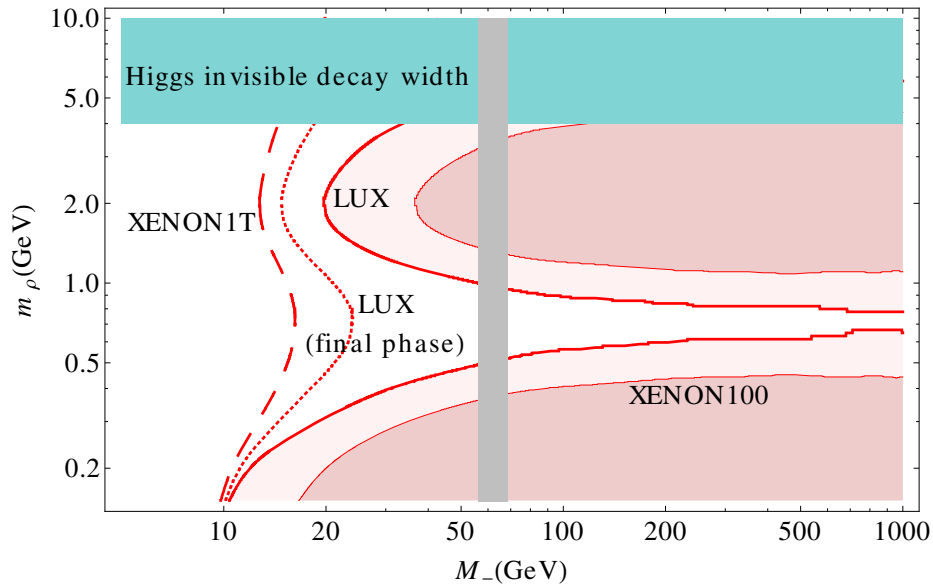


Figure 9.5: Excluded regions of $m_\rho$ as a function of the dark matter mass for Model II under the hypothesis of Goldstone bosons as dark radiation and thermally produced dark matter. The dotted and dashed lines are the projected bounds from the final phase of the LUX and XENON1T experiments, respectively. We do not include in the analysis the Higgs resonance region (gray band).
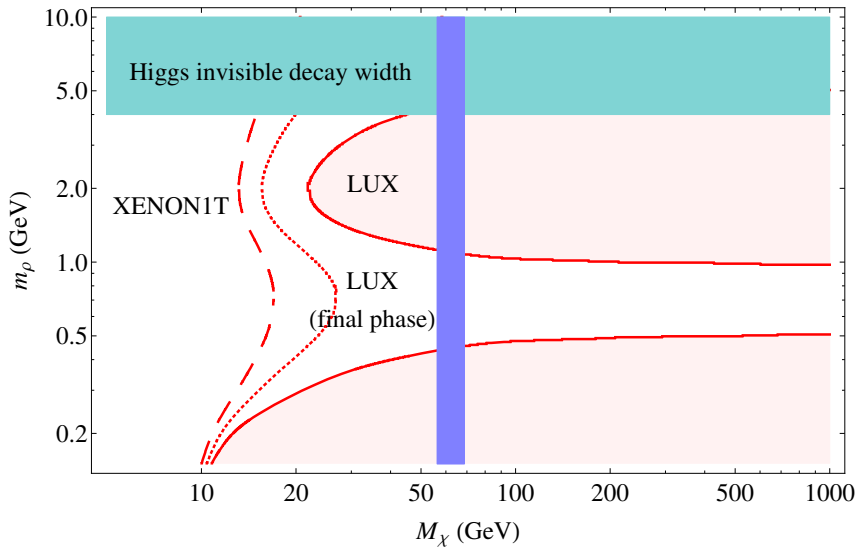
Figure 9.6: Excluded regions for Model III in the long-lived pseudo-Goldstone scenario from the LUX experiment and the invisible Higgs decay width, under the assumption that the dark matter particle was thermally produced and that the pseudo-Goldstone boson contributes to the effective number of neutrino species before recombination. The dotted and dashed lines are the projected bounds from the final phase of the LUX and XENON1T experiments, respectively. We do not include in the analysis the Higgs resonance region (blue band).

For dark matter masses larger than 100 GeV, dark radiation is allowed for $0.5$ GeV $\lesssim m_\rho \lesssim$ $0.9$ GeV. This case corresponds to the regime II for which Goldstone annihilation into $\mu^\pm$ pairs is resonantly enhanced, thus allowing for $|\sin\theta|$ values that can evade the LUX bound, for any dark matter mass. This region is shown in the plot as the "throat" at $0.5$ GeV $\lesssim m_\rho \lesssim 0.9$ GeV. Besides, for $M_- \lesssim 19$ GeV the upper bound on $m_\rho$ given by direct detection disappears, making masses as large as 4 GeV possible. We also report in Fig. 9.5 the corresponding prospects for the direct detection experiments LUX (final phase) [149] and XENON1T [150]. It is remarkable that a large part of the parameter space will be probed by these two experiments. In the former case, dark matter masses larger than about 25 GeV could be excluded, whereas in the latter it would be possible to exclude masses even as low as 15 GeV.

**Model III**   As for Model II, we search for allowed windows of $|\sin\theta|$ and translate them into allowed regions in the plane $m_\rho$ and $M_\chi$. The allowed regions are shown in Fig. 9.6, being the pink areas excluded by the LUX experiment and the cyan area by the upper limit on $|\theta|$ from the invisible Higgs decay width. Notice that close to the Higgs boson resonance (blue band) the limits previously derived do not apply and therefore we remove that region from our analysis. We also report in Fig. 9.6 the corresponding prospects for the direct detection experiments

LUX (final phase) [149] and XENON1T [150]. For $M_\chi \gtrsim 100$ GeV, dark radiation is possible if $0.5$ GeV $\lesssim m_\rho \lesssim 1$ GeV. It is remarkable that a significant portion of the parameter space will be probed both by the LUX (final phase) and XENON1T experiments. For the former case, $M_\chi \gtrsim 25$ GeV might be probed, while for the latter it would be possible to probe dark matter masses as low as 15 GeV.

# Chapter 10

# Gamma-Ray Spectral Features from Short-lived Pseudo-Goldstone Bosons

The scenario introduced in chapter 8, which we called model III, predicts that dark matter particles might be annihilating in the center of our galaxy with a non-negligible rate, concretely through the s-wave process $\chi\chi \to \eta\rho$, if kinematically allowed. This is in contrast to model II, which was introduced in chapter 7, where all the annihilation channels are p-wave suppressed. Therefore, model III might lead to observable signatures in indirect dark matter search experiments. We discuss such signatures in this chapter.

## 10.1 Gamma-Ray Boxes

Following the discussion in Section 8.3 and to allow kinematically this annihilation process, we will assume in what follows that $r < 1.5$.

The pseudo-Goldstone bosons produced in the annihilations $\chi\chi \to \rho\eta$ decay in flight into two photons well before reaching the earth, as follows from Fig. 8.6, thus generating a gamma-ray flux with a characteristic spectrum. In the center of mass frame of the annihilating dark matter particles, the energies of the $\rho$ and pseudo-Goldstone bosons are

$$E_\rho = M_\chi \left( 1 + \frac{m_\rho^2 - m_\eta^2}{4M_\chi^2} \right) \qquad \text{and} \qquad E_\eta = M_\chi \left( 1 - \frac{m_\rho^2 - m_\eta^2}{4M_\chi^2} \right) . \tag{10.1}$$

whereas the energy of the photons is

$$E_\gamma(\alpha) = \frac{m_\eta^2}{2E_\eta \left( 1 - \cos\alpha \sqrt{1 - \frac{m_\eta^2}{E_\eta^2}} \right)} , \tag{10.2}$$

where $\alpha$ is the angle between the pseudo-Goldstone boson and the emitted photons in the annihilation frame. In the rest frame of the pseudo-scalar $\eta$ the photons are emitted isotropically, therefore the energy distribution in the galactic frame displays a characteristic box-shaped spectrum [113], centered at $E_c \equiv (E(0) + E(\pi))/2$ and with width $\Delta E \equiv E(0) - E(\pi)$, which are given by

$$E_c = \frac{1}{2} E_\eta \approx \frac{M_\chi}{2} \left( 1 - \frac{r^2}{4} \right) \qquad \text{and} \qquad \Delta E = \sqrt{E_\eta^2 - m_\eta^2} \approx M_\chi \left( 1 - \frac{r^2}{4} \right) , \tag{10.3}$$

where we assume that $m_\eta \ll m_\rho$ and $r = m_\rho/M_\chi$. Namely, the center of the box is located at half the energy of the pseudo-Goldstone boson, whereas the width is given by its momentum. Besides, the dark $CP$ even scalar decays $\rho \to \eta\eta$ thus producing another contribution to the gamma-ray flux from the subsequent decay $\eta \to \gamma\gamma$. This contribution arises at lower energies, where the background is stronger, and therefore will be neglected in our analysis. The relevant part of the photon spectrum is then:

$$\frac{dN_\gamma}{dE_\gamma} = \frac{2}{\Delta E}\Theta\left(E_\gamma - E_c + \frac{1}{2}\Delta E\right)\Theta\left(E_c + \frac{1}{2}\Delta E - E_\gamma\right)\mathrm{Br}\left(\eta \to \gamma\gamma\right) \tag{10.4}$$

and the gamma-ray flux given by Eq. (2.15) is

$$\frac{d\Phi_\gamma}{dE_\gamma} = \frac{\langle\sigma v(\chi\chi \to \rho\eta)\rangle}{8\,\pi\,M_\chi^2}\frac{dN_\gamma}{dE_\gamma}\frac{1}{\Delta\Omega}\int_{\Delta\Omega} d\Omega\, J_{\mathrm{ann}}\,. \tag{10.5}$$

## 10.2 Fermi-LAT Limits on Model III

The dark matter coupling $f$ can then be constrained from searches of a box feature in the cosmic gamma-ray energy spectrum. We use the limits derived in [113] (intermediate approach), based on observations by the Fermi-LAT of the gamma ray flux from the galactic center. Those limits, derived assuming dark matter annihilation into two scalar particles of the same mass, can be appropriately adapted to our model by replacing $\langle\sigma v\rangle \to \langle\sigma(\chi\chi \to \rho\eta)v\rangle(1 - r^2/4)^2/2$ and $m_{\mathrm{DM}} \to M_\chi(1 - r^2/4)$.

We report in Fig. 10.1 the upper bound on $f$, normalized to the values of $f$ which allow for thermal production of dark matter, given in Eq. (8.17). In the plot we assume $\mathrm{Br}(\eta \to \gamma\gamma) = 1$, $x_f = 20$ and we vary $r$ between 0.1 and 1.5 (gray area). Furthermore, we highlight in blue, orange and green the bound for $r = 0.1, 1$ and 1.5 respectively. The blue shaded area corresponds to the Higgs boson resonance, around which Eq. (8.17) does not apply for sizable values of the mixing angle $\theta$. We then conclude that, under the assumption of thermal dark matter production and of the pseudo-Goldstone boson decaying dominantly into a pair of photons, dark matter masses below $\sim 55\,\mathrm{GeV}$ are excluded by the Fermi data.
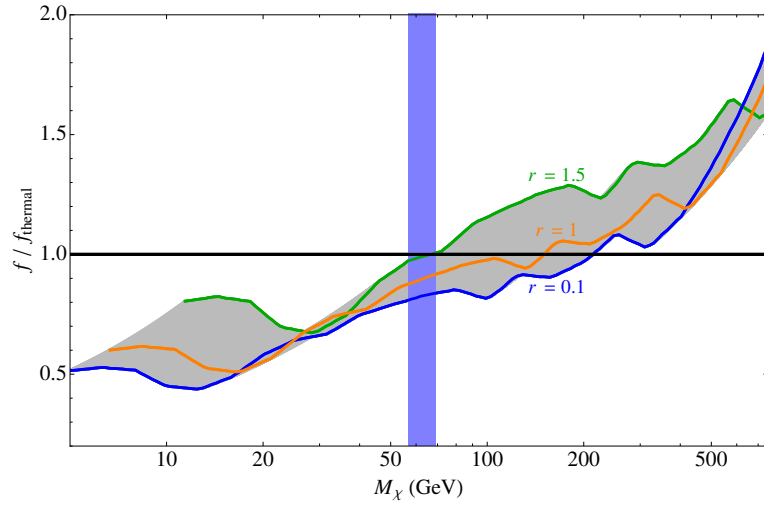
Figure 10.1: Upper bound on the coupling constant $f$ as a function of the dark matter mass from the negative searches of gamma-ray boxes in the Fermi-LAT data, normalized to the value required to thermally produce the dark matter particles. We assume in the plot $\mathrm{Br}(\eta \to \gamma\gamma) = 1$, $x_f = 20$ and vary $r$ between 0.1 and 1.5 (gray area). We do not include in the analysis the Higgs resonance region (blue band).
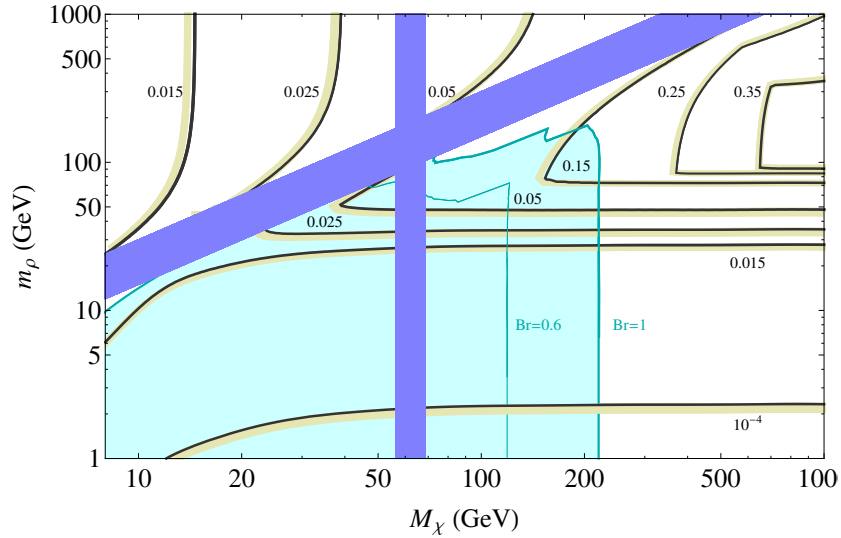


Figure 10.2: Contours with the upper limit on the absolute value of the mixing angle $|\theta|$ in the short-lived pseudo-Goldstone scenario from the LUX experiment and the Higgs invisible decay width, under the assumption that the dark matter particle was thermally produced. The areas shaded in cyan are excluded by searches of gamma-ray boxes assuming $\mathrm{Br}(\eta \to \gamma\gamma) = 0.6$ and 1. We do not include in the analysis the threshold and resonance regions (dark blue bands).

We summarize in Fig. 10.2 the impact of the various limits on the parameter space of this scenario under the assumption that the dark matter population in our Universe was thermally produced. Under this assumption the dark matter coupling $f$ is determined by Eq. (8.17) and hence the parameter space of the model is spanned by the three parameters $M_\chi$, $m_\rho$ and $\theta$. We show in the $m_\rho$-$M_\chi$ plane the upper limit on $|\theta|$ (black lines) inferred from the LUX results and the invisible Higgs decay width (see Fig. 8.1). Namely, points within a given region can not have a value of the mixing angle larger than the one indicated by the corresponding label (the interior of a given region is specified by the shaded contour). Besides, the excluded regions from gamma-ray box searches are shown in cyan for the branching ratios $\mathrm{Br}(\eta \to \gamma\gamma) = 0.6$ and 1. Lastly, we remove the resonance and threshold regions, shown as dark blue bands, where the dark matter coupling $f$ cannot be univocally determined. It is remarkable that the combination of both direct and indirect detection experiments can probe, and possibly exclude, a large portion of the parameter space of the model for light $CP$ even dark scalars, concretely when $m_\rho \lesssim 1.5 M_\chi$. On the other hand, when $m_\rho \gtrsim 3 M_\chi$ the kinematically accessible dark matter annihilation channels are all p-wave suppressed leading to no observable signature in indirect dark matter searches. In this region of the parameter space, however, signals could be detected in direct dark matter searches or in the invisible Higgs decay width.

**Part IV**

# Conclusions

# Conclusions

The high-mass regime of the IDM was studied, namely for dark matter masses greater than $500\,\mathrm{GeV}$. This scenario is our model I. In particular, we calculated the contribution to the gamma-ray spectrum coming from dark matter annihilations into $\gamma\gamma$ and $\gamma Z$. It was found that the corresponding one-loop cross sections violate perturbative unitarity. The origin of this anomaly was to found to be related to the long-range interaction that arises between the annihilation particles due to the exchange of gauge bosons. We argued that the proper solution to this problem is to account for this effect by multiplying the annihilation amplitude by the so-called Sommerfeld enhancement factors. We developed a formalism in order to calculate this in a gauge-invariant manner. Furthermore, it was shown that besides monochromatic photons, the gamma-ray spectra of dark matter annihilations also include virtual internal bremsstrahlung features coming from the process $H^0 H^0 \to W^+ W^- \gamma$, which naturally emerge in the high-mass regime of the IDM. Subsequently, we constructed a series of benchmark points exhibiting an overall spectral feature with an intensity which is one order of magnitude below the H.E.S.S. limits on this class of photon line-like signatures. The benchmarks are compatible with all theoretical and experimental constraints on the IDM. Future searches for gamma-ray spectral features by DAMPE, GAMMA-400 or CTA will continue closing in on the parameter space of the inert doublet dark matter model.

Likewise, two more dark matter scenarios, called model II and III, were studied. In both of them, the stability of the dark matter particle is attributed to the residual $Z_2$ symmetry that arises from the spontaneous breaking of a global $U(1)$ symmetry. We argued that the scalar sector responsible for the symmetry breaking plays a central role in the thermal production of dark matter.

The key difference between both scenarios is that in model II dark matter annihilations proceed via p-waves, whereas for model III annihilations into the $CP$ even dark scalar and the (pseudo-)Goldstone boson proceed in the s-wave. Furthermore, we argued that the existence of a s-wave annihilation channel is due to the explicit $C$ and $P$ breaking induced by a chiral fermion in model III.

The dark sector in these models communicate with the Standard Model via the Higgs portal. As a result, after the spontaneous breaking of the electroweak symmetry and the dark global $U(1)$ symmetry, a mixing term arises between the Standard Model Higgs boson and the dark sector $CP$-even scalar. The Higgs phenomenology is accordingly modified and in particular the invisible Higgs decay width, since new decay channels into dark sector particles are possible. Besides, the mixing induces the scattering of dark matter particles with nucleons, thus opening

the possibility of observing signatures of this model in direct dark matter search experiments. Working under the reasonable assumption that the dark matter particle was thermally produced in the early Universe, we found a stringent upper limit on the mixing angle as a function of the mass of the dark $CP$-even scalar from the negative searches by the LUX experiment.

The massless Goldstone boson predicted by this model is, as recently remarked by Weinberg, an excellent candidate of dark radiation that could account for the exotic contribution to the effective number of neutrinos hinted by various experiments, provided the Goldstone bosons were in thermal equilibrium with the Standard Model particles until the era of muon annihilation. We reevaluated, using the exact expression of the thermal annihilation cross section into $\mu^+\mu^-$, the values of the model parameters necessary to reproduce the central value of $N_{\text{eff}}$. We then derived a lower limit on the mixing angle as a function of the mass of the dark $CP$-even scalar from the requirement of perturbativity of the quartic couplings of the model. Lastly, we combined the upper limit on the mixing angle which follows from the LUX experiment with the lower limit imposed by the requirement of dark radiation and we found large regions of the parameter space where both requirements are incompatible. The final phase of LUX and the future XENON1T experiment will continue closing in on the parameter space of the model and will be able to rule out the possibility that the Goldstone boson contributes sizably to $N_{\text{eff}}$ if the dark matter mass is larger than $\sim 25$ GeV.

Subsequently, we focused on the case in which the global $U(1)$ symmetry is not exact, hence the Goldstone boson is massive and decays into two photons. The mass and lifetime of the pseudo-Goldstone boson are constrained by various experiments. There are at present two allowed windows, one with a lifetime longer than $\sim 10^{20}$ years and one with a lifetime shorter than one minute. We analyzed the experimental signatures of the pseudo-Goldstone bosons in those two windows and analyzed the interplay with the limits from thermal production, the invisible Higgs decay width and direct dark matter searches. In the former scenario, the pseudo-Goldstone boson is a candidate of dark radiation, as in the case of exact $U(1)$ symmetry. On the other hand, in the latter scenario, for model III, s-wave dark matter annihilations in the galactic center produce, if kinematically allowed, an intense gamma-ray flux displaying a box-shaped spectrum. We determined the limits on this scenario from the Fermi-LAT data and found that, if the $CP$-even scalar is much lighter than the dark matter, gamma-ray measurements exclude dark matter masses below 220 GeV (120 GeV) when $\text{Br}(\eta \to \gamma\gamma) = 1$ (0.6).

# Appendix A

# Dark Matter (Co-)Annihilations and the $C$, $P$ and $CP$ Symmetries

In order to study dark matter (co-)annihilations, in this Appendix we consider how pair of particles transform under parity and charge conjugation. Suppose that 1 and 2 are particles with the sh same spin but not necessarily identical. A two-particle state $|12\rangle$ with definite orbital angular momentum $L$ and total spin $S$ is given by

$$|12\rangle = \int \frac{d^3p_1}{(2\pi)^3\sqrt{2E_1}} \frac{d^3p_2}{(2\pi)^3\sqrt{2E_2}} \chi^{L,S}_{\sigma_1,\sigma_2}(\boldsymbol{p_1},\boldsymbol{p_2}) a_1^\dagger(\boldsymbol{p_1},\sigma_1) a_2^\dagger(\boldsymbol{p_2},\sigma_2)|0\rangle, \tag{A.1}$$

where $\sigma_i$ and $\boldsymbol{p_i}$ are the spin along a particular direction and the three-momentum of the particle $i$ and $a_i^\dagger(\boldsymbol{p_i},\sigma_i)$ is the corresponding annihilation operator. Likewise, $\chi^{L,S}_{\sigma_1,\sigma_2}(\boldsymbol{p_1},\boldsymbol{p_2})$ is the wave-function associated to the state $|12\rangle$.

**Transformation under** $P$ : Suppose that the $P-$parity of the particle $i$ is $\lambda_{iP}$, that is, that $P a_i^\dagger(\boldsymbol{p},\sigma) P^{-1} = \lambda_{iP} a_i^\dagger(-\boldsymbol{p},\sigma)$. Then the action of $P$ under the pair of particles 1 and 2 is given by

$$P|12\rangle = \lambda_{1P}\lambda_{2P} \int \frac{d^3p_1}{(2\pi)^3\sqrt{2E_1}} \frac{d^3p_2}{(2\pi)^3\sqrt{2E_2}} \chi^{L,S}_{\sigma_1,\sigma_2}(-\boldsymbol{p_1},-\boldsymbol{p_2}) a_1^\dagger(\boldsymbol{p_1},\sigma_1) a_2^\dagger(\boldsymbol{p_2},\sigma_2)|0\rangle, \tag{A.2}$$

hence

$$P|12\rangle = \lambda_{1P}\lambda_{2P}(-1)^L|12\rangle. \tag{A.3}$$

When the particle 2 is the antiparticle of 1, that is if $2 = \bar{1}$, the $P-$parities are related to each other [151]. In fact, it is well-known that $\lambda_{\bar{i}P} = (-1)^F \lambda_{iP}^*$, where $F$ is 1 for fermions and 0 for bosons. As a result

$$P|1\bar{1}\rangle = (-1)^{L+F}|1\bar{1}\rangle. \tag{A.4}$$

**Transformation under** $C$**:** Suppose that the $C-$parity of the particle $i$ is $\lambda_{iC}$. Then

$$C|12\rangle = \lambda_{1C}\lambda_{2C}|\bar{1}\bar{2}\rangle. \tag{A.5}$$

| State | $C$ | $P$ | $CP$ |
|:---:|:---:|:---:|:---:|
| $\rho,\ H^0$ | 1 | 1 | 1 |
| $\eta,\ A^0$ | $-1$ | 1 | $-1$ |
| $\psi_-$ | 1 | $i$ | $i$ |
| $\psi_+$ | $-1$ | $i$ | $-i$ |
| $\chi$ | Broken | Broken | $i$ |
| $\rho\rho,\ \eta\eta\ ,\ H^0H^0,\ A^0A^0$ | 1 | $(-1)^L$ | $(-1)^L$ |
| $\eta\rho,\ H^0A^0$ | $-1$ | $(-1)^L$ | $(-1)^{L+1}$ |
| $\psi_\pm\psi_\pm$ | 1 | $(-1)^{L+1}$ | $(-1)^{L+1}$ |
| $\psi_\pm\psi_\mp$ | $-1$ | $(-1)^{L+1}$ | $(-1)^L$ |
| $\chi\chi$ | Broken | Broken | $(-1)^{L+1}$ |
| $f\bar{f}$ | $(-1)^{L+S}$ | $(-1)^{L+1}$ | $(-1)^{S+1}$ |

Table A.1: $C, P$ and $CP$ phases of the self-conjugate particles and the two-particle states of the models considered in this work. Here $f$ is any fermion of the Stadanrd Model.

It is well-known that the C-parity phases satisfy $\lambda_{\bar{i}P} = \lambda_{iP}^*$ [151]. In particular, if the particle 2 is the antiparticle of 1, then $C|1\bar{1}\rangle = |\bar{1}1\rangle$. Now, under the exchange of the particles 1 and 2 the wave-function transforms as

$$\chi_{\sigma_1,\sigma_2}^{L,S}(\boldsymbol{p_1},\boldsymbol{p_2}) = (-1)^{L+S+F}\chi_{\sigma_2,\sigma_1}^{L,S}(\boldsymbol{p_2},\boldsymbol{p_1})\,. \tag{A.6}$$

This expression, Eq. (A.1) and the Pauli exclusion principle can be used to prove that

$$|21\rangle = (-1)^{L+S}|12\rangle, \tag{A.7}$$

and therefore

$$C|1\bar{1}\rangle = (-1)^{L+S}|1\bar{1}\rangle. \tag{A.8}$$

Another consequence of Eq. (A.7) is that a pair of identical particles must satisfy

$$(-1)^{L+S} = 1\,. \tag{A.9}$$

For example, a pair of Majorana fermions in the s-wave state must have total spin zero. If the particle 1 is self conjugate, the last two equations also imply that

$$C|11\rangle = |11\rangle. \tag{A.10}$$

The same relation holds when the particle 1 is self-conjugate.

All the previous expressions can be used to calculate the transformations properties under $C$, $P$ and $CP$ of the self-conjugate particles and the two-particle states of the models considered in this work. This is shown in table A.1.

# Appendix B

# Cross Sections

## Model I

Here we consider expressions for the VIB process $H^0 H^0 \to W^+ W^- \gamma$. The total differential velocity weighted annihilation cross section can be cast as

$$\frac{d(\sigma v)_{W^+ W^- \gamma}}{dx} = \frac{d(\sigma v)}{dx}\bigg|_{\text{Gauge}} + \frac{d(\sigma v)}{dx}\bigg|_{\text{Quartic}} + \frac{d(\sigma v)}{dx}\bigg|_{\text{Interference}} , \tag{B.1}$$

with

$$\frac{d(\sigma v)}{dx}\bigg|_{\text{Gauge}} = -\frac{e^2 g^4}{128\pi^3 M_{H^0}^2 (1-2\mu)^3} \tag{B.2}$$

$$\times \left[ \left( \frac{2 - 4x + 6x^2 - 4x^3 + x^4 - 10\mu + 16x\mu - 20x^2\mu + 8x^3\mu + 16\mu^2 - 20x\mu^2 + 18x^2\mu^2 - 8\mu^3 + 8x\mu^3}{(2 - x - 4\mu)^2 \, (1 - 2x + x^2 - 4\mu + 6x\mu - x^2\mu + 4\mu^2 - 4x\mu^2)} \right. \right.$$

$$+ \frac{1 + x^2 - 4\mu + 6\mu^2}{x^2(1-\mu)} \bigg) x(1-x)(1-\mu)(1-2\mu)A(x)$$

$$+ \frac{1}{x(1-x-2\mu)} \left( x^4 - 2x^3(1-2\mu)(1-\mu) + x^2(3-4\mu)\left(1 - 4\mu + 6\mu^2\right) \right.$$

$$\left. -2x(1-2\mu)^2\left(1 - 4\mu + 6\mu^2\right) + (1-2\mu)^3\left(1 - 4\mu + 6\mu^2\right) \right) B(x)$$

$$+ \frac{1}{(2-x-4\mu)^3(1-x-2\mu)} \left( x^6 - 2x^5(1-2\mu)(4-\mu) - 2x^4(-12 + 53\mu - 71\mu^2 + 24\mu^3) \right.$$

$$-4x^3(9 - 57\mu + 136\mu^2 - 142\mu^3 + 52\mu^4) - 2x^2(1-2\mu)^2(-14 + 54\mu - 87\mu^2 + 46\mu^3)$$

$$\left. \left. -4x(-1+2\mu)^3(-3 + 8\mu - 13\mu^2 + 6\mu^3) + 4(1-2\mu)^4(1 - 2\mu + 3\mu^2) \right) C(x) \right] , \tag{B.3}$$

$$\frac{d(\sigma v)}{dx}\bigg|_{\text{Quartic}} = \frac{32 e^2 M_{H^0}^2 \lambda_3^2}{128\pi^3 \left( 4M_{H^0}^2 - M_h^2 \right)^2}$$

$$\times \left[ -\left( \frac{1-x}{x} \right)\left(1 - 2x^2 - 4\mu + 12\mu^2\right) A(x) + \left( \frac{1-x-2\mu}{x} \right)\left(1 - 4\mu + 12\mu^2\right) B(x) \right] , \tag{B.4}$$

$$\frac{d(\sigma v)}{dx}\bigg|_{\text{Interference}} = \frac{16e^2 g^2 \lambda_3 \mu}{128\pi^3 \left(4M_{H^0}^2 - M_h^2\right)} \left[ -3 \left(\frac{1-x}{x}\right) A(x) \right.$$

$$+ \left(\frac{x^4 - x^3(7 - 13\mu) - 15x(1 - 2\mu)^3 + 6(1 - 2\mu)^4 + 2x^2 \left(8 - 31\mu + 30\mu^2\right)}{x(2 - x - 4\mu)(1 - 2\mu)(1 - x - 2\mu)}\right) B(x)$$

$$+ \left.\left(\frac{x^3 - (1 - 2\mu)^2 + x^2(-3 + 5\mu) + x \left(2 - 6\mu + 4\mu^2\right)}{(2 - x - 4\mu)(1 - 2\mu)(1 - x - 2\mu)}\right) C(x) \right] , \tag{B.5}$$

where

$$A(x) = \sqrt{1 - \frac{4\mu}{1-x}}, \qquad B(x) = \log\left[\frac{1 + A(x)}{1 - A(x)}\right], \qquad C(x) = \log\left[\frac{2 - x + A(x)x - 4\mu}{2 - x - A(x)x - 4\mu}\right] .$$

## Model II

Here we report the (co)annihilation cross sections of $\psi_\pm$ for an arbitrary center of mass-energy in the limit $\theta = 0$. We introduce for convenience the following notation

$$\omega = \frac{\sqrt{s}}{M_-}, \qquad u(r, w) = (z - 1)^2 \left(\left(\frac{\Gamma_\rho}{m_\rho}\right)^2 r^4 + \left(r^2 - \omega^2\right)^2\right) . \tag{B.6}$$

In terms of these variables, the cross sections are given by

$$\sigma(\psi_- \psi_- \to \eta\eta)(\omega) = \frac{f^4}{64\pi M_-^2 \omega^2 \left(w^2 - 4\right) u(r, w)}$$

$$\left[\frac{\log\left(\frac{\omega^2 - \omega_1^2 + z^2 - 2}{\omega_1^2 + z^2}\right)}{(z - 1)\left(\omega^2 + 2z^2 - 2\right)}\left(4r^4 \left(2\omega^2 + 4z^4 - 2\omega^2 z^3 + 8z^3 + 2\omega^2 z^2 - \omega^4 z + 6\omega^2 z - 8z - 4\right)\right.\right.$$

$$+ 4r^2\omega^2 \left(-2\omega^2 - 4z^4 + 2\omega^2 z^3 - 8z^3 - 2\omega^2 z^2 + \omega^4 z - 6\omega^2 z + 8z + 4\right)$$

$$+ \left.u(r, w)(z - 1)\left(\omega^4 + 6z^4 + 8z^3 + 4\left(2\omega^2 - 3\right)z^2 + 8\left(\omega^2 - 3\right)z - 10\right)\right)$$

$$+ \frac{4\omega_1^2 \left(-r^4\omega^2 + 4r^4 z + 4r^2\omega^2 - 4r^2\omega^2 z + u(r, w)z^2 - 2u(r, w)z + u(r, w)\right)}{(z - 1)^2}$$

$$\left.- \frac{(z + 1)^4 u(r, w)}{\omega_1^2 - \omega^2 - z^2 + 2} - \frac{(z + 1)^4 u(r, w)}{\omega_1^2 + z^2}\right]_{\omega_1 = \sqrt{\frac{w^2}{4} - 1 + \frac{w}{2}}}^{\omega_1 = \sqrt{\frac{w^2}{4} - 1 - \frac{w}{2}}} , \tag{B.7}$$

$$\sigma(\psi_- \psi_- \to \rho\rho)(\omega) = \frac{f^4}{64\pi M_-^2 \omega^2 \left(w^2 - 4\right)}$$

$$\left[\frac{\log\left(\frac{\omega_1^2 + 1}{2r^2 - \omega^2 + \omega_1^2 + 1}\right)}{(z - 1)\left(2r^4 - 3r^2\omega^2 + \omega^4\right)}\left(6r^6(z + 7) - 2r^4 \left(-5\omega^2 + 5\omega^2 z + 8z + 88\right)\right.\right.$$

$$+ \left.r^2 \left(-17\omega^4 + 64\omega^2 + 5\omega^4 z + 32\omega^2 z - 32z + 32\right) + \omega^2 \left(\omega^4 + 16\omega^2 - 32\right)(1 - z)\right)$$

$$
+ \frac{4\omega_1^2 \left(-3r^2\omega + r^2 z + 5r^2 + \omega^2 - \omega^2 z\right) \left(3r^2\omega + r^2 z + 5r^2 + \omega^2 - \omega^2 z\right)}{(z-1)^2 \left(r^2 - \omega^2\right)^2}
$$

$$
\left. - \frac{\left(r^2 - 4\right)^2}{2r^2 - \omega^2 + \omega_1^2 + 1} - \frac{\left(r^2 - 4\right)^2}{\omega_1^2 + 1} \right]_{\omega_1 = \sqrt{\frac{\omega^2}{4} - 1} + \sqrt{\frac{\omega^2}{4} - r^2}}^{\omega_1 = \sqrt{\frac{\omega^2}{4} - 1} - \sqrt{\frac{\omega^2}{4} - r^2}} , \tag{B.8}
$$

$$
\sigma(\psi_- \psi_+ \to \rho\eta)(\omega) = \frac{f^4}{64\pi M_-^2 \left(\omega^2 - (z-1)^2\right)\left(\omega^2 - (z+1)^2\right)}
$$

$$
\left[ - \frac{4r^2(z+1)\left(r^2 + \omega^2 - 2z^2 - 4z - 2\right)}{\omega^2(z-1)} \log\left[\left(1 - \omega_1^2\right)\left(r^2 - \omega^2 - \omega_1^2 + 1\right)\right] \right.
$$

$$
- \frac{2 \log\left(\frac{r^2 - \omega^2 - \omega_1^2 + 1}{1 - \omega_1^2}\right)}{\omega^2(\omega^2 - r^2)} \left(2r^6 - 5r^4\omega^2 + 4r^4 z^2 + 8r^4 z + 4r^4 + 4r^2\omega^4 - 2r^2\omega^2 - 2r^2\omega^2 z^2 \right.
$$

$$
\left. - 4r^2\omega^2 z - \omega^6 - 8\omega^2 z^3 - 16\omega^2 z^2 - 8\omega^2 z\right) + \frac{8r^4\omega_1^2(\omega^2 - (z+1)^2)}{\omega^4(z-1)^2} - \frac{2(z+1)^2(r^2 - 4z^2)}{\omega_1^2 - r^2 + \omega^2 - 1}
$$

$$
\left. - \frac{2\left(r^2 - 4\right)(z+1)^2}{\omega_1^2 - 1} \right]_{\omega_1^2 = \frac{r^2\omega^2 + r^2 z^2 - r^2 - \omega^4 + \omega^2 + \omega^2 z^2 - \left(\omega^2 - r^2\right)\sqrt{(\omega^2 - 1)^2 + z^4 - 2(\omega^2 + 1)z^2}}{2\omega^2}}^{\omega_1^2 = \frac{r^2\omega^2 + r^2 z^2 - r^2 - \omega^4 + \omega^2 + \omega^2 z^2 + \left(\omega^2 - r^2\right)\sqrt{(\omega^2 - 1)^2 + z^4 - 2(\omega^2 + 1)z^2}}{2\omega^2}} , \tag{B.9}
$$

$$
\sigma(\psi_+ \psi_+ \to \eta\eta)(\omega) = \frac{1}{z^2} \sigma(\psi_- \psi_- \to \eta\eta)\left(\frac{\omega}{z}\right)\bigg|_{r \to \frac{r}{z}, z \to \frac{1}{z}} , \tag{B.10}
$$

$$
\sigma(\psi_+ \psi_+ \to \rho\rho)(\omega) = \frac{1}{z^2} \sigma(\psi_- \psi_- \to \rho\rho)\left(\frac{\omega}{z}\right)\bigg|_{r \to \frac{r}{z}, z \to \frac{1}{z}} . \tag{B.11}
$$

## Model III

Here we report the annihilation cross sections of $\chi$ for an arbitrary center of mass energy $\sqrt{s}$ in the limit $\theta = 0$. We introduce for convenience the notation

$$
t = \frac{\sqrt{s}}{M_\chi} , \qquad r = \frac{m_\rho}{M_\chi} , \qquad \gamma_\rho = \frac{\Gamma_\rho}{M_\chi}
$$

and we define the functions

$$
K_{\eta\eta}(t) = \sqrt{-4 + t^2} , \qquad K_{\rho\eta}(r, t) = \sqrt{\frac{\left(r^2 - t^2\right)^2 \left(-4 + t^2\right)}{t^2}} ,
$$

$$
K_{\rho\rho}(r, t) = \sqrt{\left(-4r^2 + t^2\right)\left(-4 + t^2\right)} .
$$

In terms of these definitions, the annihilation cross sections are the following:

$$\sigma\left(\chi\,\chi \to \eta\,\eta\right) = \frac{f^4\left(K_{\eta\eta}(t)\left(r^4t^2 - 4r^2\gamma_\rho^2 - 4t^4\right) - 2\,t\left(-r^4 + r^2\gamma_\rho^2 + t^4\right)\right)\log\left(\frac{t - K_{\eta\eta}(t)}{t + K_{\eta\eta}(t)}\right)}{64\,\pi\,M_\chi^2\,t\,(t^2 - 4)\left(r^2\,\gamma_\rho^2 + (t^2 - r^2)^2\right)}\,,$$

$$\sigma\left(\chi\,\chi \to \rho\,\eta\right) = \frac{f^4\left(r^4 K_{\rho\eta}(r,t) + 2\left(2r^4 - 3r^2t^2 + t^4\right)\log\left(\frac{r^2 - t^2 - K_{\rho\eta}(r,t)}{r^2 - t^2 + K_{\rho\eta}(r,t)}\right)\right)}{32\,\pi\,M_\chi^2\,t^4\,(t^2 - 4)}\,,$$

$$\sigma\left(\chi\,\chi \to \rho\,\rho\right) = \frac{f^4}{128\,\pi\,M_\chi^2\,t^2\,(t^2 - 4)}$$

$$\left(\frac{2\,K_{\rho\rho}(r,t)\left(9r^8\left(t^2 - 2\right) + r^6\left(80 - 48t^2\right) + r^4\left(3t^4 + 16t^2 - 32\right) + 16r^2t^2\left(t^2 + 4\right) - 4t^4\left(t^2 + 8\right)\right)}{\left(r^2 - t^2\right)^2\left(r^4 - 4r^2 + t^2\right)}\right.$$

$$\left. - \frac{4\left(18r^6 + 10r^4\left(t^2 - 8\right) + r^2\left(-11t^4 + 16t^2 + 32\right) + t^2\left(t^4 + 16t^2 - 32\right)\right)\log\left(\frac{t^2 - 2r^2 - K_{\rho\rho}(r,t)}{t^2 - 2r^2 + K_{\rho\rho}(r,t)}\right)}{2r^4 - 3r^2t^2 + t^4}\right)\,.$$

# Acknowledgments

# Bibliography

[1] CMS Collaboration, S. Chatrchyan et al., Phys.Lett. **B716** (2012), 30, `1207.7235`.

[2] ATLAS Collaboration, G. Aad et al., Phys.Lett. **B716** (2012), 1, `1207.7214`.

[3] G. Bertone, D. Hooper, and J. Silk, Phys.Rept. **405** (2005), 279, `hep-ph/0404175`.

[4] L. Bergstrom, Rept.Prog.Phys. **63** (2000), 793, `hep-ph/0002126`.

[5] G. Bertone, *Particle dark matter: Observations, models and searches*, Cambridge University Press, 2010.

[6] N. G. Deshpande and E. Ma, Phys.Rev. **D18** (1978), 2574.

[7] E. Ma, Phys.Rev. **D73** (2006), 077301, `hep-ph/0601225`.

[8] R. Barbieri, L. J. Hall, and V. S. Rychkov, Phys.Rev. **D74** (2006), 015007, `hep-ph/0603188`.

[9] L. Lopez Honorez, E. Nezri, J. F. Oliver, and M. H. Tytgat, JCAP **0702** (2007), 028, `hep-ph/0612275`.

[10] M. Gustafsson, E. Lundstrom, L. Bergstrom, and J. Edsjo, Phys.Rev.Lett. **99** (2007), 041301, `astro-ph/0703512`.

[11] P. Agrawal, E. M. Dolle, and C. A. Krenke, Phys.Rev. **D79** (2009), 015015, `0811.1798`.

[12] S. Andreas, M. H. Tytgat, and Q. Swillens, JCAP **0904** (2009), 004, `0901.1750`.

[13] E. Nezri, M. H. Tytgat, and G. Vertongen, JCAP **0904** (2009), 014, `0901.2556`.

[14] L. Lopez Honorez and C. E. Yaguna, JHEP **1009** (2010), 046, `1003.3125`.

[15] L. Lopez Honorez and C. E. Yaguna, JCAP **1101** (2011), 002, `1011.1411`.

[16] M. Klasen, C. E. Yaguna, and J. D. Ruiz-Alvarez, Phys.Rev. **D87** (2013), 075025, `1302.1657`.

[17] A. Arhrib, Y.-L. S. Tsai, Q. Yuan, and T.-C. Yuan, `1310.0358`.

[18] M. Gustafsson, *Light from Dark Matter*, Ph.D. thesis, Stockholm University, 2008.

[19] A. Sommerfeld, Ann. Phys **11** (1931).

[20] J. Hisano, S. Matsumoto, and M. M. Nojiri, Phys.Rev. **D67** (2003), 075014, `hep-ph/0212022`.

[21] J. Hisano, S. Matsumoto, and M. M. Nojiri, Phys.Rev.Lett. **92** (2004), 031303, `hep-ph/0307216`.

[22] J. Hisano, S. Matsumoto, M. M. Nojiri, and O. Saito, Phys.Rev. **D71** (2005), 063528, `hep-ph/0412403`.

[23] J. Hisano, S. Matsumoto, O. Saito, and M. Senami, Phys.Rev. **D73** (2006), 055004, `hep-ph/0511118`.

[24] M. Cirelli, A. Strumia, and M. Tamburini, Nucl.Phys. **B787** (2007), 152, `0706.4071`.

[25] A. Hryczuk, Phys.Lett. **B699** (2011), 271, `1102.4295`.

[26] R. Iengo, JHEP **0905** (2009), 024, `0902.0688`.

[27] N. Arkani-Hamed, D. P. Finkbeiner, T. R. Slatyer, and N. Weiner, Phys.Rev. **D79** (2009), 015014, `0810.0713`.

[28] H. Baer, K.-m. Cheung, and J. F. Gunion, Phys.Rev. **D59** (1999), 075002, `hep-ph/9806361`.

[29] T. Hambye, PoS **IDM2010** (2011), 098, `1012.4587`.

[30] L. M. Krauss and F. Wilczek, Phys.Rev.Lett. **62** (1989), 1221.

[31] J. Goldstone, Nuovo Cim. **19** (1961), 154.

[32] Y. Nambu, Phys.Rev.Lett. **4** (1960), 380.

[33] J. Goldstone, A. Salam, and S. Weinberg, Phys.Rev. **127** (1962), 965.

[34] S. Weinberg, Phys.Rev.Lett. **110** (2013), no. 24, 241301, `1305.1971`.

[35] Planck Collaboration, P. Ade et al., `1303.5076`.

[36] C. Garcia-Cely and A. Ibarra, JCAP **1309** (2013), 025, `1306.4681`.

[37] C. Garcia-Cely, A. Ibarra, and E. Molinaro, JCAP **1311** (2013), 061, `1310.6256`.

[38] C. Garcia-Cely, A. Ibarra, and E. Molinaro, JCAP **1402** (2014), 032, `1312.3578`.

[39] C. Garcia-Cely, M. Gustafsson, and A. Ibarra, to be submitted (2014).

[40] S. Weinberg, *Cosmology*, Cosmology, OUP Oxford, 2008.

[41] E. Hubble, Proceedings of the National Academy of Science **15** (1929), 168.

[42] Supernova Search Team, A. G. Riess et al., Astron.J. **116** (1998), 1009, `astro-ph/9805201`.

[43] Supernova Cosmology Project, S. Perlmutter et al., Astrophys.J. **517** (1999), 565, `astro-ph/9812133`.

[44] Supernova Search Team, A. G. Riess et al., Astrophys.J. **607** (2004), 665, `astro-ph/0402512`.

[45] SNLS Collaboration, P. Astier et al., Astron.Astrophys. **447** (2006), 31, `astro-ph/0510447`.

[46] F. Zwicky, Helvetica Physica Acta **6** (1933), 110.

[47] V. C. Rubin, W. K. J. Ford, and N. . Thonnard, apj **238** (1980), 471.

[48] A. Taylor, S. Dye, T. J. Broadhurst, N. Benitez, and E. van Kampen, `astro-ph/9801158`.

[49] EROS-2 Collaboration, P. Tisserand et al., Astron.Astrophys. **469** (2007), 387, `astro-ph/0607207`.

[50] G. Steigman, Int.J.Mod.Phys. **E15** (2006), 1, `astro-ph/0511534`.

[51] D. Clowe, M. Bradac, A. H. Gonzalez, M. Markevitch, S. W. Randall, et al., Astrophys.J. **648** (2006), L109, `astro-ph/0608407`.

[52] S. D. White, C. Frenk, and M. Davis, Astrophys.J. **274** (1983), L1.

[53] M. Taoso, G. Bertone, and A. Masiero, JCAP **0803** (2008), 022, `0711.4996`.

[54] S. Dodelson and L. M. Widrow, Phys.Rev.Lett. **72** (1994), 17, `hep-ph/9303287`.

[55] T. Falk, K. A. Olive, and M. Srednicki, Phys.Lett. **B339** (1994), 248, `hep-ph/9409270`.

[56] S. Weinberg, Phys.Rev.Lett. **50** (1983), 387.

[57] H. Goldberg, Phys.Rev.Lett. **50** (1983), 1419.

[58] H. Pagels and J. R. Primack, Phys.Rev.Lett. **48** (1982), 223.

[59] J. R. Ellis, J. Hagelin, D. V. Nanopoulos, K. A. Olive, and M. Srednicki, Nucl.Phys. **B238** (1984), 453.

[60] R. Peccei and H. R. Quinn, Phys.Rev.Lett. **38** (1977), 1440.

[61] S. Weinberg, Phys.Rev.Lett. **40** (1978), 223.

[62] F. Wilczek, Phys.Rev.Lett. **40** (1978), 279.

[63] M. Dine, W. Fischler, and M. Srednicki, Phys.Lett. **B104** (1981), 199.

[64] J. E. Kim, Phys.Rev.Lett. **43** (1979), 103.

[65] M. A. Shifman, A. Vainshtein, and V. I. Zakharov, Nucl.Phys. **B165** (1980), 45.

[66] M. Cirelli, N. Fornengo, and A. Strumia, Nucl.Phys. **B753** (2006), 178, `hep-ph/0512090`.

[67] M. Cirelli and A. Strumia, New J.Phys. **11** (2009), 105005, `0903.3381`.

[68] H.-C. Cheng, K. T. Matchev, and M. Schmaltz, Phys.Rev. **D66** (2002), 036005, `hep-ph/0204342`.

[69] G. Servant and T. M. Tait, Nucl.Phys. **B650** (2003), 391, `hep-ph/0206071`.

[70] T. Appelquist, H.-C. Cheng, and B. A. Dobrescu, Phys.Rev. **D64** (2001), 035002, `hep-ph/0012100`.

[71] L. Bergstrom, T. Bringmann, M. Eriksson, and M. Gustafsson, Phys.Rev.Lett. **94** (2005), 131301, `astro-ph/0410359`.

[72] L. Bergstrom, T. Bringmann, M. Eriksson, and M. Gustafsson, JCAP **0504** (2005), 004, `hep-ph/0412001`.

[73] A. Ibarra, D. Tran, and C. Weniger, Int.J.Mod.Phys. **A28** (2013), no. 27, 1330040, `1307.6434`.

[74] E. Kolb and M. Turner, *The early universe*, Frontiers in Physics, Addison-Wesley Longman, Incorporated, 1990.

[75] D. A. Dicus, E. W. Kolb, and V. L. Teplitz, Phys.Rev.Lett. **39** (1977), 168.

[76] B. W. Lee and S. Weinberg, Phys.Rev.Lett. **39** (1977), 165.

[77] M. Srednicki, R. Watkins, and K. A. Olive, Nucl.Phys. **B310** (1988), 693.

[78] P. Gondolo and G. Gelmini, Nucl.Phys. **B360** (1991), 145.

[79] G. Belanger, F. Boudjema, A. Pukhov, and A. Semenov, Comput.Phys.Commun. **185** (2014), 960, `1305.0237`.

[80] K. Griest and D. Seckel, Phys.Rev. **D43** (1991), 3191.

[81] M. W. Goodman and E. Witten, Phys.Rev. **D31** (1985), 3059.

[82] LUX Collaboration, D. Akerib et al., Phys.Rev.Lett. **112** (2014), 091303, `1310.8214`.

[83] J. F. Navarro, A. Ludlow, V. Springel, J. Wang, M. Vogelsberger, et al., `0810.1522`.

[84] E. Hayashi and S. White, `0709.3933`.

[85] L. Gao, J. F. Navarro, S. Cole, C. Frenk, S. D. White, et al., `0711.0746`.

[86] J. F. Navarro, E. Hayashi, C. Power, A. Jenkins, C. S. Frenk, et al., Mon.Not.Roy.Astron.Soc. **349** (2004), 1039, `astro-ph/0311231`.

[87] V. Springel, J. Wang, M. Vogelsberger, A. Ludlow, A. Jenkins, et al., Mon.Not.Roy.Astron.Soc. **391** (2008), 1685, `0809.0898`.

[88] J. F. Navarro, C. S. Frenk, and S. D. White, Astrophys.J. **462** (1996), 563, `astro-ph/9508025`.

[89] J. F. Navarro, C. S. Frenk, and S. D. White, Astrophys.J. **490** (1997), 493, `astro-ph/9611107`.

[90] L. Pieri, J. Lavalle, G. Bertone, and E. Branchini, Phys.Rev. **D83** (2011), 023518, `0908.0195`.

[91] R. Catena and P. Ullio, JCAP **1008** (2010), 004, `0907.0018`.

[92] M. Weber and W. de Boer, Astron.Astrophys. **509** (2010), A25, `0910.4272`.

[93] P. Salucci, F. Nesti, G. Gentile, and C. Martins, Astron.Astrophys. **523** (2010), A83, `1003.3101`.

[94] M. Pato, O. Agertz, G. Bertone, B. Moore, and R. Teyssier, Phys.Rev. **D82** (2010), 023531, `1006.1322`.

[95] L. Bergstrom and H. Snellman, Phys.Rev. **D37** (1988), 3737.

[96] L. Bergstrom and P. Ullio, Nucl.Phys. **B504** (1997), 27, `hep-ph/9706232`.

[97] P. Ullio and L. Bergstrom, Phys.Rev. **D57** (1998), 1962, `hep-ph/9707333`.

[98] Z. Bern, P. Gondolo, and M. Perelstein, Phys.Lett. **B411** (1997), 86, `hep-ph/9706538`.

[99] Y. Mambrini, JCAP **0912** (2009), 005, `0907.2918`.

[100] C. Jackson, G. Servant, G. Shaughnessy, T. M. Tait, and M. Taoso, JCAP **1004** (2010), 004, `0912.0004`.

[101] G. Bertone, C. Jackson, G. Shaughnessy, T. M. Tait, and A. Vallinotto, Phys.Rev. **D80** (2009), 023512, `0904.1442`.

[102] G. Bertone, C. Jackson, G. Shaughnessy, T. M. Tait, and A. Vallinotto, JCAP **1203** (2012), 020, `1009.5107`.

[103] J. F. Beacom, N. F. Bell, and G. Bertone, Phys.Rev.Lett. **94** (2005), 171301, `astro-ph/0409403`.

[104] A. Birkedal, K. T. Matchev, M. Perelstein, and A. Spray, `hep-ph/0507194`.

[105] T. Bringmann, L. Bergstrom, and J. Edsjo, JHEP **0801** (2008), 049, `0710.3169`.

[106] V. Barger, Y. Gao, W. Y. Keung, and D. Marfatia, Phys.Rev. **D80** (2009), 063537, `0906.3009`.

[107] V. Barger, W.-Y. Keung, and D. Marfatia, Phys.Lett. **B707** (2012), 385, `1111.4523`.

[108] T. Bringmann, M. Doro, and M. Fornasa, JCAP **0901** (2009), 016, `0809.2269`.

[109] A. Ibarra, T. Toma, M. Totzauer, and S. Wild, `1405.6917`.

[110] T. Toma, Phys.Rev.Lett. **111** (2013), 091301, `1307.6181`.

[111] C. Arina, T. Hambye, A. Ibarra, and C. Weniger, JCAP **1003** (2010), 024, `0912.4496`.

[112] T. Bringmann, X. Huang, A. Ibarra, S. Vogl, and C. Weniger, JCAP **1207** (2012), 054, `1203.1312`.

[113] A. Ibarra, S. Lopez Gehler, and M. Pato, JCAP **1207** (2012), 043, `1205.0007`.

[114] K. Enqvist, K. Kainulainen, and V. Semikoz, Nucl.Phys. **B374** (1992), 392.

[115] A. Dolgov, Phys.Rept. **370** (2002), 333, `hep-ph/0202122`.

[116] S. Hannestad, Phys.Rev. **D65** (2002), 083006, `astro-ph/0111423`.

[117] J. F. Gunion and H. E. Haber, Phys.Rev. **D67** (2003), 075019, `hep-ph/0207010`.

[118] M. Gustafsson, PoS **CHARGED2010** (2010), 030, `1106.1719`.

[119] I. F. Ginzburg and M. Krawczyk, Phys.Rev. **D72** (2005), 115013, `hep-ph/0408011`.

[120] G. Branco, P. Ferreira, L. Lavoura, M. Rebelo, M. Sher, et al., Phys.Rept. **516** (2012), 1, `1106.0034`.

[121] T. Hambye and M. H. Tytgat, Phys.Lett. **B659** (2008), 651, `0707.0633`.

[122] T. Hambye, F.-S. Ling, L. Lopez Honorez, and J. Rocher, JHEP **0907** (2009), 090, `0903.4010`.

[123] Planck Collaboration, P. Ade et al., `1303.5076`.

[124] XENON100 Collaboration, E. Aprile et al., Phys.Rev.Lett. **109** (2012), 181301, `1207.5988`.

[125] N. D. Christensen and C. Duhr, Comput.Phys.Commun. **180** (2009), 1614, `0806.4194`.

[126] A. Alloul, N. D. Christensen, C. Degrande, C. Duhr, and B. Fuks, Comput.Phys.Commun. **185** (2014), 2250, `1310.1921`.

[127] T. Hahn, Comput.Phys.Commun. **140** (2001), 418, `hep-ph/0012260`.

[128] K. Griest and M. Kamionkowski, Phys.Rev.Lett. **64** (1990), 615.

[129] J. M. Cornwall, D. N. Levin, and G. Tiktopoulos, Phys.Rev. **D10** (1974), 1145.

[130] B. W. Lee, C. Quigg, and H. Thacker, Phys.Rev. **D16** (1977), 1519.

[131] A. Pukhov, E. Boos, M. Dubinin, V. Edneral, V. Ilyin, et al., `hep-ph/9908288`.

[132] A. Pukhov, `hep-ph/0412191`.

[133] M. Cirelli and G. Giesen, JCAP **1304** (2013), 015, `1301.7079`.

[134] PAMELA Collaboration, O. Adriani et al., Phys.Rev.Lett. **105** (2010), 121101, `1007.0821`.

[135] H.E.S.S.Collaboration, A. Abramowski et al., Phys.Rev.Lett. **106** (2011), 161301, `1103.3266`.

[136] T. Sjostrand, S. Mrenna, and P. Z. Skands, JHEP **0605** (2006), 026, `hep-ph/0603175`.

[137] H.E.S.S. Collaboration, A. Abramowski et al., Phys.Rev.Lett. **110** (2013), 041301, `1301.1173`.

[138] http://dpnc.unige.ch/dampe/index.html.

[139] A. Galper, O. Adriani, R. Aptekar, I. Arkhangelskaja, A. Arkhangelskiy, et al., Adv.Space Res. **51** (2013), 297, `1201.2490`.

[140] CTA Consortium, M. Actis et al., Exper.Astron. **32** (2011), 193, `1008.3703`.

[141] G. Belanger, B. Dumont, U. Ellwanger, J. Gunion, and S. Kraml, Phys.Lett. **B723** (2013), 340, `1302.5694`.

[142] P. P. Giardino, K. Kannike, I. Masina, M. Raidal, and A. Strumia, JHEP **1405** (2014), 046, `1303.3570`.

[143] G. Jungman, M. Kamionkowski, and K. Griest, Phys.Rept. **267** (1996), 195, `hep-ph/9506380`.

[144] H. M. Lee, M. Park, and W.-I. Park, Phys.Rev. **D86** (2012), 103502, `1205.4675`.

[145] A. Ibarra, H. M. Lee, S. L'opez Gehler, W.-I. Park, and M. Pato, JCAP **1305** (2013), 016, `1303.6632`.

[146] J. Hewett, H. Weerts, R. Brock, J. Butler, B. Casey, et al., `1205.2671`.

[147] G. Steigman, Phys.Rev. **D87** (2013), no. 10, 103517, `1303.0049`.

[148] G. Mangano, G. Miele, S. Pastor, T. Pinto, O. Pisanti, et al., Nucl.Phys. **B729** (2005), 221, `hep-ph/0506164`.

[149] LUX Collaboration, D. Akerib et al., Nucl.Instrum.Meth. **A704** (2013), 111, `1211.3788`.

[150] XENON1T collaboration, E. Aprile, `1206.6288`.

[151] S. Weinberg, *The quantum theory of fields: Foundations*, The Quantum Theory of Fields, no. v. 1, Cambridge University Press, 1995.